Bending-Related Faulting and Mantle Serpentinization at the Nicaraguan Subduction Zone

DISSERTATION ZUR ERLANGUNG DES DOKTORGRADES
DER MATHEMATISCH-NATURWISSENSCHAFTLICHEN FAKULTÄT
DER CHRISTIAN-ALBRECHTS-UNIVERSITÄT ZU KIEL

vorgelegt von

Marten Lefeldt

Kiel, 2008

Referent/in: PD Dr. Ingo Grevemeyer
Korreferent/in: Prof. Dr. Wolfgang Rabbel
Tag der mündlichen Prüfung: 28.04.2008
Zum Druck genehmigt: 28.04.2008

Der Dekan

Hiermit erkläre ich, dass die vorliegende Abhandlung, abgesehen der Beratung durch meine akademischen Lehrer, nach Inhalt und Form meine eigene Arbeit darstellt. Ferner habe ich weder diese noch eine ähnliche Arbeit an einer anderen Abteilung oder Hochschule im Rahmen eines Prüfungsverfahrens vorgelegt.

Marten Lefeldt

Abstract

At a convergent margin large amounts of structurally bound water are carried into the Earth's interior and - as the subducting plate descends and the temperature rises - are driven off to some extent into the mantle wedge, where they are thought to trigger intermediate-depth earthquakes in the Wadati-Benioff zone and melting under volcanic arcs. However, a largely uncertain fraction outlasts sub-arc fluid release and hence enters the deeper mantle, which leads to a connection between the oceans and the Earth's deep water cycle. Thus, a detailed knowledge of the water budget of a subduction zone is not only important to understand arc volcanism, but as well to comprehend the chemical development of the Earth's mantle. For this purpose, profound information about the amount of water that is subducted along with the oceanic plate is indispensable.

The present thesis uses geophysical methods to determine the degree of hydration of the Cocos Plate offshore Nicaragua, which is subducted beneath the Caribbean Plate.

In general it was assumed that structured water is transported into the slab in sediments and the upper crust only, though in recent years growing evidence suggested that lower crust and upper mantle might contain capacious amounts of fluids as well, since the bending of the incoming oceanic plate leads to a reactivation or creation of normal faults (bend-faults), which are visible in batrymetric data and have been inferred to cut deep enough into the plate to provide a pathway for seawater to penetrate into the lithosphere, changing "dry" peridotites to "wet" serpentinites, which contain up to 13% of water. Such a mechanism could transport much more fluids into the earth's interior than any other considered possibility. However, the cutting depth of these bend-faults and hence the depth that seawater could penetrate into the mantle was not well-defined, for one reason since focal depth of earthquakes associated with the bend-faults were poorly known. Yet previous studies assumed cutting depths such that serpentinization is firstly restricted by its thermal limit of 600° C.

This study uses openly accessible, global broadband data of earthquakes offshore Central America as well as an unique dataset from a local long-period earthquake monitoring network offshore Nicaragua, to determine typical focal depths off earthquakes at the trench-outer rise and further relates these focal depths to the cutting depths of bend-faults. In addition, a full 3d-tomographic inversion that consistently integrates seismic airgun blasts and local as well as regional seismicity, could show reduced seismic mantle velocities at the outer rise and nearby the deep sea trench with an evolutionary trend towards it. Best explained is this by a fractured and partly serpentinized lithosphere. The use of regional sources (i.e. earthquakes in distances of ≥200 km from the seismic network) in the tomographic inversion process made it possible, for the first time, to reflect the entire brittle lithosphere. In a second approach, relative arrival times of large earthquakes that occurred during the deployment of the seismic network were investigated. Again, it could be shown that seismic mantle velocities decrease in accordance with the onset of bend-faults in the bathymetry.

But not only seismic velocities decrease nearby the trench, the average moment magnitude of outer rise earthquakes does as well, though the number of events increases significantly. We explain this a weakened lithosphere and hence a reduced yield strain, which again suggests an occurrence of serpentinite.

However, tomographic images suggest that the area of reduced seismic velocities and in turn possible serpentinization does not reach the cutting depth of bend-faults nor the depth of the 600° C isotherm. Focal mechanisms of several earthquakes were determined via moment tensor inversion and forward modelling respectively and it could be shown that where seismic velocities are reduced only tensional ruptures occur, which allow for water infiltration, meanwhile the area beneath is dominated by compressional rupture behaviour, which presents a barrier for seawater. This result does not only confirm and enlarge flexure models of subducting plates [*Chapple and Forsyth*, 1979; *Christensen and Ruff*, 1988], but also establishes a coherent connection between stress distribution in the incoming plate and penetration depth of seawater and is the first study in this vein.

Zusammenfassung

An konvergenten Plattengrenzen werden große Mengen chemisch gebundenen Wassers in den oberen Erdmantel injiziert und - wenn die subduzierte Platte abtaucht und sich die Temperatur erhöht - durch metamorphe Umwandlungen teilweise wieder in den Mantelkeil freigegeben, wodurch Erdbeben in der Wadati-Benioff Zone ausgelöst werden können und der Schmelzpunkt des Mantelkeiles erniedrigt wird, was zu einer Aufschmelzung und somit zum Vulkanismus führt. Allerdings wird ein immer noch ungenau bekannter Anteil des gebundenen Wassers nicht freigesetzt, sondern in größere Tiefen transportiert, womit eine Verbindung zwischen den Ozeanen und dem Wasserzyklus des Erdmantels hergestellt ist. Somit könnte eine eingehende Kenntnis des Wasserhaushaltes einer Subduktionszone nicht nur Aufschluss über Vulkanismus, sondern auch über die Entwicklung des Erdmantels geben. Hierfür ist aber ein Wissen um die genaue Menge an Wasser, die mit der ozeanischen Platte subduziert wird, unabdingbar.

Die vorliegende Doktorarbeit benutzt geophysikalische Methoden, um den Hydrierungsgrad der Cocosplatte vor Nicaragua zu bestimmen, die dort unter die Karibische Platte taucht.

Im Allgemeinen ging man davon aus, dass chemisch gebundenes Wasser überwiegend in den Sedimenten und dem oberen Teil der Kruste vorkommt, allerdings wurde in den vergangenen Jahren eine weitere Möglichkeit hinzugezogen: Taucht die ozeanische Platte unter die kontinentale ab, so findet eine starke Biegung der Lithosphäre statt, was bereits seewärts des Tiefseegrabens zu Brüchen der Kruste und des oberen Mantels führt. Diese Brüche, die deutlich in bathymetrischen Daten erkennbar sind, könnten Meerwasser in die Lithosphäre eindringen lassen und dabei das "trockene" Peridotite in Serpentinite umwandeln, welches bis zu 13% Wasser enthalten kann. Ein solcher Mechanismus vermag bedeutend größere Mengen Fluide ins Erdinnere zu transportieren, als alle zuvor betrachteten Möglichkeiten. Allerdings war bisher nicht genau bekannt, wie tief diese Brüche in den Mantel einschneiden und in welche Tiefen somit Meerwasser gelangen kann, was unter anderem daran lag, dass die Herdtiefen der mit den Brüchen einhergehenden Erdbeben nur äußerst ungenügend bekannt waren. Vorausgegangene Studien nahmen aber Einschnitttiefen derart an, dass Serpentinisierung erst durchs thermische Limit von 600° C begrenzt wird.

Diese Studie benutzt zum einen frei zugängliche, globale Daten von Erdbeben vor Mittelamerika und zum anderen Daten eines seismischen Langzeitnetzwerkes vor Nicaragua, um erstmals typische Herdtiefen für Beben seewärts des Mittelamerikanischen Tiefseegrabens zu bestimmen und stellt darüber hinaus einen Zusammenhang zwischen diesen Tiefen und der Schnitttiefe der Brüche her. Außerdem kann durch eine vollständige 3D-Tomographie, die konsistent Luftpulserschüsse und lokale sowie regionale Seismizität invertiert, gezeigt werden, dass seismische Mantelgeschwindigkeiten der Cocosplatte in unmittelbarer Nähe des Tiefseegrabens reduziert werden. Diese Reduktion deutet auf eine poröse, teilweise serpentinisierte Lithosphäre hin. Dabei machte es die Einbeziehung von 'regionalen' Erdbeben (d.h. Erdbeben in Abständen von $\geq$200 km zum Netzwerk) in die tomographische Inversion erstmals möglich, den gesamten brüchigen Bereich der Lithosphäre wiederzugeben. In einem zweiten Ansatz konnte durch relative Laufzeiten für Strahlen weltweiter Großbeben, die während des Einsatzes des Langzeitnetzwerkes auftraten, ebenfalls gezeigt werden, dass seismische Geschwindigkeiten dort reduziert werden, wo die einfahrende Platte anfängt zu brechen.

Aber nicht alleine die seismischen Geschwindigkeiten werden Nahe des Tiefseegrabens reduziert, sondern auch die durchschnittlichen Momentmagnituden der Erdbeben, während deren Zahl rapide zunimmt. Dies kann durch eine Abschwächung der Belastbarkeit der Lithosphäre erklärt werden, was abermals auf ein Vorhandensein von Serpentinite deutet.

Allerdings zeigt diese Studie, dass sowohl die 600° C Isotherme als auch die Einschnitttiefe der Brüche bedeutend tiefer liegen, als die Reduktion seismischer Geschwindigkeiten und damit möglicher Serpentinisierung. Durch Momententensor Inversion, bzw. Vorwärtsmodellierung gelang die Bestimmung von Herdmechanismen mehrerer Erdbeben und es konnte gezeigt werden, dass im Bereich der reduzierten Geschwindigkeiten nur expansive Brüche stattfinden, die das Eindringen von Wasser erlauben, während unterhalb nur kompressive Brüche auftreten, die das Gegenteil bewirken. Dieses Ergebnis unterstreicht nicht nur bekannte Biegungsmodelle für subduzierte Platten [*Chapple and Forsyth*, 1979; *Christensen and Ruff*, 1988], bzw. erweitert diese, sondern stellt auch einen schlüssigen Zusammenhang zwischen Spannungszuständen in der Lithosphäre und dem Eindringen von Meerwasser her. Diese Studie ist die erste dieser Art.

Contents

List of Figures

List of Tables

Vorwort

Aus meiner Zeit als Doktorand sind bisher drei Veröffentlichen hervorgegangen:

> Lefeldt, M. & I. Grevemeyer (2008), Centroid depth and mechanism of trench-outer rise earthquakes off Central America, *Geophys. J. Int.*, *172*, 240-251, doi:10.1111/j.1365-246X.2007.03616.x
>
> Lefeldt, M., I. Grevemeyer, C. Ranero, J. Goßler & J. Bialas (2007), Mantle hydration and subduction of water at the Nicaraguan trench, *Letter to Nature*, *submitted*
>
> Lefeldt, M., I. Grevemeyer & C. Ranero (2008), Screening the Oceanic Plate: Implications from teleseismic arrival time residuals for serpentinization at deep sea trenches, *in preparation*

Die drei Arbeiten beschäftigen sich zwar mit derselben Problematik, gehen diese aber auf sehr verschiedene Art an.

Auch wenn zwei Veröffentlichungen zum gegenwärtigen Zeitpunkt noch nicht akzeptiert sind und dies für eine kumulative Promotion nicht ausreichend ist, so möchte ich doch das Grundkonstrukt einer wissenschaftlichen Publikation nicht verlassen und die Veröffentlichungen in drei, in sich geschlossenen Kapiteln darstellen. Dies auch, um die unterschiedliche Herangehensweise, die den Arbeiten zugrunde liegt, weiter herauszustellen. Dabei lassen sich gewisse Wiederholungen (Einleitung, geol. Überblick, etc.) nicht vermeiden.

Nach einer Einführung in die Thematik in Kapitel 1, wird sich das zweite Kapitel mit der Geologie und der Tektonik des Arbeitsgebietes auseinandersetzen. Kapitel 3 bis 5 beschäftigen sich jeweils mit einer der Veröffentlichungen, Katipel 6 faßt die Ergebnisse zusammen und Kapitel 7 gibt einen Ausblick auf das, was basierend auf diese Arbeit in Zukunft getan wird oder getan werden könnte.

Chapter 1

Introduction

Earthquakes and volcanism are triggers to the most devastating natural disasters in the history of humanity. While ancient cultures believed them to be the anger of gods, the picture changed quite early towards a scientific explanation when the great Grecian Philosophers hypothesized that earthquakes are caused when continents, which are floating on the water are bobing up and down - which is amazingly close to Tectonic Theory. Unfortunately, these approaches perished when the occurrence of Christianity covered science in Europe with a second darkness and reintegrated natural disasters into their naive-religious views.

Not until a strong earthquake destroyed Lisbon on 01 November 1755 with conflagration and a subsequent Tsunami, the prime minister Sebastião de Mello instructed to assemble all information about duration of the quake, number of aftershocks and damages, which makes it today possible to reconstruct the event at that time and thus this earthquake, whose moment magnitude of Mw=8.5 to 9.0 is at the upper limit, can be considered the hour of birth of modern seismology.

To date this area of science lost none of its importance, since great loss of human lives - like the disaster in the Indian Ocean after the seaquake on 26 December 2004 - are mostly caused by the unpredictability and short warning time of earthquakes and Tsunamis, as well as volcano eruptions and can only be avoided in the future if all involved processes are to be understood more thoroughly.

The present thesis, which is contribution of the Collaborative Research Center 574 "Volatiles and Fluids in Subduction Zones: Climate Feedback and Trigger Mechanisms for Natural Disaster" attends to this subject-matter and focuses therefore on the Central American country Nicaragua. Central America belongs to the circumpacific Ring of Fire, a ring of seismic and volcanic active zones that embraces the Pacific. About 65% of all active volcanos and the majority of the worldwide seismicity are located in these zones, including the seaquake of the Indian Ocean and the largest ever recorded earthquake (Mw=9.5), that occurred offshore Chile in 1960 and caused a Tsunami, which yet devastated the coast of South Africa.

Nicaragua is part of the Caribbean Plate, which today consists of both, continental and oceanic lithosphere. Noticeable earthquakes are almost daily events and in 1992 a seaquake 120 km from Nicaragua led to a Tsunami, which claimed more than 110 lives. Furthermore, about 16 active volcanos are located here. At the

Nicaraguan subduction zone, the incoming oceanic Cocos Plate is subducted along the Middle America Trench beneath the overriding Caribbean Plate. It is assumed that an incoming subducted plate underwent several high- and low-temperature alteration processes in the past that led to a partial hydration. Fluids that are carried in this way into the subduction zone are released by metamorphic reactions into the mantle wedge to trigger arc melting [*Rüpke et al.*, 2002]. The produced melts start to rise towards the typically chain of arc volcanoes that is usually located ∼100km above the subducted plate (Fig. 1.1). However, some water may outlive the sub-arc release and is transported into the deeper mantle.

Understanding these processes more thoroughly is indispensable to expand our knowledge about melting and earthquake generation at subduction zones and the geochemical evolution of the Earth's mantle. Though, one of the yet largely unconstrained values is the amount of fluids that are carried along with the subducting plate.

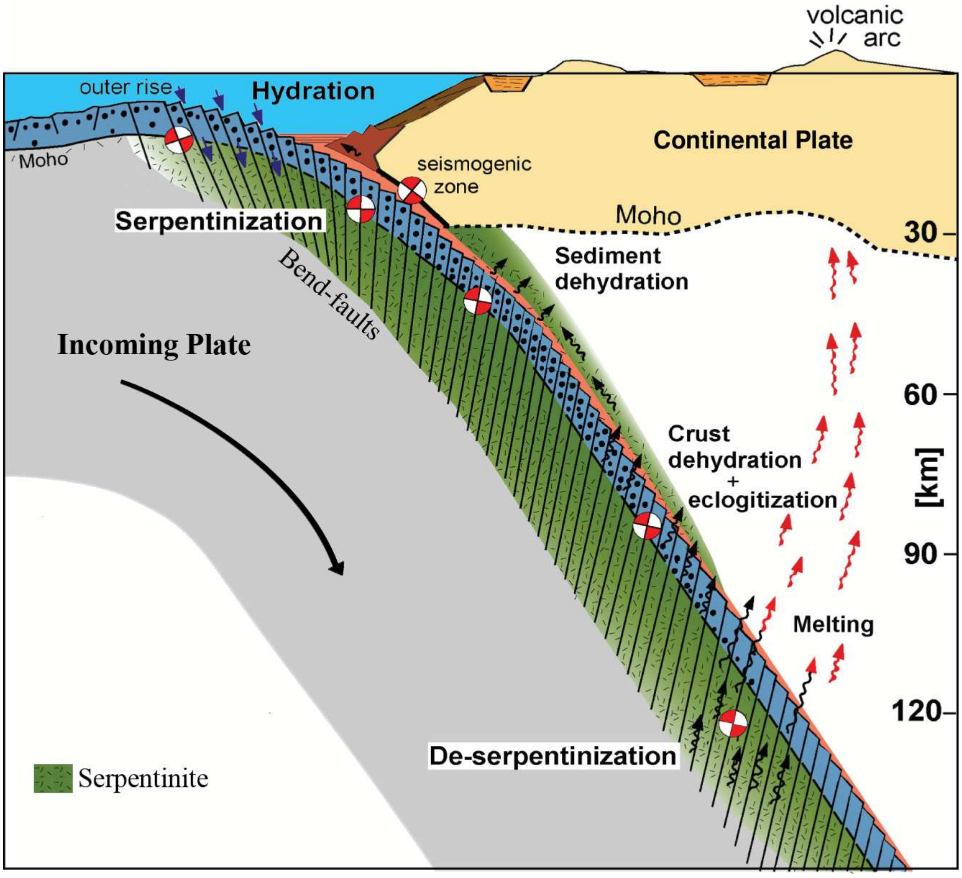

Figure 1.1: *Schematic drawing of an subduction zone including fracturing and serpentinization prior to subduction, as well as fluid release beneath the arc (modified after Ranero et al. [2005]).*

Generally, water can be transported into the subduction zone in chemically bound form in sediments and upper crust or as pore-water trapped in the sediments and in open void spaces in the igneous crust [*Staudigel*, 1996; *Jarrad*, 2003].

In recent years growing evidence suggested another possibility: when the incoming plate bends under the continental plate, the flexure - which can be described as the flexure of a thin elastic plate [*Chapple and Forsyth*, 1979] - causes fractures in the oceanic lithosphere prior to subduction [*Masson*, 1991; *Kobayashi* et al., 1998; *Ranero et al.*, 2003]. Off Nicaragua, existing data suggest that bending-related faults (following *Ranero et al.*, 2003 we will call them bend-faults) cut at least 10-15 km deep into the mantle [*Ranero et al.*, 2003; *Lefeldt and Grevemeyer*, 2008] and thus provide a pathway for seawater to penetrate into the mantle and react with the cold lithospheric material [*Christensen and Ruff*, 1988; *Hasegawa*, 1994; *Ranero et al.*, 2003], changing "dry" peridotites to "wet" serpentinites [*Peacock*, 2001; 2003], which contain up to 13% of water. Even a partly serpentinized crust and upper mantle would present an efficient system for seawater injection into the subduction zone with the potential to be the most important one [*Ranero et al.*, 2003].

Supporting evidence comes from seismic wide-angle and refraction data. In the study area, P-wave velocities in the crust and the upper mantle show unusually low values. This velocity anomaly develops $\sim$50 km seawards the Middle America Trench - were bend-faults become a highly visible feature in the bathymetry - and extends towards it. Seismic velocities are smaller in serpentinite than in peridotide [*Carlson and Miller*, 2003] and thus, a fractured and serpentinized lithosphere is the best explanation [*Grevemeyer et al.*, 2007; *Ivandic et al.*, 2007]. However, at the outset of this study existing seismic data could only resolve the upper 3-5 km of the mantle, while bend-faults and in consequence serpentinization might reach greater depths.

This study attends to the mechanics and behavior of earthquakes at the trench-outer rise offshore Nicaragua and the implications for mantle hydration by using different methods:

1. The first part of this thesis will present results and methods for an investigation of seven teleseismic earthquakes - two offshore Mexico and five offshore Nicaragua / Costa Rica - with moment magnitudes between Mw=5.5 and 6.7 (In this thesis, teleseismic events will be defined as earthquakes that can be recorded in at least 90° distance). For each, accurate epicenter locations were determined and a sophisticated moment tensor inversion procedure was applied to determine a detailed focal mechanisms. Therefore, existing methods were modified and adjusted.

2. A local earthquake monitoring network consisting of 21 *Ocean Bottom Seismometer* (OBS) and *Ocean Bottom Hydrophones* (OBH) on an area of approximately 120x100km^2 was installed at the trench-outer rise off Nicaragua and seismic activities were recorded for a duration of two months. This unique data set made it possible to generate an accurate velocity model for the oceanic mantle and to determine focal depths, fault mechanisms and moment magnitudes for several earthquakes.

3. The same network described in the former item also recorded several teleseismic earthquakes in great distances, among them a Mw=7.6 event that occurred in Pakistan ($\sim 160°$ distance). Rays emitted from such sources arrive at the receivers under very steep angles. Synthetic relative arrival times within the network have been calculated and compared to the observed ones. Arrivals times at receivers nearby the trench are delayed compared to the ones further seawards, which suggests a zone of reduced seismic velocities with an evolutionary trend towards the trench.

Previous studies related the maximum depth of mantle serpentinization to the depth that bend-faults cut into the lithosphere or to the $600°C$ thermal depth limit of serpentinization [e.g. *Ranero et al.*, 2003]. However, even though bend-faults were made visible in seismic refraction data [*Ranero et al.*, 2003], a depth migration of these data was not possible and neither was a clear ending of these faults observable. Further, prior to the present study, no precise data for typical hypocenter depths of trench-outer rise earthquakes existed. Thus, the maximum depth of bend-faults was poorly known.

The results presented in this thesis give accurate focal depths for both, microseismic and teleseismic trench-outer rise earthquakes offshore Central America. We linked these hypocenter parameters to the cutting depth of bend-faults and show that they extend deeper than the area of reduced seismic velocities and hence serpentinization. Via moment tensor inversion and forward modelling schemes we determined several fault mechanism solutions which we relate to the stress distribution in the incoming plate. We document that mantle serpentinization is controlled by the location of the neutral plane between tensional stress regime on top of the plate and compressional one beneath, but not by the cutting depth of bend-faults nor the $600°C$ thermal depth limit. Further, we present evidence that suggests that the incoming plate is significantly weakened and hence indeed serpentinized. In this context, we slightly modify plate stress models of *Chapple and Forsyth* [1979] and *Christensen and Ruff* [1988]. Finally, we present new numbers for the water input at the Nicaraguan Subduction Zone.

Chapter 2

Tectonical Framework

This chapter aspires to give a brief overview of the geological and tectonical settings of the Nicaraguan subduction zone. Since this study focuses on trench-outer rise processes, a broader description of the incoming oceanic plate, the Cocos Plate will be prefixed.

2.1 The Cocos Plate

Approximately 80 million years ago, the Farallon Plate started to subduct beneath the North American Plate. Once its centerpiece was fully subducted (~22,7 million years ago), the plate broke apart [*Barckhausen et al.*, 2001] and formed the *Juan de Fuca Plate* in the North, which continued to subduct under the northern part of the North American Plate, the *Cocos Plate* and the further southward located *Nazca Plate*, which subducts beneath the South American Plate.

Cocos and Nazca Plate are separated by the Panama Basin and the Cocos-Nazca Spreadingcenter (CNS), whereat the CNS can be divided into three subsequent spreading systems, CNS-1, 22.7-19.5 Ma; CNS-2, 19.5-14.7 Ma; and CNS-3, 14.7 Ma-present. CNS-1 was characterized by a high spreading rate. The jump from CNS-1 to CNS-2 occurred 19.5 million years ago: probably due to the Galapagos Hot Spot, the spreading axis changed southwards which caused a significant slowdown of the spreading rate [*Barckhausen et al.*, 2001]. A second jump of the spreading axis southwards happened about 14.7 million years ago. Today's spreadingrate is 2.6 cm/a in the west [*Lonsdale*, 1988] and increases in an eastward direction to 7.6 cm/a [*Allerton et al.*, 1996], which causes a rotation of the Cocos Plate. The slow or moderate spreading rates combined with transform faults caused by the Galapagos Hot Spot lead to a relatively rough crust in this area.

Westwards, the East Pacific Rise (EPR) defines the Cocos Plate. This part of the EPR has a comparable high spreading rate of 10-12 cm/a [*Carbotte & Macdonald*, 1992; *Madsen et al.*, 1992], but 11-18 million years ago a period of ultrafast spreading with rates of more than 20 cm/a [*Wilson*, 1996] led to a thin and smooth crust [*Wilson & Teagle*, 2003], as well as a consistent orientation of the anisotrop Olivine crystals in the upper mantle, which causes high seismic P-wave velocities of 8.4 km/s parallel to the spreading axis [*Nicolas & Christensen*, 1987]. However, the crust that is formed today at the EPR is as well comparable thin (4,7 km to 7,3 km [*Vera et al.*, 1990; *Barth & Mutter*, 1996; *Canales et al.*, 2003]) and smooth, which leads to a visible transition between crust formed at the CNS and formed at the EPR, the so-called "Rough-Smooth" Boundary [*Hey*, 1977].

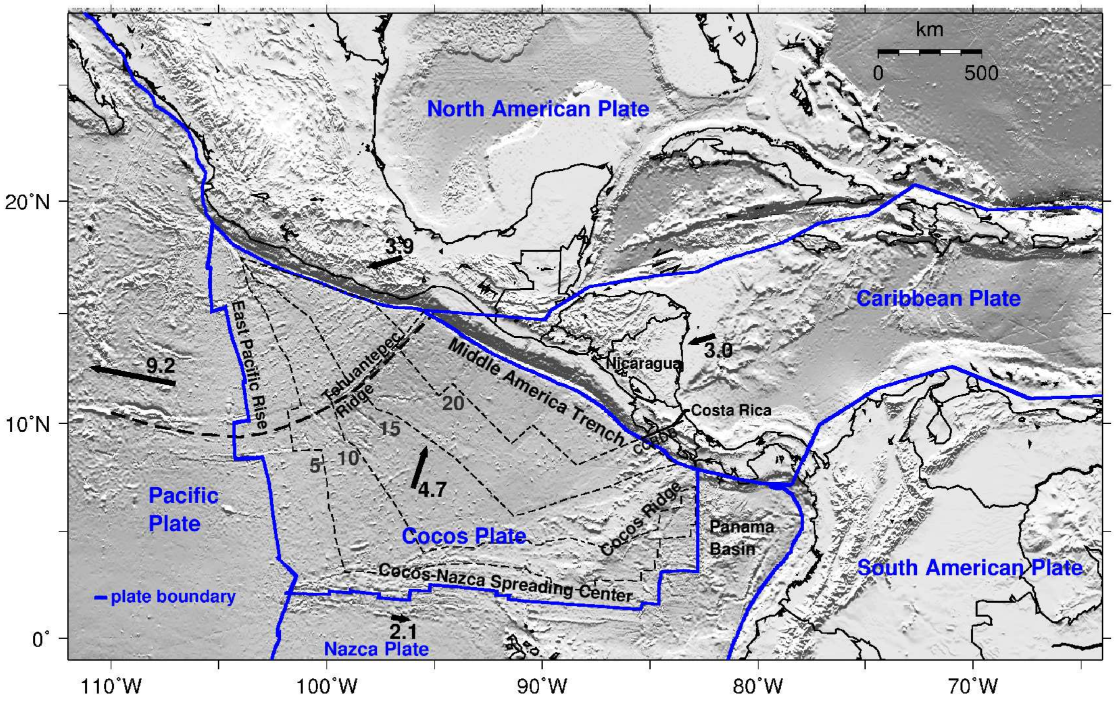

Figure 2.1: *Contour map of Central America [Smith & Sandwell, 1997] and the capital plate boundaries [Bird, 2003]. The Middle America Trench (MAT) evolves from the subduction of the Cocos Plate beneath the Caribbean Plate. Arrows mark the direction and velocity of the absolute plate movements [Gripp & Gordon, 2002, digitized by Berhorst, 2006]. The dashed lines show isochrones [Wilson & Teagle, 2003; digitized by Berhorst, 2006]. CCRDB denotes the Central Costa Rica Deformation Belt.*

This boundary vanishes for crust older than 19.5 million years, which was formed prior to the first jump of the spreading axis of the CNS, when EPR and CNS had comparable spreading rates [*Barckhausen et al.*, 2001].

Finally, the northern part of the Cocos Plate is subducted beneath the North American Plate and the northeastern part beneath the Caribbean Plate and thereby forms the *Middle America Trench* (MAT).

2.2 The Nicaraguan Subduction Zone

Due to the rotation of the Cocos Plate, the subduction rate along the MAT varies from ~9 cm/a in the south to ~7 cm/a in the North, with a slightly oblique subduction (10°) northwards of the Central Costa Rica Deformed Belt [*DeMets*, 2001]. Offshore Nicaragua, the age of the subducted crust is nearly consistently 24 Ma [*Wilson % Teagle*, 2003], which changes southwards, where the subducted crust was formed at the CNS and is with 15-22 Ma much younger.

The subduction angle, which can be approximated by the location of the Wadati-Benioff, shows an increase from 60° at Guatemala to 80° at Nicaragua and Earthquakes with focal depths up to 200 km are recorded [*Burbach et al.*, 1984]. Southwards of the Central Costa Rica Deformed Belt, both, the subduction angle and the maximum focal depth of earthquakes decrease significantly [*Protti et al.*,1994].

High resolution multichannel bathymetric mapping of the incoming plate (Fig. 2.2) shows that bend-faults are visible across most of the ocean trench slope. Single faults can be tracked for at least 50 km in the bathymetry [*Ranero et al.*, 2003]. The hypothesis that these faults allow seawater to penetrate into the mantle is perhaps supported by geochemical data from the volcanic arc, which suggests that mafic magmas in Nicaragua have water concentrations among the highest in the world [*Roggensack et al.*, 1997]. Additionally, P-wave arrivals from intraslab events at 100-150 km depth show high-frequency late arrivals, which suggest a 2.5-6 km thick low-velocity waveguide at the top of the down-going plate [*Abers et al.*, 2003]. Such a feature is best explained by >5wt% water in the subducted crust, which is 2-3 times higher hydration than inferred for other subduction zones.

Seismicity at the trench-outer rise is not only caused by the bending of the incoming plate and the associated reactivation of existing or creation of new faults. Large outer rise events are rather related to the pulling of the down-going slab [*Lefeldt and Grevemeyer*, 2008]. Following *Chapple and Forsyth* [1979], the bending of the incoming plate leads to a tensional regime on top of the plate grading into a compressional one beneath. Bending-related earthquakes can occur in both regimes and therefore can have tensional normal fault or compressional thrust fault mechanisms. In contrast, a pulling slab leads to events of mostly tensional character. Fig. 2.2 shows the distribution of recent teleseismic events. Note, how rare trench-outer rise normal fault events are compared to interplate or deep intraslab events.

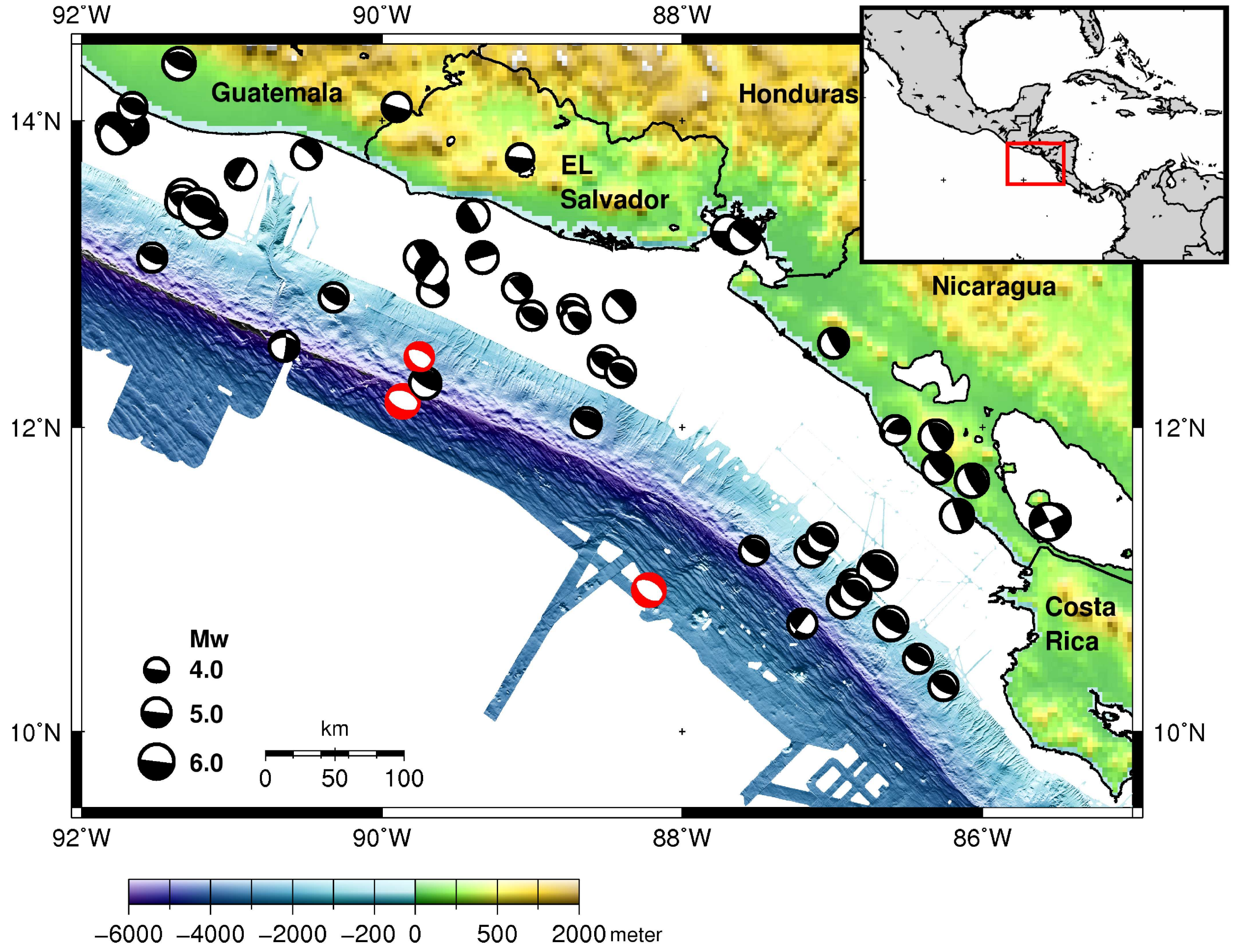

Figure 2.2: *Multichannel bathymetry of the MAT offshore Nicaragua [Ranero et al., 2003] and most recent teleseismicity (Mw≥4.0) after Harvard CMT catalog. Shown are all events between 01/2005. Red focal mechanisms show normal fault events, black ones all remaining.*

Chapter 3

Teleseismic Events

Trench-outer rise earthquakes occur by reactivation or creation of normal faults caused as the oceanic lithosphere approaches a subduction zone and bends into the deep-sea trench. These faults may cut deep enough into the mantle to allow seawater to penetrate into the lithosphere, causing serpentinization. The amount of water carried into the mantle is thought to be linked to the maximum depth that the tensional faults cut into the lithosphere, which in turn is directly linked to the maximum focal depths of outer rise normal faulting earthquakes.

We analyzed teleseismic P and S waves of seven earthquakes from the trench-outer rise offshore of Central America using teleseismic waveform inversion of broadband data. For the computation of Green's functions for waveform inversion, probabilistic earthquake locations were calculated. To study the rupture process, earthquake centroid depths and focal mechanisms for a sequence of subevents were calculated. Both, hypocentral depths from the relocation process and the estimated centroid depths from the waveform inversion show that all events occur at shallow depths (<30 km). Furthermore, the locations of the subevents relative to each other suggest that fault planes for Mw$\sim$6 are in the order of 50 km in length and only 5-10km in width. Rupture generally propagates down-dip and the focal mechanisms change for most events from normal faulting to strike-slip or oblique thrusting with time. The depth at which this mechanism change is observed may represent the depth of the nodal plane between tensional and compressional regions in the incoming plate.

3.1 Introduction

Earthquakes in the trench-outer rise of subduction zones are inherently related to plate subduction. *Chapple and Forsyth* [1979] proposed a model in which outer rise earthquakes are a consequence of plate flexure, as the lithosphere is bent into the trench. Their model suggests that the uppermost lithosphere behaves as a thin elastic plate and that downward flexure at the subduction zone leads to a tensional regime at the top of the plate, grading into a compressional regime at the bottom. Global compilations of earthquake mechanisms based on waveform inversion support this model, as normal faulting events characterise the uppermost 25 km of the incoming lithosphere while thrust faulting, and hence compressional fault behaviour, occurs at greater depth [e.g., *Seno and Gonzalez*, 1987; *Seno and Yamanaka*, 1996]. However, the energy released by great outer rise events, like the 1933 Sanriku Ms=8.3 earthquake, suggest that fracturing took place over almost the entire thickness of the lithosphere, thereby precluding the possibility that such events merely represent a surface tensile crack due to the flexure of the downgoing plate [*Kanamori*, 1971]. Such large scale lithospheric faulting is presumably due to a gravitational pull exerted by the cold sinking lithosphere [*Kanamori*, 1971; *Spence*, 1986].

Multibeam bathymetric coverage of the outer rise region support the view that the oceanic plate may become pervasively fractured prior to subduction [*Masson*, 1991; *Kobayashi et al.*, 1998; *Ranero et al.*, 2003]. At the seafloor, faults have throws of up to 100-500 m and are often 10-50 km long [*Kobayashi et al.*, 1998; *Ranero et al.*, 2003]. Offshore Nicaragua, faulting and fault growth between the outer rise and the trench axis generate a prominent stairway-like seafloor relief prior to subduction. The depth down to which the faults cut into the crust or mantle is poorly known, due to the fact that the centroid depth of earthquakes is difficult to determine for shallow events in the ocean [e.g., *Yoshida et al.*, 1992], though depth phases and waveform modeling suggest that faults may cut often 30-40 km into the mantle [*Spence*, 1986; *Tichelaar et al.*, 1992].

Growing evidence suggests that trench-outer rise earthquakes may open pathways for fluids into the crust and mantle that cause extensive hydration of the incoming plate prior to subduction and hence may affect the Earth‘s water cycle. Some of these faults may cut deep enough into the lithosphere [*Christensen and Ruff*, 1988; *Hasegawa et al.*, 1994] to reach and react with the lithospheric mantle [*Ranero et al.*, 2003], changing “dry“ peridotites to “wet“ serpentinites, which contain up to 13 wt% of bound water. In consequence, outer rise processes may affect a number of subduction zone features, such as the location of the seismogenic coupling zone [*Hyndman and Wang*, 1993], the melt generation under volcanic arcs [*Rüpke et al.*, 2002] and Wadati-Benioff earthquakes [*Meade and Jeanloz*, 1991; *Kirby et al.*, 1996, *Ranero et al.*, 2005].

While trench-outer rise earthquakes in many areas have been studied elsewhere [*Chappel and Forsyth*, 1979; *Forsyth*, 1982; *Seno and Gonzalez*, 1987; *Seno and Yamanaka*, 1996], little is known from earthquakes along the Middle America Trench. In contrast, most recent studies on plate hydration associated with trench-outer rise processes concentrate their efforts on the subduction zone of Costa Rica and Nicaragua [e.g., *Ranero et al.* 2003; *Grevemeyer et al.* 2005; 2007].

In this study we present an investigation of seven outer rise events with Mw>5.5 that occurred between 1992 and 2004 at the Middle America trench. All events have been relocated using travel time pick data. Centroid depth, focal mechanism, and rupture behaviour were determined from the inversion of body waves using broadband data. We use these results to show that tensional outer rise events offshore Central America are very shallow and show narrow fault planes. We link these results to seismic images published by *Ranero et al.* [2003] in the context of mantle hydration.

3.2 Tectonical Framework and Setting

The Middle America Trench (MAT) extends from the Gulf of Tehuantepec to Panama. Earthquakes along the MAT clearly define a Wadati-Benioff zone of landward dipping seismicity where the Cocos plate subducts beneath Central America. The age of the incoming plate (Wilson 1996; Barckhausen *et al.* 2001) increases southwards from 11 Myr to 25 Myr (Fig. 3.1). The margin normal convergence rate increases from ∼40 mm/yr to ∼88 mm/yr from Mexico to southern Costa Rica (DeMets *et al.* 1999). The most prominent features entering the trench are the Tehuantepec fracture zone subducting under southern Mexico and the Cocos Ridge subducting under southern Costa Rica. The crust forming the Cocos plate was created at the fast spreading East Pacific Rise and the Galapagos-Nazca spreading center. The suture between both domains is located offshore Nicoya Peninsula (Barckhausen *et al.* 2001). The study area, however, is located north of Nicoya Peninsula. Thus, all earthquakes studied here occurred in lithosphere created at the East Pacific Rise. Offshore Northern Costa Rica and Nicaragua magnetic anomalies run parallel to the trench axis. North of Nicaragua, the trench axis bends and from El Salvador to Mexico magnetic anomalies are subducted at low angles.

High resolution multibeam bathymetry offshore Nicaragua, El Salvador and Guatemala [*Ranero et al.*, 2005] shows that bending-related faulting is pervasive across most of the ocean trench slope (Fig. 3.2). Multi-channel seismic (MCS) reflection data suggested that some of these faults may cut 10-15 km deep into the lithosphere, which may promote fluid flow down to mantle depth [*Ranero et al.*, 2003] and may cause serpentinization of the mantle between the outer rise and the trench axis. Heat flow data obtained on the incoming plate off Nicaragua suggest that bending-related faulting reactivates a vigorous hydrothermal circulation system prior to subduction [*Grevemeyer et al.*, 2005] and low seismic velocities occurring where MCS data image deep normal faulting suggest that seawater actually reaches down to mantle depth to cause serpentinization [*Grevemeyer et al.*, 2007]. Furthermore, seismological data indicates that regional P-waves from intraslab events at 100-150 km depth show high-frequency late arrivals, most likely trapped in a 2.5-6 km thick low-velocity waveguide at the top of the incoming plate. Such low velocities can best be explained by >5 wt.% of water in the subducted crust, which is 2-3

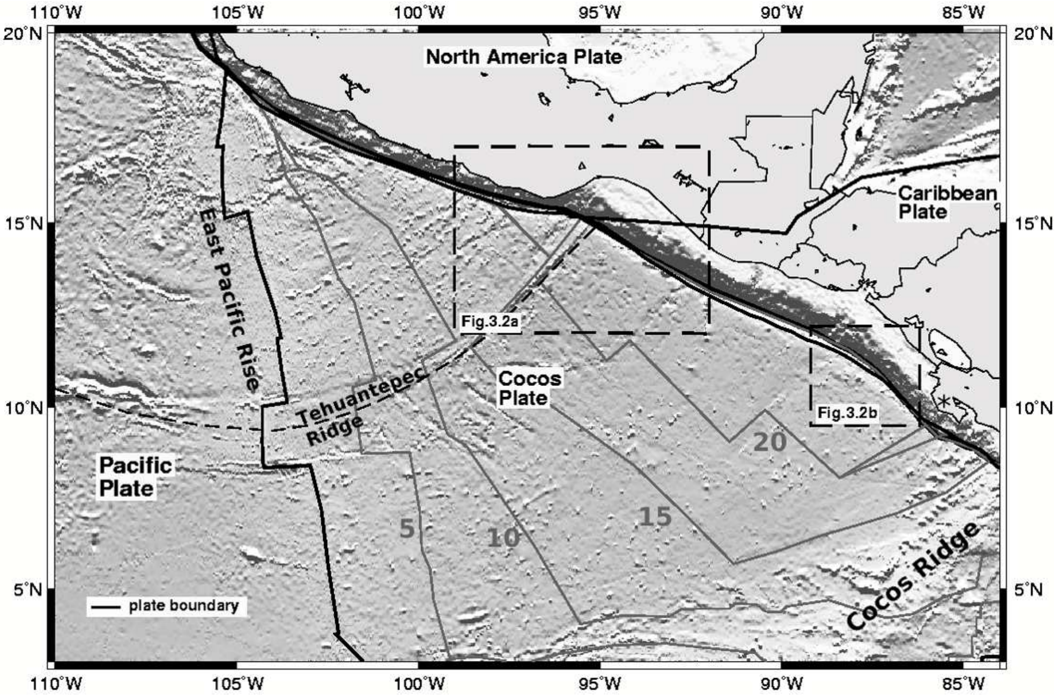

Figure 3.1: *Contour map of the Cocos Plate. (Smith and Sandwell 1997) with plate boundaries (modified after Bird 2003). The grey lines denote isochrons with 5 Ma distance (Wilson and Teagle 2002). The dashed frames give the positions of the sections in Fig. 3.2, the asterisk next to the down right corner of the Fig. 3.2b-frame shows Nicoya Peninsula*

times the hydration inferred for other slabs (Abers *et al.* 2003).

3.3 Data

We studied seven trench-outer rise earthquakes that occurred off Central America between 1992 and 2004. Magnitudes range from Mw=5.5 to 6.4 (Table 3.1). Broadband data for teleseismic waveform inversion were downloaded at the *Incorporated Research Institution for Seismology* (IRIS) from IRIS-DMC's archive. Seismograms were chosen from the aspect of good azimuth coverage and good data quality. Here the latter simply means that the data is considered as of good quality if the P and SH wave is clearly distinguishable from the noise. The records were converted into ground displacement and a three pole low-pass filter (1 Hz) has been applied.

In addition to the waveform data we retrieved phase data from the *National Earthquake Information Center* (NEIC) of the *US Geological Survey* (USGS) to relocate the earthquake epicenters. The USGS uses and archives travel time from a dense worldwide network of stations. However, the distribution of continents and ocean islands leaves a gap over the Pacific Ocean (Fig. 3.3).

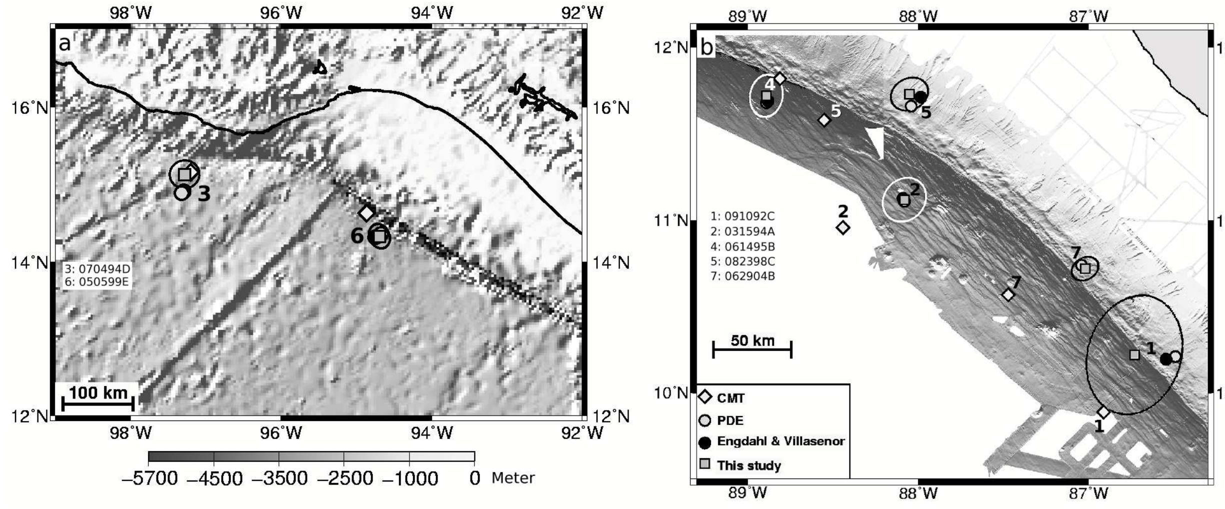

Figure 3.2: *Comparision between epicenters from Table 1 and different catalogues. Numbering and labelling is the same as in Table 1. Ellipses are 90%-confidence-ellipses. (a) Seafloor topography after Smith and Sandwell (1997) (b) Multibeam bathymetry offshore Nicaragua.*

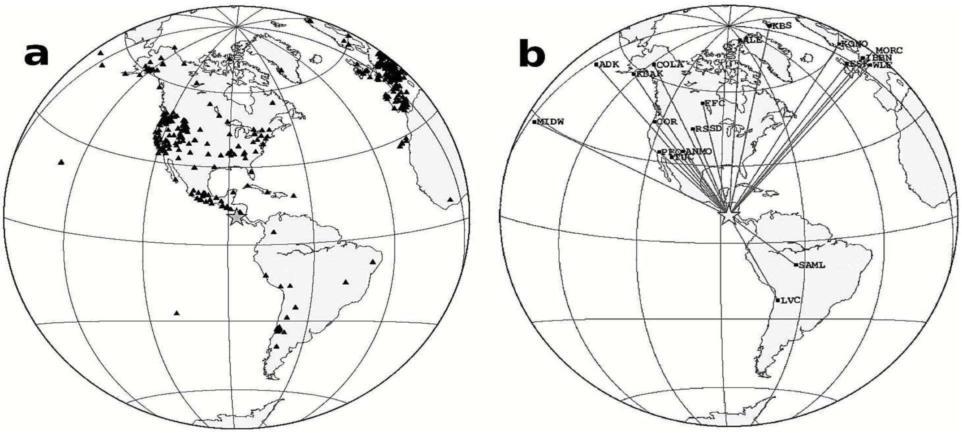

Figure 3.3: *Distribution of (a) stations for the relocation process of the 062904B-event (picks from around 450 stations have been used. Data was retrieved from USGS) and (b) of IRIS broadband seismograph stations used for the waveform inversion of the same event. The star always denotes the epicenter.*

Table 3.1: Events in this study.

No.	Event	Mw	Lat	Lon	Depth [km]
1	091092C	5.9	10.22	-86.73	9
2	031594A	5.8	11.12	-88.08	15
3	070494D	6.4	15.13	-97.28	17
4	061495B	5.5	11.72	-88.89	15
5	082398C	6.7	11.73	-88.05	21
6	050599E	6.1	14.33	-94.69	24
7	062904B	6.3	10.72	-87.02	11

The labelling (column 2) is the same as used in *Harvard CMT Catalog* and simply consists of the date on which the event took place and a letter for what number the event was on that date.

3.4 Relocation

Automated teleseismic event locations often come with large uncertainties, due to timing errors, phase misslocation [*Lomax et al.*, 2000] or limitations of the algorithms, in particular for shallow earthquakes [*McGinnis*, 2001]. Earthquake catalogues such as Engdahl and Villasenor (2002) or NEIC/PDE [1] give different locations. However, for the following moment tensor inversion, the computation of Green‘s function is indispensable and sensitive to the epicenter-station distances. Therefore, events were re-located using the *NonLinLoc*-Package (see 3.4.1) from *Lomax et al.* (2000; 2001) to yield probabilistic event locations.

The phase data together with a 1D, spherically-layered travel-time grid, which was created for each phase type at each station using the TauP Toolkit [2] with the ak135 1D Travel Time Tables [*Kennett*, 1995] gave the input for the NonLinLoc-code. The step size of the grid search was 0.05° in latitude and longitude and 2 km in depth. Hypocenter coordinates in Table 3.1 are results of this calculation. Fig. 3.2 compares epicenters from different catalogues. The match with acknowledged catalogues, like *Engdahl and Villaseñor* [2002] and NEIC/PDE, is excellent. Epicenters from these catalogues lie throughout into the 90%-confidence-ellipse (Fig. 3.2), which gives the area in which the epicenter is located with a likelihood of 90%.

3.4.1 The NonLinLoc-Package

This section gives a brief overview of the earthquake location algorithm used for this study. The description is in close imitation to *Lomax et al.* [2001] to which - for further insights - reference is made at this point.

NonLinLoc is a non-linear travel-time calculation code that produces an optimal hypocenter, a misfit function and an estimate of the probability density function

---

[1] (http://neic.usgs.gov/neis/epic/)

[2] (http://www.seis.sc.edu/software/TauP)

from arrival times of seismic phase data using a systematic 3D-grid-search.

The location algorithm used in NLLoc [*Lomax et al.*, 2000] follows the inversion approach of *Tarantola and Valette* [1982], and the earthquake location methods of *Tarantola and Valette* [1982]; *Moser, van Eck and Nolet* [1992] and *Wittlinger et al.* [1993]. The errors in both, the observed phase time pick data and the forward problem (travel-time calculation) are assumed to be Gaussian. This assumption allows the direct, analytic calculation of a maximum likelihood origin time, given the observed arrival times and the calculated travel times between the observing stations and a point in xyz space. Thus, the 4D problem of hypocenter location reduces to a 3D search over x, y, z space.

Inversion Approach

The program NLLoc [*Lomax et al.*, 2000] uses an earthquake location algorithm based on the probabilistic formulation of inversion by *Tarantola and Valette* [1982] and *Tarantola* [1987], which relies on the use of normalised and unnormalised probability density functions to express our knowledge about the values of parameters.

Thus, may $f(x)$ be the normalised density function for the value of a parameter x, then one can express the probability that x has a value between X and $X + DX$ as

$$P(X \leq x \leq X + \Delta X) = \int_{X}^{X+\Delta X} f(x)dx \tag{3.1}$$

In general, a geophysical inversion intends to find the values of a vector of unknown parameters $\mathbf{p}$ from the observed data set $\mathbf{d}$ and a known relationship $q(\mathbf{d},\mathbf{p})$ relating $\mathbf{d}$ and $\mathbf{p}$. Assuming that the density functions, which give the prior information on the model parameters $r_p(\mathbf{p})$ and on the observations $r_d(\mathbf{d})$ are independent and that the relationship between $\mathbf{p}$ and $\mathbf{d}$ can be expressed as a conditional density function $q(\mathbf{d}|\mathbf{p})m_p(\mathbf{p})$, then it is possible to express a complete, probabilistic solution as a posterior density function (**PDF**) $s_p(\mathbf{p})$ (Tarantola and Valette, 1982; Tarantola, 1987)

$$\sigma_p(\mathbf{p}) = \rho_p(\mathbf{p}) \int \frac{\rho_d(\mathbf{d})\theta(\mathbf{d}\,|\mathbf{p})}{\mu_d(\mathbf{d})} d\mathbf{d} \tag{3.2}$$

where $m_p(\mathbf{p})$ and $m_d(\mathbf{d})$ are null information density functions specifying the state of total ignorance.

Gaussian Error Assumption - L2-RMS likelihood function

The earthquake location problem is a 4D-problem with the hypocentral coordinates $x = (x, y, z)$ and the origin time T as unknown parameters. The observed data is a set of arrival times t, and the theoretical relation are given by predicted travel times h. Provided that the theoretical relationship and the observed arrival times have Gaussian uncertainties with covariance matrices $\mathbf{C}_T$ and $\mathbf{C}_t$, respectively, and if the prior information on T is taken as uniform, then it can be shown that it is possible to evaluate analytically the integral over d in (3.2) and an integral over origin time T to obtain the marginal PDF for the spatial location, $s(\mathbf{x})$ [*Tarantola and Valette*, 1982]. This marginal PDF reduces to [*Tarantola and Valette*, 1982; *Moser, van Eck and Nolet*, 1992]

$$\sigma(\mathbf{x}) = Kp(\mathbf{x})exp[-\frac{1}{t}g(\mathbf{x})] \tag{3.3}$$

$$g(\mathbf{x}) = [[\hat{\mathbf{t}}_0 - \hat{\mathbf{h}}\mathbf{(x)}]^T(\mathbf{C}_t + \mathbf{C}_T)^{-1}][\hat{\mathbf{t}}_0 - \hat{\mathbf{h}}\mathbf{(x)}]$$

In this expression K is a normalisation factor, $r(\mathbf{x})$ is a density function of prior information on the model parameters and $g(\mathbf{x})$ is an L2 misfit function. $\hat{\mathbf{t}}_0$ is the vector of observed arrival times $\mathbf{t}$ minus their weighted mean, $\hat{\mathbf{h}}\mathbf{(x)}$ is the vector of theoretical travel times $\mathbf{h}$ minus their weighted mean, where the weights w_i are given by

$$w_i = \sum_j w_{ij} \ ; \ \ wij = [(\mathbf{C}_t + \mathbf{C}_T)^{-1}]_{ij} \tag{3.4}$$

Furthermore, *Moser, van Eck and Nolet* [1992] show that the maximum likelihood origin time corresponding to a hypocentre at (x, y, z) is given by

$$T_{mi}(\mathbf{x}) = \frac{\sum_i \sum_j w_{ij}[t_i - h_i(\mathbf{x}]}{\sum_i \sum_j w_{ij}} \tag{3.5}$$

The posterior density function (PDF) $s(\mathbf{x})$ given by equation (3.3) represents a complete, probabilistic solution to the location problem, including information on uncertainty and resolution. This solution does not require a linearised theory, and the resulting PDF may be irregular and multi-modal because the forward calculation involves a non-linear relationship between hypocentre location and travel-times.

This solution includes location uncertainties due to the spatial relation between the network and the event, measurement uncertainty in the observed arrival times, and errors in the calculation of theoretical travel times. However, realistic estimates of uncertainties in the observed and theoretical times must be available and specified in a Gaussian form through $\mathbf{C}_t$ and $\mathbf{C}_T$, respectively. Absolute location errors due to incorrect velocity structure could be included through $\mathbf{C}_T$ if the resulting travel time errors can be estimated and described with a Gaussian structure. Estimating these travel time errors is difficult and often not attempted. When the model used for location is a poor approximation to the "true" structure (as is often the case with layered model approximations), the absolute location uncertainties can be very large.

Complete, Non-linear Location - PDF

The NLLoc grid-search algorithm systematically determines the posterior probability density function $s(\mathbf{x})$ or the "misfit" function $g(\mathbf{x})$ over a 3D, x, y, z spacial grid. The NLLoc Metropolis-Gibbs sampling algorithm attempts to obtain a set of samples distributied according to the posterior probability density function s(x).

The grid-search $s(\mathbf{x})$ grid, samples drawn from this function, or the samples obtained by the Metropolis-Gibbs sampling, form the full, non-linear spatial solution to the earthquake location problem. This solution indicates the uncertainty in the spatial location due to picking errors, a simple estimate of travel-time calculation errors, the geometry of the observing stations and the incompatibility of the picks. The location uncertainty will in general be non-ellipsoidal (non-Gaussian) because the forward calculation involves a non-linear relationship between hypocenter location and travel-times.

Because it is difficult or impossible to obtain, a more complete estimate of the travel-time errors (or, equivalently, a robust estimate of the errors in the velocity model) is not used. This is a serious limitation of this and most location algorithms, particularly for the study of absolute event locations.

The PDF may be output to a 3D Grid and a binary Scatter file (see Output below). PDF values are also used for the determination of weighted average phase residuals (output to a Phase Statistics file), and for calculating location confidence contour levels (see Output below), and "Traditional" Gaussian estimators (see below).

Maximum likelihood hypocentre

The maximum likelihood (or minimum misfit) point of the complete, non-linear location PDF is selected as an "optimal" hypocentre. The significance and uncertainty of this maximum likelihood hypocentre cannot be assessed independently of the complete solution PDF. The maximum likelihood hypocenter is also used for the determination of ray take-off angles (output to a HypoInverse Archive file), for the determination of average phase residuals (output to a Phase Statistics file), and for magnitude calculation. The ray take-off angles can be used for a first-motion fault plane determination.

Gaussian estimators

"Traditional" Gaussian or normal estimators, such as the expectation $E(\mathbf{x})$ and covariance matrix $\mathbf{C}$ may be obtained from the gridded values of the normalised location PDF or from samples of this function (e.g. *Tarantola and Valette*, 1982; *Sen and Stoffa*, 1995). For the grid case with nodes at $\mathbf{x}_{i,j,k}$,

$$E(\mathbf{x}) = \Delta V \sum_{ijk} \mathbf{x}_{ijk} \sigma(\mathbf{x}_{ijk}) \tag{3.6}$$

where DV is the volume of a grid cell. For N samples drawn from the PDF with locations $\mathbf{x}_n$,

$$E(\mathbf{x}) = \frac{1}{N} \sum_{n} \mathbf{x}_n \tag{3.7}$$

where the PDF values $s(\mathbf{x}_n)$ are not required since the samples are assumed distributed according to the PDF. For both cases, the covariance matrix is then given by

$$\mathbf{C} = E[(\mathbf{x} - E(\mathbf{x})(\mathbf{x} - E(\mathbf{x})^T] \tag{3.8}$$

The Gaussian estimators are output to the NNLoc, ASCII Hypocenter-Phase File (STATISTICS line).

Confidence Ellipsoid
The 68% confidence ellipsoid can be obtained from singular value decomposition (SVD) of the covariance matrix **C**, following *Press et al.* (1992; their sec. 15.6 and eqs. 2.6.1 and 15.6.10). The SVD gives:

$$\mathbf{C} = \mathbf{U}[diag w_{ij}]\mathbf{V}^T \tag{3.9}$$

where $\mathbf{U} = \mathbf{V}$ are square, symmetric matrices and w_i are singular values. The columns $\mathbf{V}_i$ of $\mathbf{V}$ give the principle axes of the confidence ellipsoid. The corresponding semi-diameters for a 68% confidence ellipsoid are Ö$(3.53w_i)$, where 3.53 is the Dc^2 value for 68.3% confidence and 3 degrees of freedom.

The Gaussian estimators and resulting confidence ellipsoid will be good indicators of the uncertainties in the location only in the case where the complete, non-linear PDF has a single maximum and has an ellipsoidal form.

3.5 Moment Tensor Inversion

To determine focal mechanisms from seismic broadband data, we used a time-domain iterative inversion method developed by *Kikuchi and Kanamori* that allows mechanism changes during the rupture sequence. The method is explained in detail elsewhere [*Kikuchi and Kanamori* 1982; 1986; 1991; 1993].

Focal mechanism solutions, like Global CMT or Harvard CMT, are often based on the simplification that a rupture process can be considered as a single point source. This approach allows to determine the overall fault mechanism, but may fail to reveal more complex rupture behaviour. For complex rupture and slip distribution it is more appropriate to describe the source process as a sequence of point sources (subevents), each specified by a moment tensor and its onset time and location [*Kikuchi and Kanamori* 1991]. In this case the overall moment tensor M is a linear combination of - in the most general case 6 - elementary moment tensors M_n:

$$M = \sum_{n=1}^{N_b} a_n M_n \tag{3.10}$$

with the coefficients a_n.

Let $x_j(t)$ denote the jth observed record and $\omega_{jn}(t,p)$ the Green's function due to the nth elementary moment tensor M_n, where t is the time and p is a parameter that represents both, the onset time τ and the location of the point source.

May $y_j(t,p)$ represent the synthetic waveform

$$y_j(t,p) = \sum_{n=1}^{N_b} a_n \omega_{jn}(t,p) \quad , \tag{3.11}$$

whereas the coefficients a_n and the parameter p can be obtained from the maximation of the correlation function between the observed and the synthetic waveforms

$$\Psi(p) = \frac{\sum_{j=1}^{N_s} \int \left[x_j(t) y_j(t,p)\right] dt}{\sum_{j=1}^{N_s} \int \left[x_j(t)\right]^2 dt} \quad , \tag{3.12}$$

where N_s is the number of used seismograms (Kikuchi and Kanamori 1991). Eq. (3.12) can be maximized via a grid search over all values of p, in which for the computation of overall fault mechanism and depth of a single point source p just represents the onset time τ and the depth z. Later, for the calculation of subevents, p will contain the locations l of the point sources as well.

To demonstrate this inversion procedure we will consider the event 062904B as example, for which we selected 21 vertical components of P-waveforms and 8 horizontal components of SH-waveforms (Table 3.2). Fig. 3.3b shows the distribution of the stations with good signal-noise-ratio. The coverage is good in the north, but poor in the south, which has been a common problem in this study. Moreover, the number of stations for waveform inversion is much more limited then for the phase data. This has different reasons. First, not all stations listed in the USGS NEIC catalogue operate broadband sensors; Second, in most seismograms it might indeed be possible to pick first arrivals, but the signal-to-noise ratio might be too poor for waveform modeling. Furthermore, since more stations require more processing time, it is not useful to pick more than a few representative stations out of a "cluster", like for northwest America or Europe. Further, we applied weight-factors on each station (Table 3.2) in order to “down weight“ cluster of stations and stations with poor waveform data.

The first step is to determine the representation of the overall fault mechanism in the elementary moment tensors and the depth of a single point source. Therefore, we computed Green‘s functions for eight discrete depths of 5 to 35 km under seafloor with an equal spacing of 5 km beneath the epicenter. We used an increment of 5 km, because, with a sampling interval of 1 s, the minimum depth increment to be resolved by depth phases such as pP and sP is 2 to 3 km [*Kikuchi and Kanamori* 1993] and since the coverage of stations shows large gaps, a maximum resolution of 5 km in depth reflects the error of the assessment. The obtained depth might vary from the hypocenter depth, which has been calculated in the relocation process, since the latter only gives the point of the first motion and the former may give the centroid depth of the entire fault motion [*Yamanaka and Kikuchi* 2003].

Table 3.2: List of station parameters.

Station	Network	Distance [*deg*]	Azimuth [*deg*]	Phase	Weight
IBBN	GE	84.5	37	P	1.0
KBS	GE	81.3	11	P	1.0
MORC	GE	89.9	38	P	1.0
WLF	GE	84.0	40	P	1.0
ALE	II	72.5	3	P, SH	0.8, 0.1
ASCN	II	74.7	101	P	0.8
ESK	II	77.8	35	P	1.0
FFC	II	45.4	347	P, SH	1.0, 0.2
KDAK	II	68.0	328	P, SH	0.8
PFO	II	35.3	314	P, SH	1.0, 0.2
ADK	IU	81.4	321	P	1.0
ANMO	IU	29.9	326	P	1.0
COLA	IU	68.2	336	P, SH	1.0, 0.1
COR	IU	45.9	323	P, SH	1.0, 0.2
KONO	IU	84.2	30	P	1.0
LVC	IU	37.6	151	P, SH	1.0, 0.6
MIDW	IU	85.3	297	P	1.0
RSSD	IU	36.4	339	P	1.0
SAML	IU	30.8	128	P	2.5
TRQA	IU	53.9	155	P	1.0
TUC	IU	30.7	318	P, SH	1.0, 0.2

The Green's functions were computed using *Kikuchi and Kanamori's* method [1982; 1991]. The near-source structure model used to compute theoretical waveforms is given in Table 3.3. It is a four-layer structure based on results from seismic refraction and wide-angle data [*Grevemeyer et al.* 2007]. Again, the ak135 1D Travel Time Tables [*Kennett* 1995] have been used as earth model.

Now, the overall fault mechanism is calculated by applying only a single point source together with a broad source time function [*Kikuchi and Kanamori*, 1991], for which we assumed a triangle function with a duration of 15s. Basically, this method leads to a Centroid Moment Tensor (CMT). These CMTs and the scalar moments, which we obtained with this method are shown in Table 3.4 for all events. Table 3.5 gives the corresponding fault mechanisms.

Seismic reflection data and bathymetry image that the bending-related faults dip $\sim 45°$ trenchwards with a strike of $\sim 120° - 130°$ [*Ranero et al.*, 2003], thus a distinction between fault and auxiliary plane could be done (e.g. for the event 062904B we established two solutions, one with a strike of 323° and a dip of 49° and one with a strike of 136° and a dip of 41°. The latter solutions meets the results of *Ranero et al.* [2003] suggesting that the former is the auxiliary plane). Thus, the

Table 3.3: Near-source structure.

V_p [km/s]	V_s [km/s]	Z [km]
1.50	0.00	3.0
6.70	3.74	6.0
7.20	4.10	10.0
8.40	4.40	–

V_p is the P-wave and V_s the SH-wave velocity, Z the thickness of the layer. The structure is based on results from seismic refraction and wide-angle data [*Grevemeyer et al.*, 2007]. It should be mentioned here that slide changes of this values do not influence the results of the calculations.

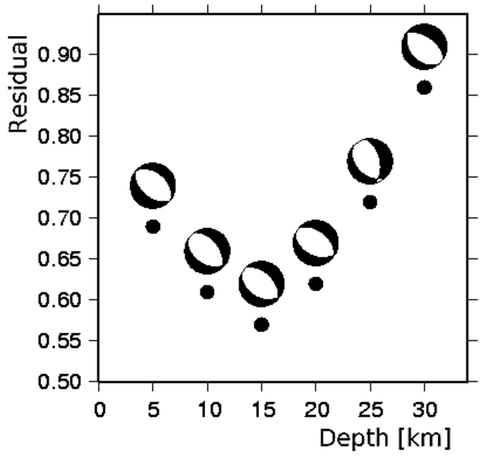

Figure 3.4: *Depth-dependency of the residual for a single point source for the 062904B-event and a time window of 40s starting from the first arrival. A depth of 15 km shows the best waveform-match.*

overall mechanisms are similar to the Harvard CMT solution (Table 3.5). Fig. 3.4 illustrates the determination of the centroid depth for the event 062904B. The best waveform match was obtained for a depth of 15 km. Table 3.5 shows these depths for all events.

3.6 Subevents

As indicated before, the complex rupture of a teleseismic event usually cannot be described by one point source alone, but by a sequence. Each point source is called a subevent.

To identify subevents we used a refined depth grid (Fig. 3.5) of 9 discrete depths with a spacing of 2.5 km and a dip according to Table 3.5 (dip of *our CMT*), where the centroid depths (Table 3.5) represent the central point of the grid. The 9 grid points had a spacing of 10 km on a line in strike-direction to determine the subevents

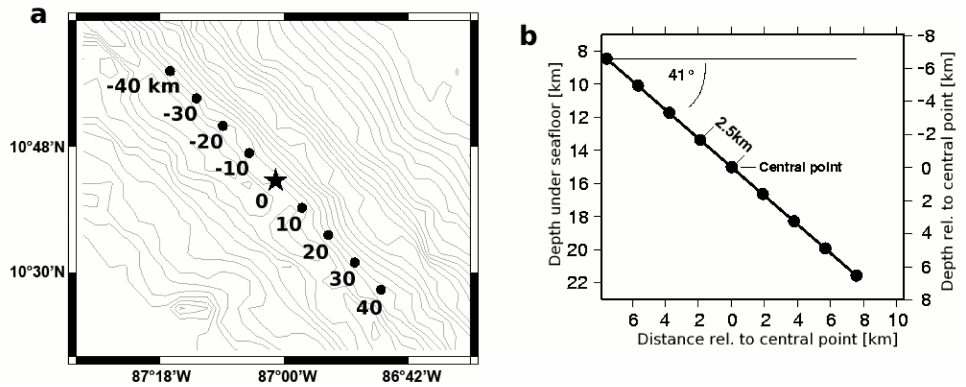

Figure 3.5: *Grid scheme for the inversion of the 062904B-earthquake. (a) 9 grid points are set up at equal spacing of 10 km on a line (strike of N44° W). The star denotes the epicenter after Table 3.1. (b) Depth grid.*

locations. This approach is based on the assumption that the entire rupture takes place on a plane which is equal to the CMT fault plane, so that all subevents will take place on a planar fault corresponding to the overall fault mechanism. This limitation is a consequence of the inversion code of Kikuchi and Kanamori, which does not allow a 3D gridsearch for subevents (which then could determine the fault plane). The number of possible solutions would be too large and hence instabilities would be introduced. Therefore, some additional information about the rupture process is required (Kikuchi and Kanamori 1991).

Now, an iterative procedure is executed, that introduces in every iteration a new subevent with an onset-time τ_i (time t and τ_i are discrete values with the increment of the sample rate), represented by a term $\sum a_{ni}\,\omega_{jn}(t,p_i)$, which maximizes the correlation function Ψ_i (eq. (3.12)), where i denotes the ith subevent ($i = 1, ..., N_i$; N_i = Number of subevents (iterations)), so in every new iteration i the observed record $x_j(t)$ in eq. (3) is replaced by a “new“ record

$$x_{ji}(t) = x_j(t) - \sum_{k=1}^{i-1}\sum_{n=1}^{N_b} a_{nk}\,\omega_{jn}(t,p_k) \quad , \tag{3.13}$$

which then is used as input for the next iteration.

The number of iterations after which a decrease in the residual is not observed determines the number of subevents. Fig. 3.6 illustrates the procedure for event 062904B. A single event cannot satisfy the observed waveform. The source time function must be very wide to explain the magnitude, which leads to a too wide and prominent first motion. Additionally, later peaks in the observed data cannot be explained. Four iterations are needed to satisfy the records. Additional iterations would not improve the least square fit. The final results for 062904B are shown in Fig. 3.7 and 3.8. The comparison of the observed and the synthetic waveforms shows a high degree of concordance (Fig. 3.7).

The total fault mechanism, which is now the sum of all subevents, changes only slightly (Table 3.5). The total seismic moment is $M_0 = 3.49x10^{18}Nm$ or $Mw = 6.3$,

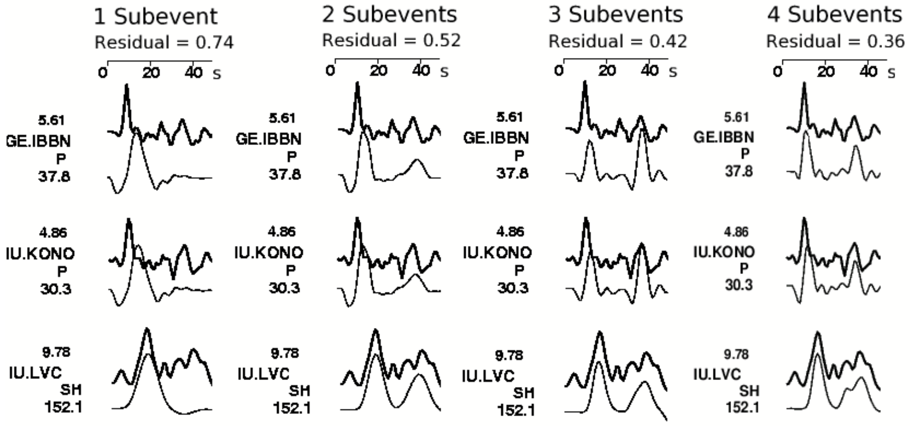

Figure 3.6: *Comparision between observed (upper) and synthetic waveforms for different stations and phases. Each column is the result of an inversion process with a different number of iterations (subevents). A further (significant) decrease of the residual cannot be observed after 4 subevents, which is also sufficient to obtain a good fit (Residual $\leq$ 0.4).*

which is consistent with the Harvard CMT solution. With time, however, the focal mechanism is changing from normal faulting to strike-slip. Final results for all other events are shown in Fig. 3.13-3.18.

3.7 Relocation of Subevents

As discussed previously, the inversion code of *Kikuchi and Kanamori* only allows 2D grid searches for subevents. To avoid this limitation, we tried to modify the inversion code algorithm by applying a 3D grid search. Unfortunately, a stable convergent behavior could not be achieved. The problem is already mentioned in outlines in *Kikuchi and Kanamori* [1986]. The non-linear and non-Gaussian character of the inverse problem leads to many local minima of the error Δ with respect to source parameters such as location. The path dependence of the solution is inevitable in any iterative method for non-Gaussian problems and there is no absolute criterion for choosing one solution against another. The only way is to try iterations for many different paths and choose the solution that is consistent with the *a priori* information. Thus, a 3D grid search leads to many solutions that fit the data equally well.

In order to find a way out of this dilemma, we decoupled the inversion for the focal mechanisms and onset times from the location process by using the NonLinLoc code to recalculate the location of the subevents in a 3D grid-search.

The first arrival observed at station j is associated with the first subevent $i = 1$. It's onset time can be randomly set to $\tau_1 = 0$. Every following subevent i with the onset time τ_i will occur at the time $(\tau_1 + \tau_{ij}) = \tau_{ij}$ at station j, whereas τ_{ij} most likely will differ from τ_i, since the locations of the point sources are shifting with the

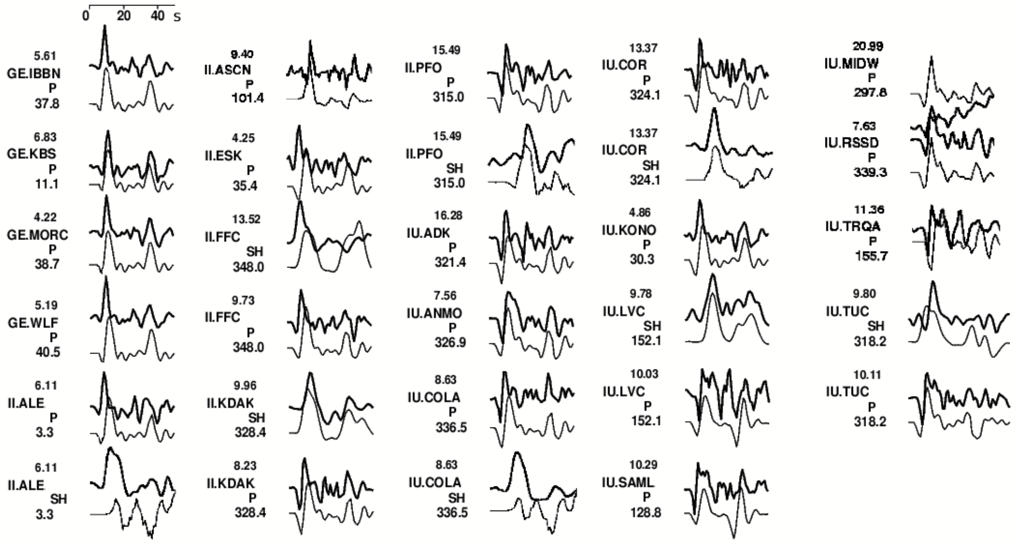

Figure 3.7: *Comparision between observed (upper) and synthetic waveforms for all phases used in the 062904B-inversion*

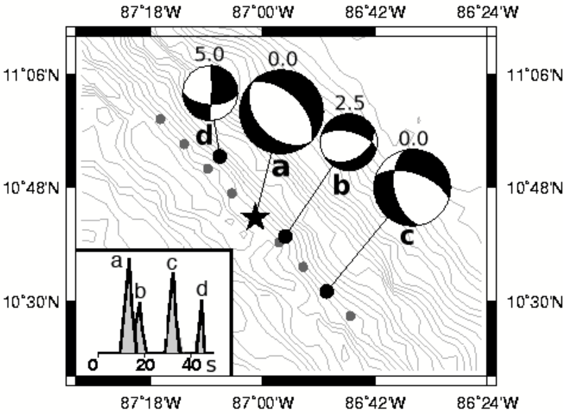

Figure 3.8: *Final result of the 062904B-inversion process. The grid scheme is the same as in Fig. 3.5. The letters beneath the focal mechanism diagram give the chronological order of the onset times of the subevents, the number above gives the depth relative to the centroid depth of 15 km (Table 3.5). In the down left corner the source time function is shown.*

rupture process.

Knowledge of the τ_{ij} for every station j and the azimuths and distances of the stations is already enough to calculate a location relative to the first subevent.

The moment tensor inversion provides us with synthetic waveforms for every station including the first arrival of every considered subevent. Admittedly, these first arrivals are the best-fit result of eq. (3.12), not the best-fit for every single station.

Instead of maximizing eq. (3.12), one can also obtain the coefficients a_n and the parameter p from the least squares criterion

$$\Delta = \sum_{j=1}^{N_s} \int \left[x_j(t) - \sum_{n=1}^{N_b} a_n \, \omega_{jn}(t,p) \right]^2 dt = min \tag{3.14}$$

As discussed above, a moment tensor solution does not depend on the particular grid, so we can presume that a_{ni} for all subevents are given by the inversion process and now solve eq. (3.14) independently for every summand

$$\Delta_{ji} = \int \left[x_j^{'}(t) - \sum_{n=1}^{N_b} a_{ni} \, \omega_{jn}(t,\tau_{ji}) \right]^2 dt \tag{3.15}$$

Here $x_j^{'}$ stands for the observed seismogram subtracted by the contributions of subevents 1,...,i-1. Note, that the Green's function here is just a function of time t and onset-time τ, since we assumed all source parameters, as source time function, near source structure and source depth to be fixed and the same as in the inversion. Hence, the relocation process here is a relocation of the epicenter only.

Subsequently, we carried out eq. (3.15) for a range of τ_{ji}, usually starting from $\tau_{ji} = \tau_{ji-1}$ to $\tau_{ji} = \tau_{ji-1} + 2\tau_i$ in steps of 0.5 s. Here, τ_{ji-1} is the onset time of the previous subevent at station j and τ_i is the onset time of the subevent under consideration from the inversion process. Then, the lowest value of Δ_{ji} determines τ_{ji} for subevent i and station j. An example is given in Fig. 3.9.

This method leads to different onset-times for every station and subevent, which we used as picks to calculate a location relative to the first subevent for every subevent using NonLinLoc. The method is similar to the Master Event Method [*e.g. Jackson and Fitch*, 1979]. The results are shown in Fig. 3.10, the step size for the grid search has been 0.01° in latitude and longitude.

One problem of this method is that it assumed that the parameters onset-time and moment tensor solution (focal mechanism) can be decoupled from the parameter location, hence that both sets of parameters are independent. This is not necessarily true. A change of the focal depth of a subevent may lead to a different focal mechanism which in turn can influence the onset time. This problem can be solved iteratively. Therefore we added to the inversion algorithm the possibility to set location parameters to fixed values. After finding initial focal mechanisms and onset-times, locations were determined for which in the next step "new" focal mechanisms and onset-times were calculated. In the present study, focal mechanisms and

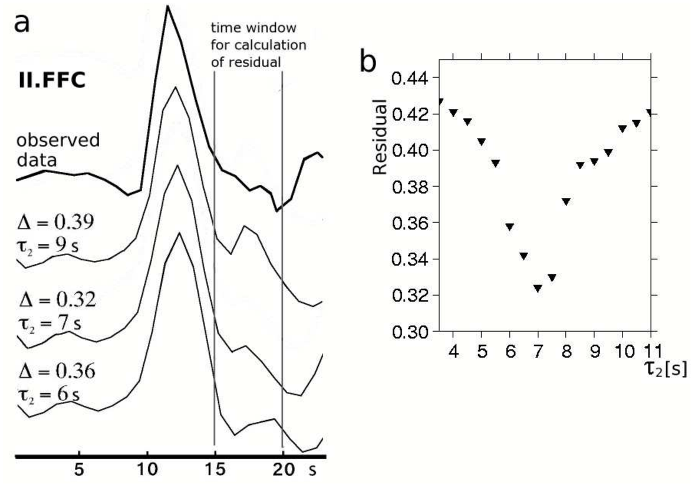

Figure 3.9: *(a) Observed seismogram (top) and synthetic waveforms for different onset-times of the second subevent (τ_2). (b) Residual Δ over onset-time τ_2 for station II.FFC and for the time window showed in (a) with a length of 5s. The inversion process led to $\tau_2 = 6s$ for this station, the minima obtained here is $\tau_2 = 7s$.*

onset times did not change during this iterative inversion procedure, which implies that the named set of parameters are mostly independent. This might be a result of the simple structure of the incoming plate.

However, the implementation of a powerful non-linear location code (NonLinLoc) made it possible to circumgo the non-convergent behavior of moment tensor inversion in three dimensions and therefore allow an estimation of the dimension of the fault plane by using the relative positions of all subevents.

3.8 Results

We relocated hypocenters for seven events from the trench-outer rise offshore of Central America using phase time data (Table 3.1). Epicenter locations are thorough, error ellipses are small and results from other catalogues mostly lay within these ellipses (Fig. 3.3). However, the phase time data included only few picks from surface reflections such as pP, sP, etc., since for shallow, large events recorded at teleseismic distances, it is almost impossible to distinguish between those and direct waves, which limits the depth resolution [e.g., *Dziewonski et al.*, 1981]. The error margins that we obtained for the hypocenter depths are much higher than those for the epicenter parameters. Statistical errors are usually in the range of ±15 km to ±50 km. Uncertainties given for the named catalogues are of the same order.

A better method to estimate hypocenter parameters is to find the centroid depth of a point source by moment inversion and waveform modeling. Thus surface reflections are automatically included. The surface reflection of a shallow event arrives shortly after the direct wave. Although its first movement cannot be identified, its contribution to the waveform plays an important role in the inversion process.

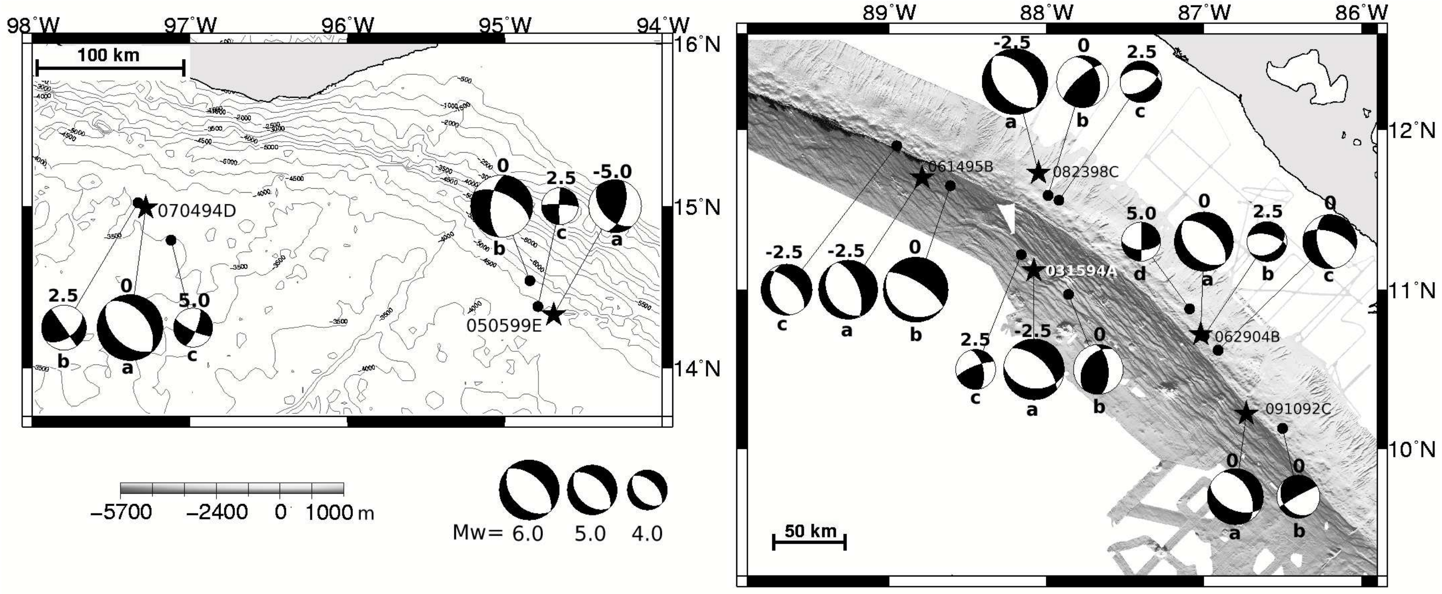

Figure 3.10: *Final results of the subevent-relocation process. The stars denote the epicentres of the first subevents, the numbers next to them accord to Table 3.1. The letters beneath the focal mechanism diagram give the chronological order in which the subevents occurred and the number above gives the depth relative to the first subevent (A negative value means a shallower depth. All depth from moment tensor inversion). Focal mechanism diagrams in one row belong to the same event.*

Fig. 3.4 illustrates that if one centroid depth minimizes the residual function, a change of ±5 km for this depth already leads to a significant increase of the residual. In consequence we estimate uncertainties for the centroid depths in Table 3.5 of $\pm 5 - 10$ km. However, hypocenter parameters in Table 3.1 and centroid depths in Table 3.5 coincide. Note that the hypocenter depth, which gives the location of the initial break and the centroid depth of the entire fault motion usually vary from each other. A good agreement between both depths could indicate a fault plane of small extension into depth.

Nevertheless, the calculation of centroid depths via waveform inversion may decrease uncertainties compared to location routines based on travel time pick, but has its limitations since the calculation of an overall fault mechanism with a single point source cannot reflect the waveform data (normalized residual is usually $\Delta \geq 0.7$, see Fig. 3.6) and disregards the details of the waveform.

More solid results are obtained from the determination of subevents. Here we used the depths from Table 3.5 as centroid points for a finer depth grid with a resolution of 2.5 km. Then, a grid search finds the locations for the subevents that lead to the best match between observed and synthetic waveforms. Assuming that the depths in Table 3.5 would be much to shallow, we would find subevents just on the lower grid points and we could not obtain a good residual (In general, $\Delta \geq 0.4$ can be considered "good"). Our results show subevents in the -5.0 km to 5.0 km around the centroid depths, even though the depth grid ranges from -10 km to 10 km. The normalized residuals are between $\Delta = 0.29$ for event 050599E and $\Delta = 0.44$ for event 091092C for a 50s-cutout counting from the first arrival, whereas the latter is the only one that exceeds $\Delta = 0.4$.

Now, the location of the first subevent in chronological order is conform with the hypocenter, but a limitation of the used moment tensor inversion codes made it necessary to define a 2D fault plane on which all subevents occur *a priori*. All attempts to use a 3D grid search led to a non-convergent behavior and introduced instabilities. In order to deal with this problem we used fault solutions for all point sources to determine arrival times for each subevent at each station. These arrival times we used to calculate precise locations of the subevents relative to each other.

3.9 Discussion

Teleseismic waveform inversion for earthquakes occurring in the Middle America Trench suffers from a gap in the distribution of stations in the Pacific ocean, and perhaps from the simplification introduced by a 1D Earth model. Nevertheless, we could demonstrate that all events in this area are very shallow and that rupture is propagating downdip in most cases.

It is interesting to note that the rupture sequences of all events but 061495B show a change in mechanism from normal faulting to strike-slip or oblique thrusting. This feature, however, is a robust result and not introduced by the inversion procedure itself. Fig. 3.11 illustrates the results of a test. The inversion code by *Kikuchi and Kanamori* allows mechanism changes but also has an option to fix the mechanism.

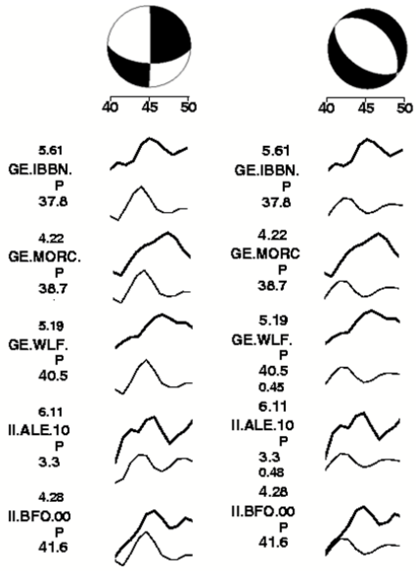

Figure 3.11: *Comparision between observed (upper) and synthetic waveforms for two different mechanism for the fourth subevent in the 062904B-event. The left column shows the results of the inversion: a strike-slip subevent can explain the waveform. A neglect of possible changes of the focal mechanism with time and hence the assumption of a normal fault mechanism (consistent with the overall fault mechanism) for the fourth subevent cannot reflect the observed waveforms.*

For 062904B, we executed a run with a fixed mechanism for all subevents. The first three subevents we set to the obtained values from section 3.7 and the fourth and last subevent we set to the overall mechanism from section 3.5 ((strike(Φ), dip(δ), rake(λ)) = (136°, 41°, -96°)). In both cases the onset-time of the fourth subevent is found to be 41 s after the first arrival. In Fig. 3.11 we show observed and synthetic waveforms for the subevent, for a strike-slip (left column) and a normal faulting mechanism (right column). As one can see, the introduction of normal faulting leads to a clear difference between observed and synthetic data, while the strike-slip motion improves the fit.

Such a behavior provides the possibility to estimate the dimension of the fault plane from the distribution of the point sources alone. Usually this is not possible, since a point source only represents the location of an initial break, but tells nothing about how much further the rupture propagates. In the present case five of the seven investigated earthquakes start to rupture down-dip as normal faults and end as strike-slip (rupture in strike-direction) or thrust-faults (up-dip). Therefore, the distance in dip-direction between the shallowest point source and the deepest one gives an estimated for the rupture width. The distance in strike-direction between the two furthermost point sources provides an estimate for the rupture length, only in this case we do not know how much further the rupture continued. In consequence we obtain the minimum rupture length. Via the results from the relocation process for the subevents we find rupture widths of $W = 5$ km to 10 km and minimum rupture lengths of $L_{min} = 25$ km to 50 km. The rupture width seems to be independent of the magnitude. In contrast, the largest event (082398C with Mw=6.7) shows the smallest minimum rupture length ($L_{min} = 25 km$), which might confirm that the actual rupture length is much greater. The subsequent minimum aspect ratios are in the range of $L_{min}/W = 3$ to 10.

Dowrick and Rhoades [2004] investigated 129 earthquakes from 4 different regions and found only 17 events with $L/W \geq 10$. The bulk of the data does not exceed $L/W = 6$. Rupture areas are between 40 km^2 and 400 km^2 for events of magnitudes M_w= 5.5 to 6.5. The latter corresponds with our results, but taking into consideration that the actual aspect ratios for events in this study might be much higher, fault planes of trench-outer rise events offshore Central America seem to be unusually long and narrow.

Accurate centroid depths [Table 3.5] derived from moment tensor inversion show values between 10 km and 25 km below seafloor. (Only for the event 091092C a centroid depth of 30 km was found. However, this event shows also the highest uncertainty and is therefore excluded from the consideration). Combined with the narrow fault planes it follows that large outer rise events offshore Central America are restricted to the upper 15 km to 30 km of the incoming plate.

Seismic images published by *Ranero et al.* [2003] suggest that faults offshore Nicaragua penetrate 10-15 km in to the mantle. Focusing on that area, we can easily estimate the maximum penetration depth into the mantle for those events, which occurred seawards the trench. In that case we only need to subtract the Moho depth of 5 km to 6 km from the entire rupture depth, whereas the latter is given by centroid depths and width of the fault plane. Provided that the centroid depth is located at the upper part of the fault plane (which is unrealistic, since the centroid of the entire fault motion is rather located somewhere in the middle of the fault plane then at its edge), the maximum possible rupture depth can be calculated by adding the width of the fault plane multiplied with the cosine of the dip angle.

Fig. 3.10 shows that two events (031594A and 061495B) occurred seawards the trench. Those events are also amongst the shallowest (Table 3.5) with centroid depths of 15 and 10 km respectively and dip angles of 46° and 38° respectively. We did not use the dip angles from the CMT solution in Table 3.5 for this calculation, since those represent only an average over all dip angles of all subevent. An inversion involving a strong change of focal mechanism as it is the case for the 031594A event cannot provide a realistic overall dip angle. It seems a more appropriate choice to use dip angles of the main shock (the largest subevent) instead. For both events we find rupture plane widths of less than 5 km and in consequence that these rupture penetrate 8 km to 14 km into the mantle. It might therefore be reasonable to hypothesize that seismically imaged faults [*Ranero et al.*, 2003] coincide with the rupture plain of large outer rise normal fault events.

As mentioned in the introduction, *Chapple and Forsyth* [1979] proposed a model in which the bending stresses in the incoming plate produce a tensional and a compressional region, both separated by a neutral nodal plane. They found a global average depth for the neutral plane of 30 km to 40 km, whereas their investigation of one thrust event offshore Central America suggests a shallower tensional region.

They argued that the lithosphere here is much younger and the plate likely much thinner. The focal depth, which they found for the compressional Middle America event, was 19 km. This falls within the range of the depth in which our inversions show the reported change of mechanism. It seems that the focal mechanism changes from normal (tensional) to strike-slip or thrust faulting when the rupture front strikes the nodal plane. A large normal fault event that ruptures the surface may provide a pathway for seawater to penetrate the mantle as suggested by *Ranero et al.* [2003], but a compressional regime could present a barrier. In consequence thrust faulting may occur at greater depth than any depth derived for the earthquakes in this study, but those fault may remain dry. *Ranero et al.* [2003] suggested that the reflectivity of bending-related faults is cause by hydration. Thus, dry compressional faults are perhaps not prominent in seismic reflection data.

Christensen and Ruff [1983; 1988] suggested a model in which the depth of the neutral nodal plane varies both temporally and spatially. They found that after a large underthrusting earthquake the coupling between the incoming and the continental plate can be weakened and tensional stress from slab pull is transferred to the outer rise. In Fig. 3.12 we plotted events listed in *Harvard CMT* which occurred before those in our study. All events are thrust fault events with focal depths shallower than 90 km. Most likely they are megathrust or interplate events, since earthquakes due to the dehydration of the incoming plate occur at greater depths [*Green and Houston* 1995; *Kirby et al.* 1996; *Hacker et al.*, 2001]. This suggests that all events in this study occur after a partial decoupling of the incoming and the continental plate and therefore are slab pull related. In consequence the depth of the neutral nodal plane found in this study might be greater than it is after the occurrence of a large normal fault outer rise event or before a large thrust event. An interesting question is what would happen to seawater that penetrates during the rupture into a region that is tensional at present, but compressional afterwards. Would it be forced out? However, the good match between our estimation for the depth of the neutral plane and the depth down to which faults are seismically imaged [*Ranero et al.*, 2003] suggests that almost the entire tensional regime as we see it during a normal fault rupture is hydrated.

3.10 Conclusion

It has been shown that large trench-outer rise earthquakes offshore Central America occur at very shallow depths (<30 km). Strike and dip of these events are consistent with the geometry of the bending-related faults, as it is determined from seismic reflection data and bathymetry. Further, normal fault events at the trench-outer rise seem to occur after large thrust faults events and hence are expected to be related to slab pull.

The rupture processes of normal fault earthquakes is characterized by subevents; a change of the focal mechanism with time from normal fault to strike-slip was observed, provided that the rupture moved unambiguous downdip. This is best explained by a change of the stress field in the lithosphere, which might present the intersection between the upper, tensional and the lower, compressional area. This intersection, which approximately is located ∼8 km to 14 km below the Moho, may also present a threshold for seawater to penetrate any deeper. This depth corresponds roughly to the depth of normal faults derived from seismic images [*Ranero et al.* 2003].

This study presents seismological evidence for a depth of fracturation that may facilitate water penetration in the mantle of the Central American Subduction Zone and underlines existing seismic refraction and reflection data. In other subduction zones, where seismic images suggest hydration of the incoming mantle as well, e.g. at the North Chile trench [*Ranero and Sallares*, 2004], the presented methods may provide further insights into trench-outer rise processes and mantle hydration.

Table 3.4: Moment tensor for all events

			Centroid Moment Tensor [$10^{18} Nm$]				M_0
Event	M_{zz}	M_{xx}	M_{yy}	M_{zx}	M_{zy}	M_{xy}	$10^{18} Nm$
091092C	-0.807 ± 0.033	0.544 ± 0.021	0.263 ± 0.018	0.089 ± 0.210	0.057 ± 0.137	-0.391 ± 0.014	0.82
031594A	-0.339 ± 0.017	1.021 ± 0.016	-0.682 ± 0.021	-0.302 ± 0.187	-0.546 ± 0.120	-0.995 ± 0.097	1.48
070494D	-4.757 ± 0.021	0.590 ± 0.024	4.167 ± 0.017	-1.397 ± 0.261	0.451 ± 0.174	-1.920 ± 0.082	5.10
061495B	-6.235 ± 0.025	2.260 ± 0.036	3.974 ± 0.026	1.480 ± 0.259	-3.152 ± 0.153	-3.065 ± 0.051	7.17
082398C	-12.078 ± 0.014	9.701 ± 0.022	2.378 ± 0.015	0.758 ± 0.413	-3.515 ± 0.227	-5.537 ± 0.036	12.9
050599E	-1.636 ± 0.019	1.583 ± 0.017	0.053 ± 0.010	0.083 ± 0.174	-0.511 ± 0.144	-0.555 ± 0.021	1.78
062904B	-3.417 ± 0.010	1.411 ± 0.012	2.006 ± 0.010	0.137 ± 0.113	-0.536 ± 0.131	-1.699 ± 0.007	3.47

M_{xx} etc. are defined by *Kanamori and Given* [1981].

Table 3.5: Centroid depths and fault mechanisms

	Centroid	our CMT			Sum of Subevents			Harvard CMT		
Event	Depth [km]	Strike	Dip	Rake	Strike	Dip	Rake	Strike	Dip	Rake
091092C	30	132	44	-80	126	41	-89	135	24	-68
		298	47	-100	303	49	-91	292	68	-99
031594A	15	74	71	-158	64	73	-148	109	46	-109
		336	69	-20	324	61	-30	316	47	-71
070494D	25	144	52	-106	139	49	-98	147	45	-103
		349	41	-71	330	42	-82	345	47	-78
061495B	10	137	31	-100	134	37	-110	127	34	-99
		328	59	-84	338	55	-76	318	56	-84
082398C	20	106	41	-109	111	43	-100	120	45	-106
		311	52	-73	305	48	-80	322	47	-74
050599E	15	93	43	-113	121	39	-102	111	49	-106
		303	51	-70	317	52	-80	313	44	-73
062904B	15	136	41	-96	133	42	-99	124	52	-98
		323	49	-85	328	49	-82	317	39	-80

For each event, the first row gives the fault plane and the second one the auxiliary plane.

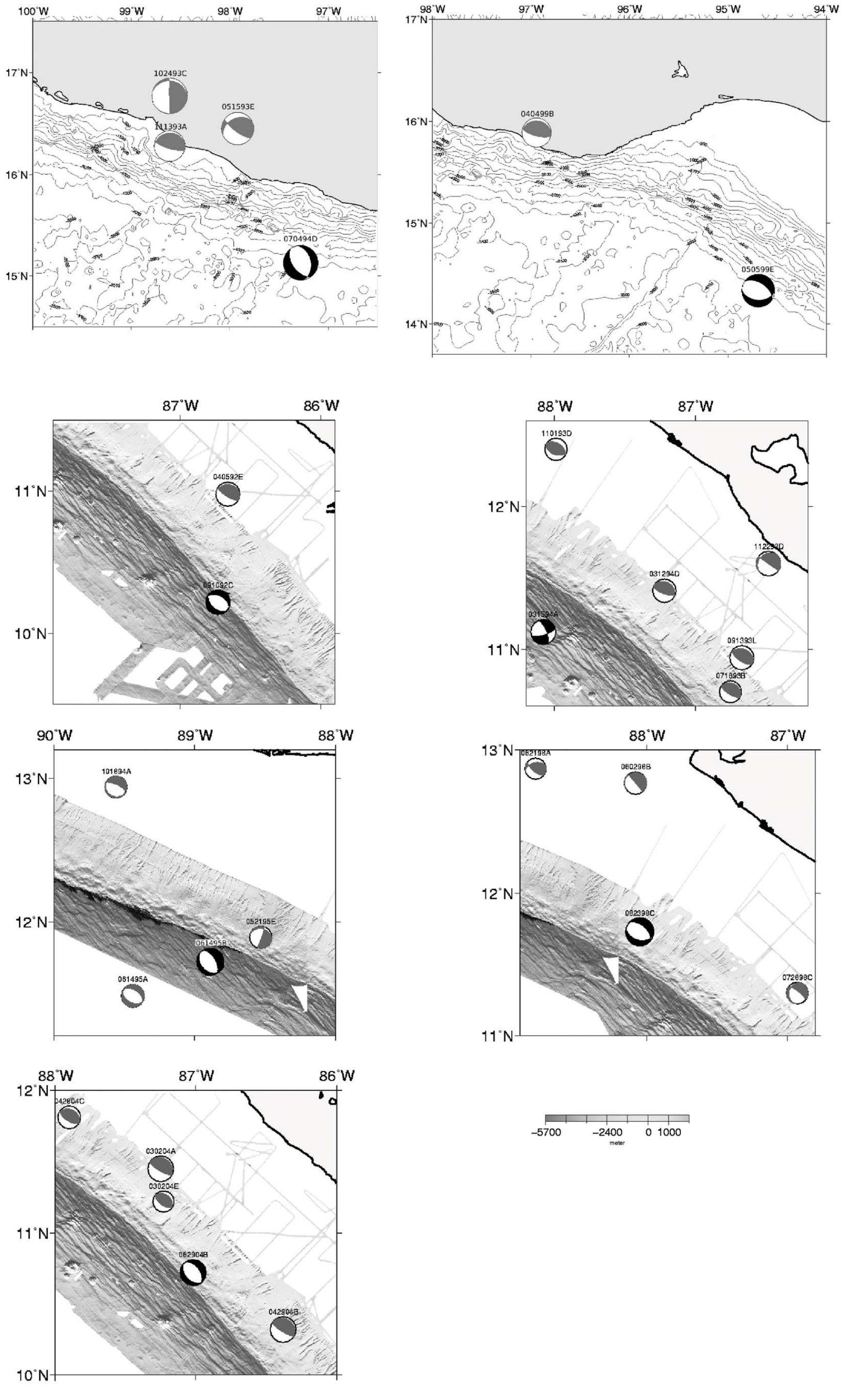

Figure 3.12: *Earthquake history of all seven events in this study. Grey focal mechanisms are 'Harvard CMT' solutions for teleseismic events, which occurred before events investigated in this study (black focal mechanisms after Tables 3.1 and 3.5)*

3.11 Appendix

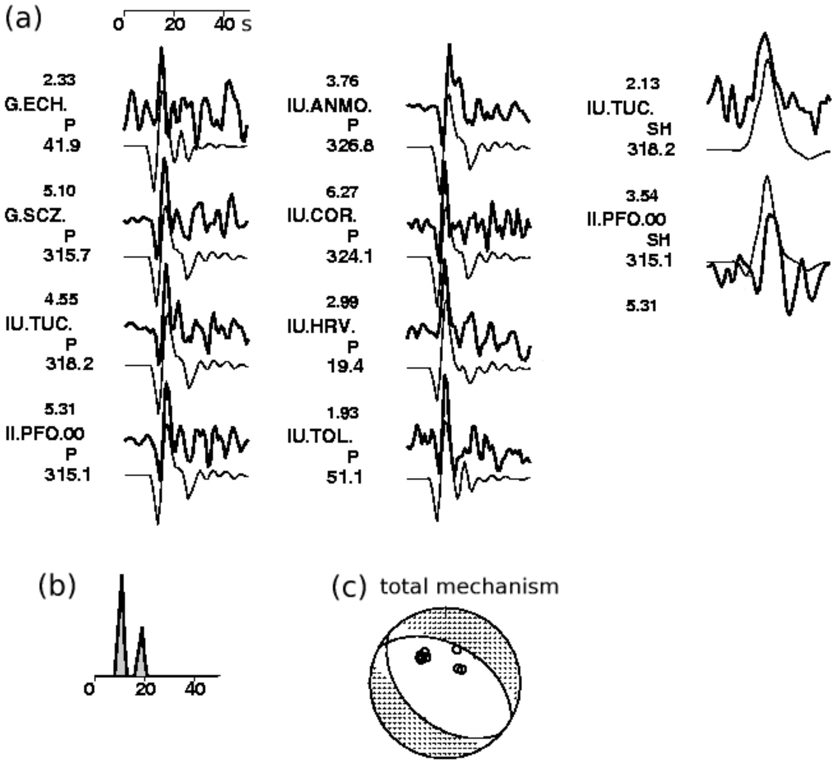

Figure 3.13: *Comparision between observed (upper) and synthetic waveforms for all phases used in the 091092C-inversion*

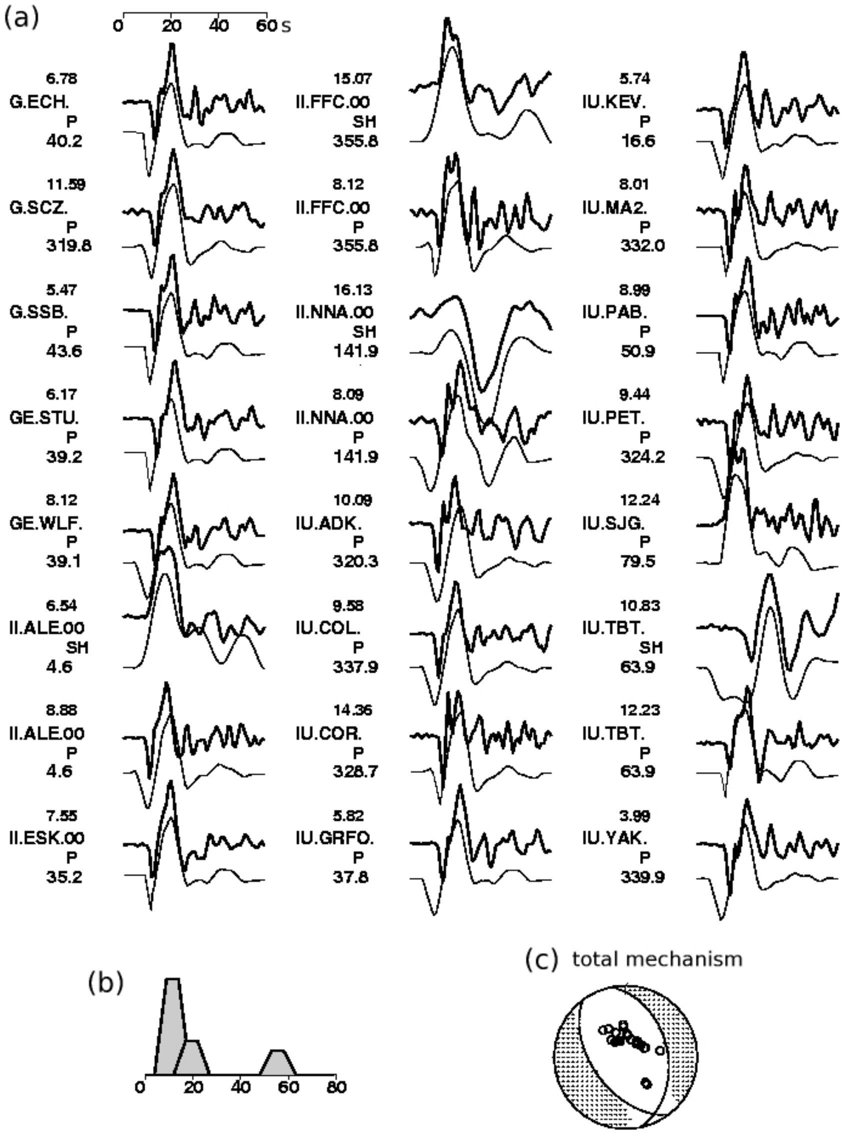

Figure 3.14: *Comparision between observed (upper) and synthetic waveforms for all phases used in the 070494D-inversion*

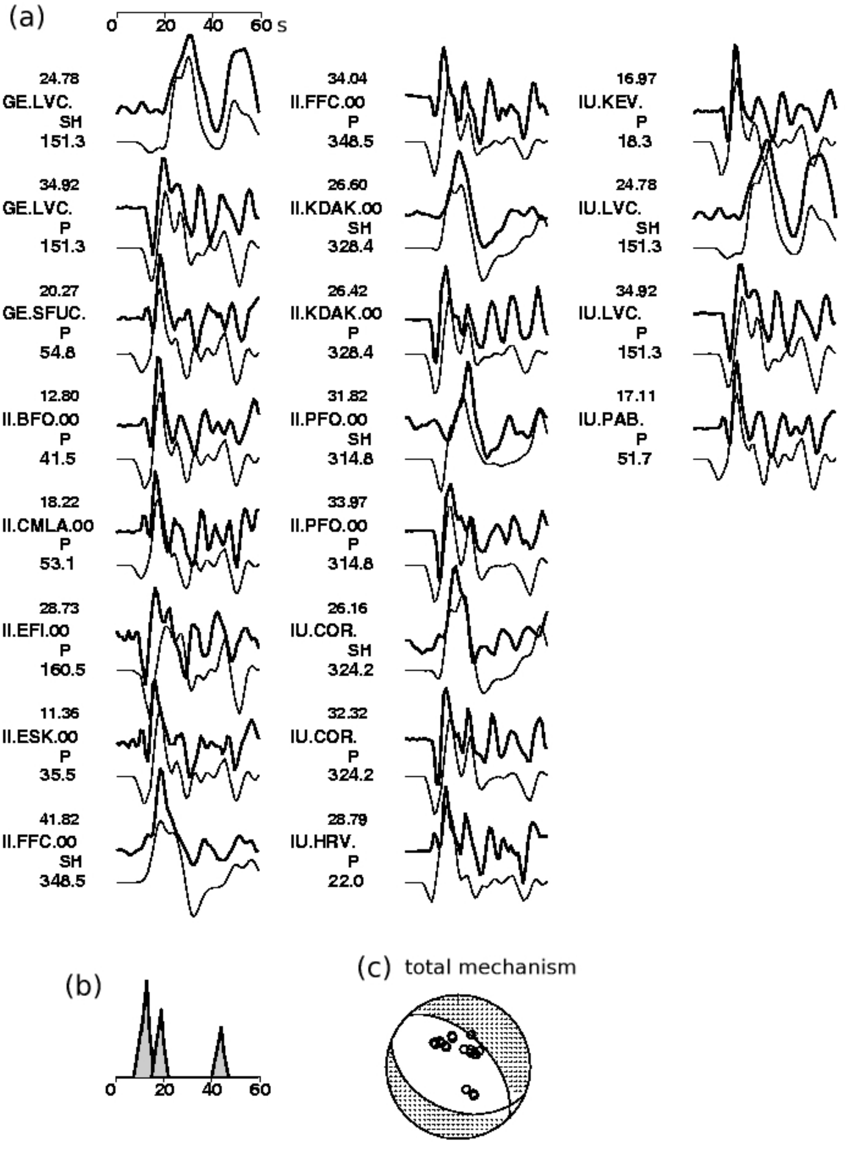

Figure 3.15: *Comparision between observed (upper) and synthetic waveforms for all phases used in the 082398C-inversion*

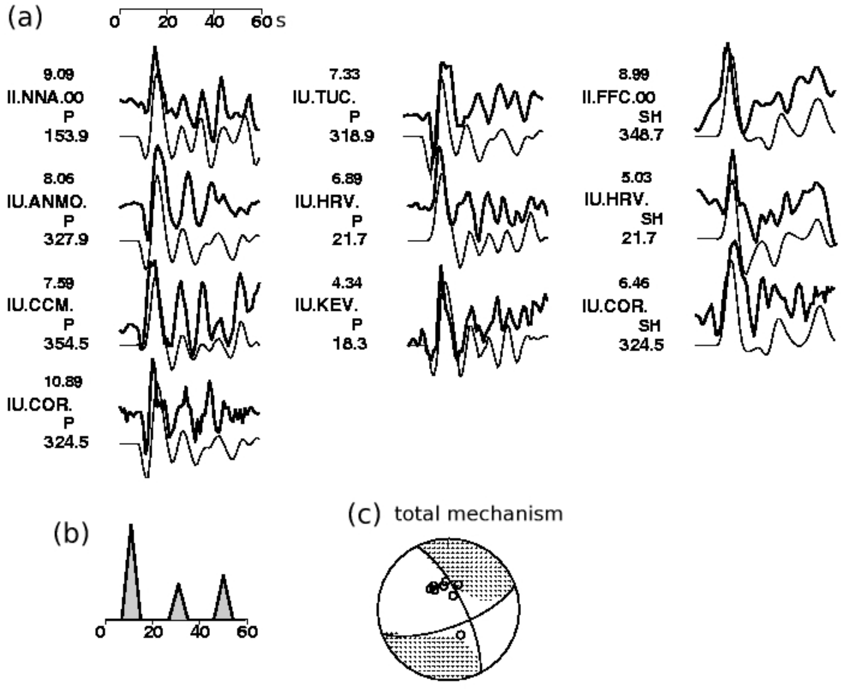

Figure 3.16: *Comparision between observed (upper) and synthetic waveforms for all phases used in the 031594A-inversion*

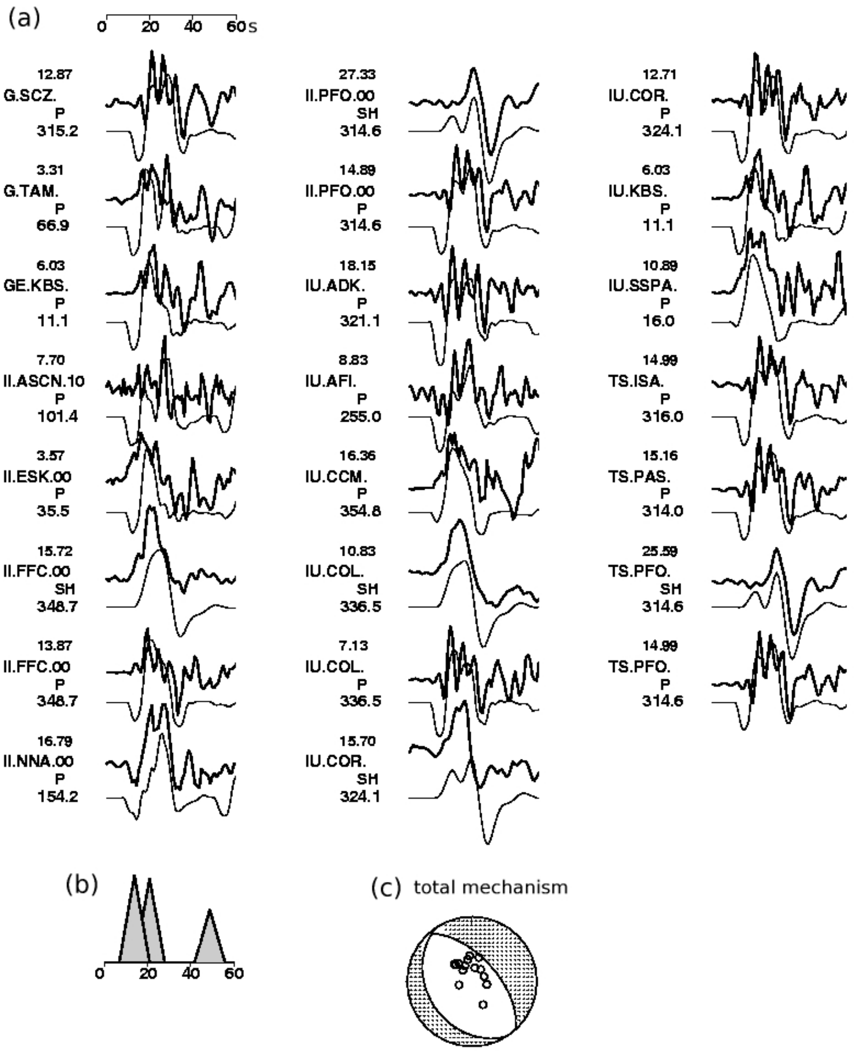

Figure 3.17: *Comparision between observed (upper) and synthetic waveforms for all phases used in the 061495B-inversion*

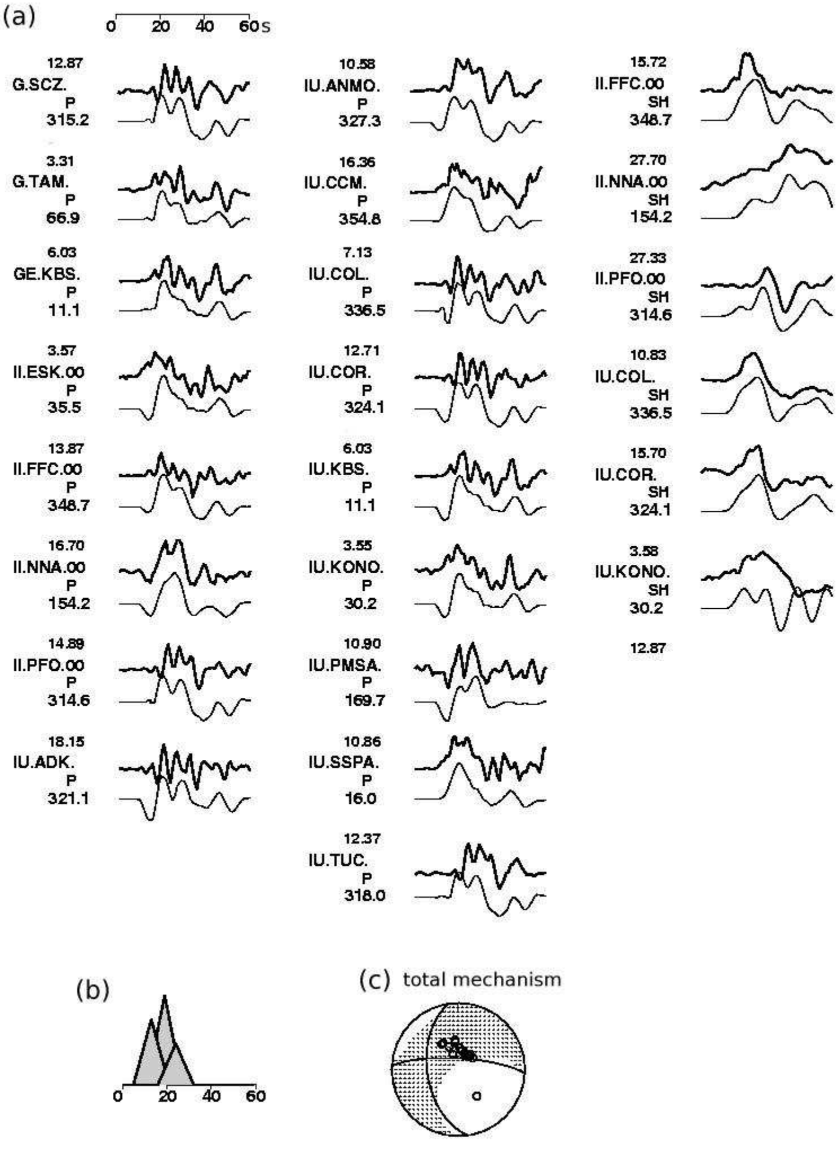

Figure 3.18: *Comparision between observed (upper) and synthetic waveforms for all phases used in the 050599E-inversion*

Chapter 4

Local Seismicity

At subduction zones, the bending of the incoming oceanic plate leads to a reactivation or creation of normal faults [*Christensen & Ruff*, 1988; *Hasegawa et al.*, 1994], which have been inferred to cut deep enough into the mantle to provide a pathway for seawater to penetrate into the lithosphere [*Ranero et al.*, 2003], changing "dry" peridotites to "wet" serpentinites [*Peacock*, 2001; 2003]. Such a mechanism would present an efficient system to transport fluids into the slab and therefore would influence a wealth of subduction zone processes, as dehydration at depths of 50-300 km can trigger intermediate-depth earthquakes [*Meade & Jeanloz*, 1991; *Kirby et al.*, 1996] and promotes melt generation under volcanic arcs [*Rüpke et al.*, 2002].

We present results from a unique data set obtained from a dense, local seismic monitoring network deployed in the trench-outer rise. A joint inversion of airgun shots, local earthquakes within or nearby the network and well-located regional earthquakes at distances of 200-700km allow us to constrain a velocity model that reflects almost the entire lithosphere. We document a relation between bending-related faults and trench-outer rise seismicity, but state that micro-seismicity reaches deeper than the area of reduced mantle velocity and hence possible serpentinization. We explain the latter with a change of the stress regime from tensional at the top of the incoming lithosphere to compressional beneath, as we infer from the determination of focal mechanism for a number of events. Seawater might not be able to penetrate into an area governed by compressional stresses. In consequence, all numbers for serpentinization that have been named so far need to be scaled down.

4.1 Introduction

Understanding the Earth's water budged requires an understanding of the amount of water carried into a subduction zone. While water in open pore spaces of sediments or igneous crust is released at shallow depth, chemically-bound water trapped in sediments or lithosphere will be carried to greater depth [*Rüpke et al.*, 2002], where it affects a wealth of subduction zone processes, including intraslab earthquakes [*Meade & Jeanloz*, 1991; *Kirby et al.*, 1996] and arc magmatism [*Rüpke et al.*, 2002]. The subduction of water into the deep Earth's interior is inherently linked to the hydrogeology and alteration of the incoming lithosphere [*Wallmann et al.*, 2001;

Jarrard et al., 2003]. Growing evidence suggests that much of the hydration of oceanic plates occurs at the trench-outer rise slope right before subduction [*Peacock*, 2001; *Ranero et al.*, 2003; *Grevemeyer et al.*, 2007; *Ivandic et al.*, 2007]. Here, normal faults are created while the rigid lithosphere bends into the trench; normal faulting produces earthquakes that cut down to mantle depth [*Christensen & Ruff*, 1988; *Hasegawa et al.*, 1994]. Water trapped in the mantle may alter mantle peridotites to serpentinites, providing a major source for chemically-bound water to be subducted to greater depth [*Ranero et al.*, 2003].

High-resolution multibeam bathymetry [*Ranero et al.*, 2003] offshore of Nicaragua and seawards of the Middle American Trench, where the oceanic Cocos Plate is subducted beneath the Caribbean Plate, shows that bending-related faulting is pervasive across most of the trench-outer rise slope (Fig. 4.1). Single faults are tracked in the bathymetry for at least 50 km and multi-channel seismic reflection (MCS) data suggest that they cut up to 15 km into the mantle [*Ranero et al.*, 2003]. Heat flow data *Grevemeyer et al.*, 2005] suggest that this area is characterized by a reactivation of the ridge flank hydrothermal circulation system. Trench-outer rise normal faults may facilitate infiltration of seawater into the lithosphere. For Nicaragua, geochemical data from the volcanic arc suggests that mafic magmas have water concentrations among the highest in the world [*Roggensack et al.*, 1997], supporting the idea of mantle hydration prior to subduction. Furthermore, regional P-waves from Nicaraguan intraslab earthquakes occurring at 100-150 km depths show high-frequency late arrivals, which could be caused by a 2.5-6 km thick low-velocity layer in the incoming plate. Such velocity anomalies in areas of great depths and pressure can be explained by >5 wt% of water in the subducted crust, which means a hydration degree which is 2-3 higher than inferred for other slabs [*Abers et al.*, 1979].

Following Chapple and Forsyth [*Chapple & Forsyth*, 1979] the bending of the uppermost lithosphere of the incoming oceanic plate can be described as the downward flexure of a thin elastic plate, leading to a tensional regime at the top of the plate, grading into a compressional one at the bottom, both separated by a neutral plane. In this model trench-outer rise earthquakes and hence fracturing of the incoming plate are a consequence of flexure. Supported is this by global compilations of earthquake mechanisms based on waveform inversion, since tensional, normal faulting events occur in general in the uppermost 25 km of the incoming lithosphere, while compressional fault behaviour dominates at greater depth [*Seno et al.*, 1987; 1996]. In the particular case of the Central American subduction zone, the tensional regime seems to be shallow compared to global averages. Centroid depth of a single compressional event in the area [*Chapple & Forsyth*, 1979] occurred at 19 km and interpretation of teleseismic broadband data suggests a change of the stress regime at 10-15 km beneath Moho [*Lefeldt & Grevemeyer*, 2007]. An explanation to this might be the comparable young age and the subsequent thin lithosphere of the Cocos Plate. However, the given numbers may suffer from significant uncertainties, since large teleseismic events at the trench-outer rise are rare [*Lefeldt & Grevemeyer*, 2007] and in general it is difficult to determine hypocentre parameters for shallow events in the ocean [*Yoshiba et al.*, 1992].

Recently published seismic refraction and wide-angle data from the trench-outer rise off Nicaragua [*Grevemeyer et al.*, 2007; *Ivandic et al.*, 2006] were able to resolve the upper 3-5 km of the mantle and show reduced P-wave velocities starting approximately 50 km seawards of the trench, where bending-related faults become a highly visible feature in the bathymetry. Seismic velocities of the uppermost mantle are 7.6-7.8 km/s and hence 5-7% lower than the typical velocity of mantle peridotite. Seismic velocities in the uppermost mantle decrease systematically towards the trench hence indicating an evolutionary process [*Ivandic et al.*, 2006] consistent with percolation of seawater through the faulted and fractured lithosphere and serpentinization of mantle peridotites. If hydration indeed affects seismic properties serpentinization reaches 12-17%, suggesting that roughly 1.5 to 2.5 wt% of water is chemically-bound in the uppermost 3-5 km of the mantle [*Grevemeyer et al.*, 2007; *Ivandic et al.*, 2006], where active source seismic data provide enough resolution. However, deeper penetration of seismic rays into the upper mantle is needed to yield better estimates for the flux of water carried with the subducting oceanic slab into the Earth's interior. Seismic sources in the mantle and seismic rays transiting the mantle seaward of the trench axis, both recorded in the trench-outer rise, are required to resovle the structure of the mantle down to approximately 30 km.

Inspired from this idea, a dense earthquake-monitoring network was installed seawards the Middle America Trench offshore of Nicaragua. High quality recordings of 68 local earthquakes within the latitude-longitude range or in the close surroundings of the network (we will call them "local sources") were used to obtain accurate hypocentre locations and a three-dimensional velocity model via an iterative inversion scheme (see supplementary material), including additional 39 regional sources far outside of the network (Fig. 4.1) resolving the entire region of the lithosphere that might be affected by bending-related trench-outer rise faulting. In addition, active source seismic data have been used to resolve the shallow structure and the crust/mantle transition zone.

4.2 The Outer Rise Network

The Outer Rise Network (ORN) was deployed during the RV Meteor M66/3 cruise in September 2005 and recovered after 58 to 61 days. Altogether, 21 instruments provided data, among 10 ocean bottom seismometers (OBS), each equipped with both a hydrophone and a three-component seismometer and 11 ocean bottom hydrophones (OBH). All sample frequencies were 100 Hz or 125 Hz. The distances between the instruments were 15 to 25 km and in total the network is covering an area of 120 km by 110 km (Fig. 4.1).

4.2.1 Time Correction

A problem in ocean bottom seismology is to correct the internal clocks of the recorders for deviation during the period of deployment. The best approximation is to set the clock of each recorder to GPS time, once before the deployment and a second time right after the recovery to determine the deviation for the whole period of deployment, which is assumed to be a linear drift. This assumption is justified, since for any particular clock the deviation from the nominal rate is primarily dependent on the temperature which is almost constant at the seafloor and the time spent on deck and sinking or rising, during which large temperature variations can be experienced, is short compared to the time on the seafloor.

Most stations had a drift of less than 100ms over the entire two month period, even though some stations had drifts up to 480ms. Station obs18 showed a time leap of ∼30s. Arrival times of the first events that have been recorded shortly after deployment showed that the leap occurred prior to those events. Nevertheless, stations obh17, obs18, obh20 and obh21 showed a linear increase of the absolute value of the residual with time (Fig. 4.2), meanwhile the distribution of residuals over times seems to be randomly for all other stations (Fig. 4.3). The linear component has been removed (Fig. 4.2).

4.2.2 Relocation

Where a refraction profile passed directly over the station, the stations were relocated in the profile-parallel direction by fitting the water wave arrival times from airgun shots near the station. This was the case for all stations except obh17, obh20, obh21, obh23 and obh24 (cp. Fig. 4.1)

4.2.3 Seismic Data Processing

To identify earthquakes in the continuous data stream an automatic trigger routine has been applied that considers only events that have been simultaneously observed, at least at 4 stations within a 3-minute time window. A total number of 1911 events were detected this way. Any further processing of the data was done manually.

In a first pass any event that showed an interval of more than 20s between the first P-wave arrival and the S-wave arrival has been neglected, since it is far outside of the network and a calculation of the hypocenter is not accurate anymore due to the azimuthal gap of stations. Afterwards, even events with records from less than 6 stations have been ignored. In a second pass, regional events from cataloges (cp. 4.2.4) that could be identified in the ORN data set have been reintegrated.

For 297 events a preliminary location could be found (Fig. 4.4) using the linear earthquake location program HYP from the SEISAN earthquake analysis software package [*Havskov and Ottemöller*, 1999] and a preliminary 1D-velocity model (Table 4.1) based on seismic refraction data [*Grevemeyer et al.*, 2007].

4.2.4 Regional Seismicity

We received accurate hypocenter parameters for 85 regional earthquakes [*Syracuse*, 2006], which occurred on- and offshore Nicaragua and Costa Rica over the period of deployment of the ORN. All of these events could be identified in the ORN data set.

Table 4.1: Velocity structure for a preliminary calculation of hypocenters. [a]

Layer no.	depth[b] [km]	V_P [km/s]
0	0	1.6
1	0.4	4.5
2	1.4	5.4
3	3	6.4
4	6	7.2
5	7	7.7
6	10	7.9
7	13	8.0
8	15	8.1
9	20	8.2
10	30	8.3
11	50	8.4

[a] V_P/V_S-ratio of 1.8 has been used for all layers.

[b] The depth of a layer is the starting point from which the velocity V_P is applied, measured from the seafloor.

In order to perform a 3D-tomography inversion we chose only those events from the data set, which fulfil the quality requirements that the first *P*-wave arrival can be picked at minimum 10 stations with an accuracy of <100ms. This was possible for 57 events.

Further, we retrieved approximately 230 regional events with magnitudes of Mw=0.6 to 6.0 that have been recorded and located across Central America by the Instituto Nicaraguense de Estudios Territoriales (INETER). Unfortunately, only land stations were used for the location process. In consequence, hypocenter parameters for offshore events suffer from a gap in the azimuthal distribution of station and therefore have been excluded.

The intersection between the both named data sets shows a good agreement for the hypocenter parameters. 17 more events have been included from the INETER catalog.

4.2.5 Wide-angle and Refraction Data

At the end of the duration of the ORN, three seismic wide-angle and refraction profile have been shot (Fig. 4.1). When line 01 was shot, all stations were still recording. We were able to receive "3D-information" by picking the first arrivals of *Pn*-phases from shots on line 01 at stations that were not part of this line. Further, we picked several *Pg*-, *PmP*- and *Pn*-phases from line 03. This profile has exceptional importance for this study since (1) its central position leads to a high resolution (cp. 4.3.3) and (2) it is perpendicular to the trench and hence might show the evolutionary character of a low velocity anomaly.

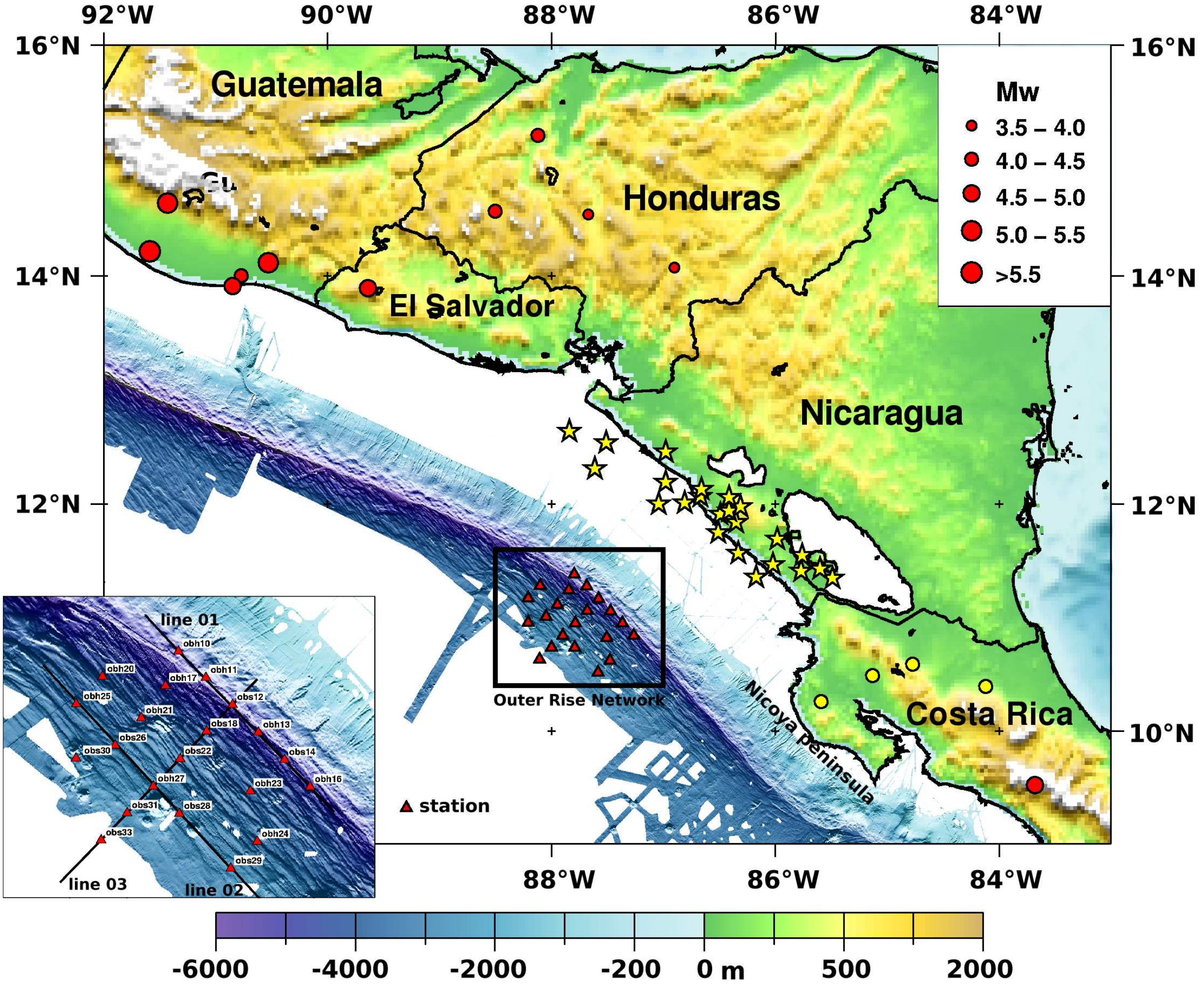

Figure 4.1: *Location of the Trench-Outer Rise Network (ORN) and distribution of regional sources added to the tomographic inversion. Red circles denote earthquakes recorded and located by Instituto Nicaraguense de Estudios Territoriales (INETER), yellow stars and circles events that have been located by Syracuse et al. [2006]. Arrival times of events denoted with a yellow star might be influenced by the cold sinking slab, which shows higher seismic velocities than its surroundings and therefore might favour stations closer to the trench. To account for this, we used an accurate P-wave velocity model for the entire slab [Dinc-Akgodan et al., 2007] to calculate travel times within the inversion process. Red triangles show the positions of the stations used in this study. At the end of the deployment of the ORN, three seismic wide-angle and refraction profiles have been shot (line 01 - 03). The ORN was installed in this specific area, since existing multichannel bathymetry [Ranero et al., 2003;] suggested a simple nature of the bending-related faults (i.e. strike of the faults is parallel to the trench axis, no occurrence of massive ridges, etc.), which allows an accentuation of bending-related fault processes.*

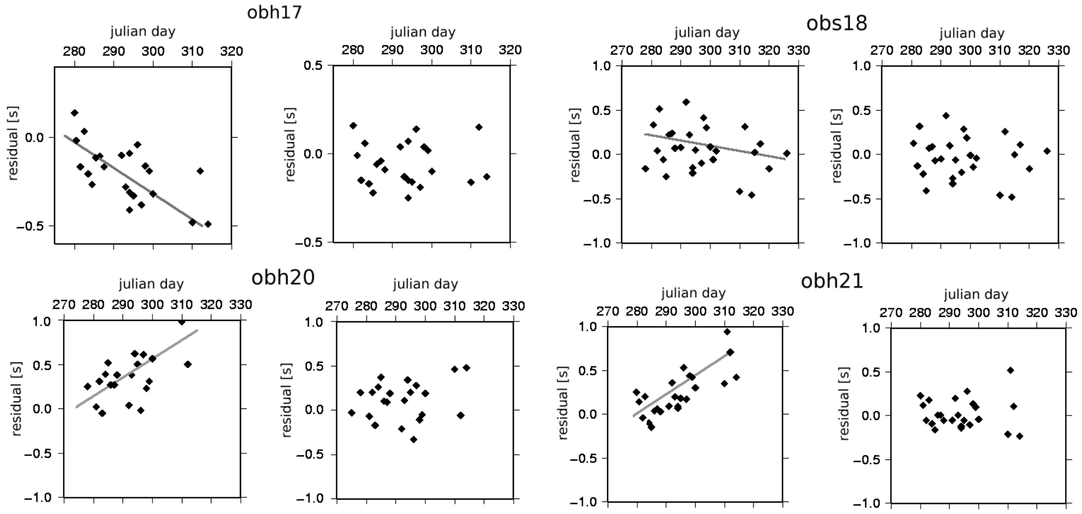

Figure 4.2: *Residuals between observed first arrival travel times and synthetic travel times (final calculation with fmtomo) over duration of deployment. For all plotted stations a linear trend (grey line) was observed (left plot). After a removal of the linear drift, a new calculation with fmtomo was carried out (right plot).*

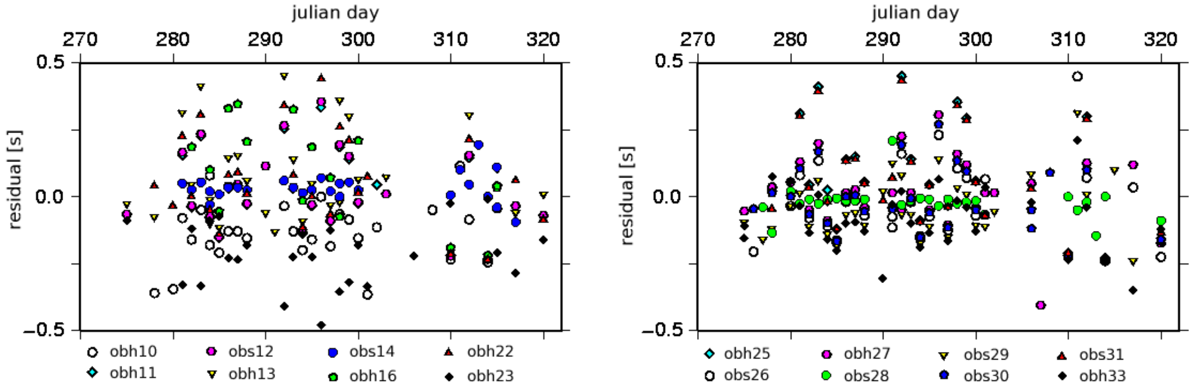

Figure 4.3: *Residuals between observed first arrival travel times and synthetic travel times of final calculation with fmtomo. All stations, which did not show a linear trend over time, are plotted.*

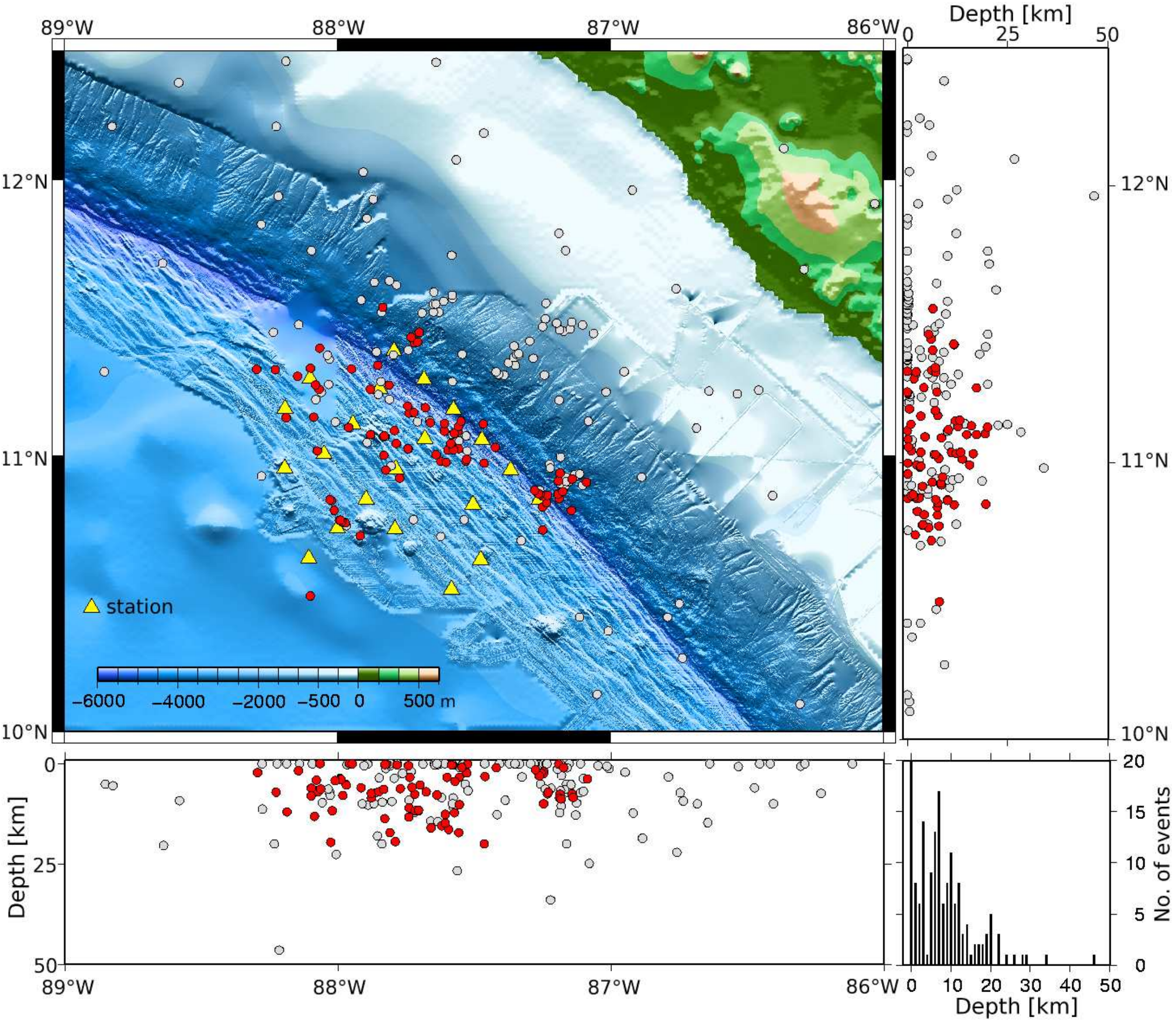

Figure 4.4: *Seismicity over a two-month period as observed by the ORN experiment. Red circles denote events for which accurate hapocenter locations could be found. Gray circles show the remaining earthquakes. The events have been located using the HYP code and a preliminary velocity model (Table 4.1). The depth always denotes depth beneath seafloor. All stations have been set to a depth of 0 km, in order to keep the calculation simple. The total number of events for a depth between 0 to 1 km is 56.*

4.3 Hypocenter Locations and 3D Velocity Model

In most earthquake localization routines the velocity parameters must be known *a priori*, e.g. from active seismic tomography. Then, the observed travel times are minimized by changing the hypocenters, which represent the only free parameters, while the velocity model is kept constant. However, the travel time of a seismic wave depends on both, the seismic velocities sampled along the ray paths and the hypocenter parameters [*Husen et al.*, 1999]. Keeping one of these sets of variables fixed will most likely introduce systematic errors [*Thurber*, 1992; *Eberhart-Phillips and Michael*, 1993]. Generally speaking, the calculation of hypocenters from travel time data is a non-linear problem, with the velocity model and the hypocenters as variables and is called the coupled hypocenter-velocity model problem [*Crosson*, 1976a; *Kissling*, 1988; *Thurber*, 1992]. Thus, an accurate hypocenter calculation requires the simultaneous inversion for the hypocenters and the velocity structure.

4.3.1 *P*-wave Minimum 1D-velocity Model

A minimum 1D-velocity model was obtained by using the software routine VELEST [*Kissling et al.*, 1994; 1995].

Even though almost 300 events have been located using a preliminary velocity model, by far not all of them are of use for the inversion process, since a stable and accurate inversion generally demands a data set of high quality. In the present case the latter means that only those events, for which an accurate calculation of the hypocenter is even possible, should be taken into account. Events, which have been observed at too few stations or which show a large azimuthal gap of observations will always show a significant uncertainty in hypocenter parameters even if the velocity structure is perfectly known.

In order to satisfy the named conditions, events that were recorded at less than 8 stations or showed an azimuthal gap of $\geq 220°$ were excluded from the data set, which leaves a total number of 68 events, with 722 P-wave observations and 197 S-wave observations.

Both the velocity model that minimizes the average RMS values of all events, and refined hypocenter parameters are calculated in an iterative inversion procedure, whereat the number of iterations has to be increased until an appreciable decrease in the all-over RMS cannot be observed anymore.

For most applications it is of advantage that VELEST allows for station elevation, which implies that each ray is traced to the absolute position of each station. The shallowest station in the ORN was at 2820 m below sea level meanwhile the deepest one was at 5296 m below sea level, which gives a station topography of approximately 2.5 km.

The current version of VELEST requires that all stations are located in the first layer, resulting into a top layer of 2.5 km thickness with a constant velocity. This is rather unrealistic since the study area is characterized by a thin sediment layer of about 380 m thickness [*Kimura et al.*, 1997], with a very low average velocity of 1570 m/s in the upper 180 m (hemipelagic sediment) and additional a thin crust

[*Ivandic et al.*, 2006; *Grevemeyer et al.*, 2007] of 5.5 to 6 km with a velocity gradient from 4.2 km/s to 6.7 km/s. Further, the strong velocity gradient in the sediments and upper crust would most likely introduce systematic errors and cause numerical instabilities if a thick top layer is used [*Husen et al.*, 1999]. In addition, seismic refraction data [*Ivandic et al.*, 2006; *Grevemeyer et al.*, 2007] suggest that the basic structure (thickness of sediments, depth of Moho, etc.) is the same beneath any station. Hence, even if it would be possible to place stations in different layers with different velocities, it would still be inappropriate since it would suggest that the basic structure beneath the stations would be different for varying station depths. Therefore, it seems to be much more appropriate to neglect station elevations.

The first step of the inversion process is to find an appropriate layering for the P-wave inversion. Therefore, different layer thicknesses are tested with a wide range of realistic and unrealistic initial velocity models. After the inversion, the final model should have the same values independently from the initial model. Are instabilities observed, the model needs to be refined, show two following layers the same velocity, they can be merged in order to lower the numerical effort. Fig. 4.5 shows a layer test for a thick first layer and allowance of station elevations. A wide range of initial models leads to a wide range of final models.

A better convergence is achieved when a refined upper layer thickness is used and station elevations are neglected (Fig. 4.6). Various initial models (Fig. 4.6a) all show convergence below 7 km beneath sea floor (Fig. 4.6b). Above convergence is not well constrained.

Most likely this is a result of both, the neglect of station elevations and the strong decrease of crustal velocities towards the trench [*Ivandic et al.*, 2006]. Since crustal velocities in this area are known from seismic wide-angle and refraction data, a combination of average velocities from active seismic tomography for the crust and of the 1D velocity model for the mantle provides a very reliable velocity structure.

P-wave station corrections are shown in Fig. 4.7. Negative travel time residuals refer to an early arrival compared to the reference station, meanwhile positive values imply a late arrival.

The final P-wave 1D velocity model (Table 4.2) was obtained after 9 iterations with VELEST. The final all-over RMS is 205ms, which is acceptable low. The initial model consists of average velocity values from active seismic for the crust (Table 4.1, layer 2-6) and assumed values for the mantle.

4.3.2 S-Wave Pick Time Data

In most earthquake location routines the S-wave velocity model is constrained by assuming a constant V_P/V_S-ratio, even though it has been shown that focal-depth errors may be twice as large compared to the errors using only P-phases [*Maurer and Kradolfer*. 1996].

However, a well-constrained and independent S-wave model can contribute to the hypocenter locations and can increase the accuracy of focal depths. Only, it is much more difficult to pick the arrival of an S-wave than to pick a P-phase, since the onset of the S-wave most likely occurs within the P-wave coda and therefore

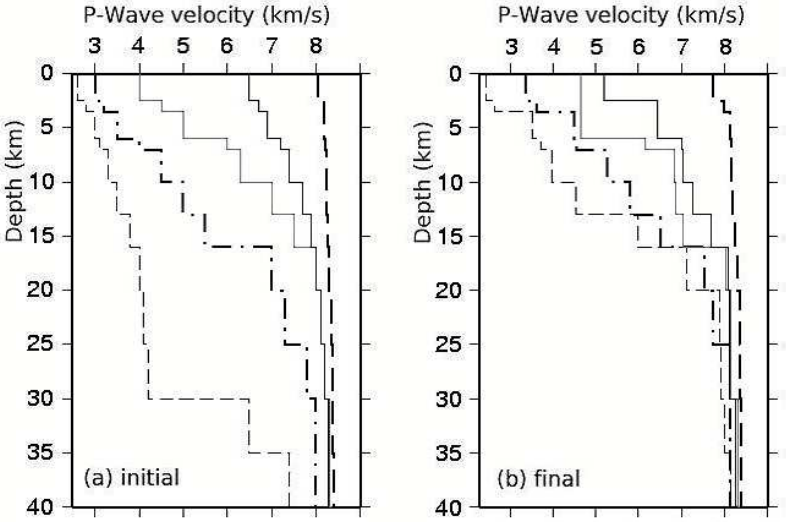

Figure 4.5: *Initial (a) and final (b) P-wave velocity model after inversion with a thick first layer and with station elevations. The convergence is not satisfying due to the large thickness of the top layer.*

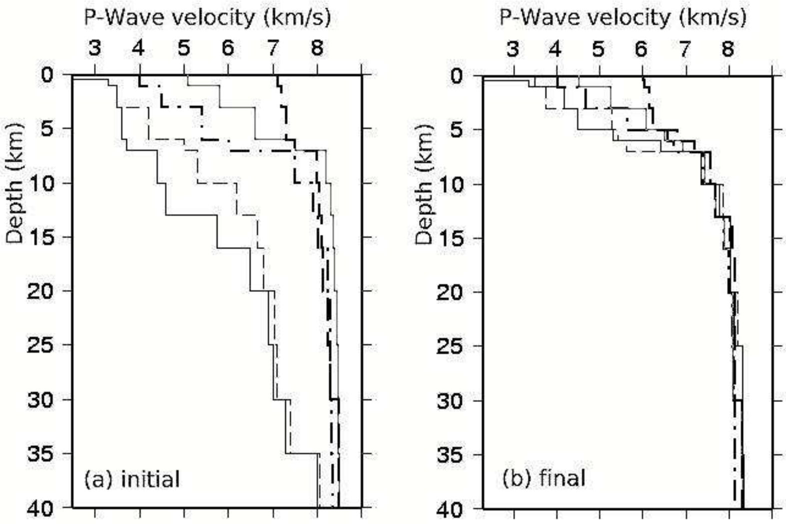

Figure 4.6: *Initial (a) and final (b) P-wave velocity model after inversion with a refined upper layering and neglect of station elevations. Convergence is given below 7 km, just in the upper layers only the velocity gradient can be resolved and not absolute values.*

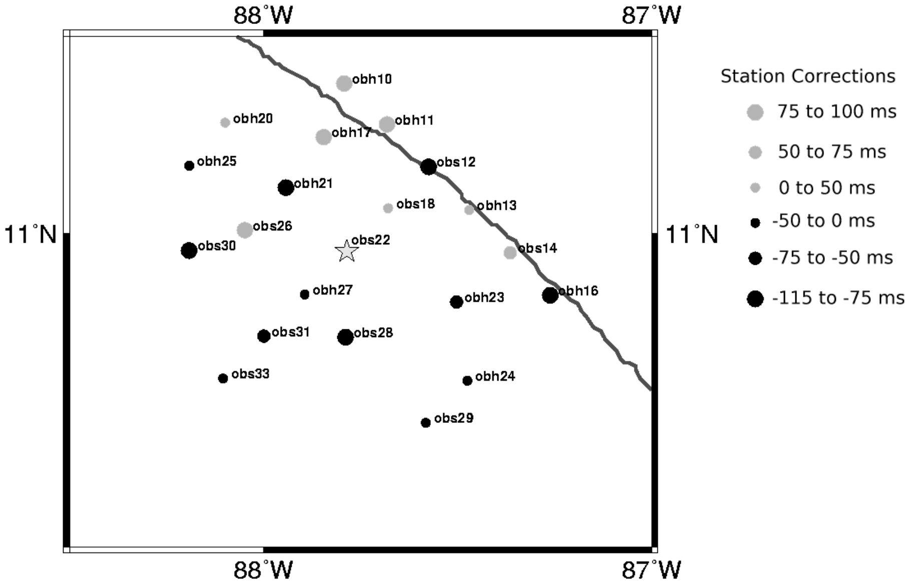

Figure 4.7: *P-wave station corrections for the final 1D velocity model. The star denotes the reference station obs22.*

is covered or distorted. One way to decrease the possibility of mispicked S-phases is to rotate and integrate the horizontal components. However, the attitude of the seismometers on the ocean bottom is not known, hence rotation is not possible. But, a wrongly picked S-wave, arrival time easily can result in a wrong hypocenter solution, but regardless with a small RMS. Furthermore, again only events of good quality can be included into the calculations, which means e.g. at least 8 P-wave and 4 S-wave observations and a gap in the azimuthal distribution of stations of $<180°$. Only 18 events fulfilled these terms, which is a very small number. Also, S-wave arrivals from regional sources are of no use for us, since we do not possess a reliable S-wave velocity model for the subduction zone. For these reasons, we did not consider S-Wave pick time data.

4.3.3 3D-tomography

We retrieved the Fortran 90 software package FMTOMO[1]. The program uses a relatively new tomographic inversion scheme, which (1) solves the forward problem of travel time calculation via a multi-stage fast marching method (FMM), which is a sophisticated grid-based eikonal solver and (2) solves the inverse problem of adjusting model parameters to satisfy data observations and any imposed regularization by using a subspace scheme, which minimizes an objective function simultaneously along multiple search directions that together span a subspace of model space. The method is described in detail in [*Rawlinson et al.*, 2006; 2007].

The first step is to define and to parameterize the model volume, i.e. the volume

---

[1] http://rses.anu.edu.au/∼nick/fmtomo.html

in which P-wave velocities can be changed by the inversion process . All local sources must lay within this volume. In FMTOMO, velocity is represented by a regular grid of points with cubic B-splines applied to define a continuum. We introduced 12 equal spaced grid points in north-south and in east-west direction and defined for the model volume the same borders as given by Fig. 4.18. Focal depths for all local sources calculated with the minimum 1D-velocity model show a range of 0.0 km to 17.4 km beneath seafloor, respectively 4.9 km to 22.7 km beneath sea level. Since hypocenter parameters are expected to change in the 3D tomography inversion, we defined a larger depth range of 0.0 km to 30 km for the model volume and introduced 60 grid points with an equal spacing of 0.5 km. Since FMTOMO automatically adds a cushion of boundary nodes, the total number of grid cells is $(12 + 2) * (12 + 2) * (60 + 2) = 12152$.

Then, an input velocity model was created by combining the P-wave minimum 1D-velocity model with multibeam bathymetry data [*Ranero et al.*, 2003]. For every surface grid point of the model volume, the depth of the seafloor was received from the multibeam bathymetry and starting from this depth the 1D-velocity model (Table 4.2) was applied. Fig. 4.11 shows a cross section through the input model. The described high quality data set of 68 local sources with 722 P-wave observations has been used for the 3D inversion as well, whereat start values for the hypocenter parameters (Fig. 4.11) are obtained from the final step of the 1D inversion. 513 P-wave arrivals from regional sources as well as picks from 853 Pg-Phases, 653 PmP-Phases and 1198 Pn-Phases (cp. 4.2.5) have been added to the data set.

When solving the forward problem, FMTOMO routinely calculates the total travel time from source to receiver for events outside of the model volume (regional or teleseismic events) by embedding the model volume into the ak135 travel time tables [*Kennett et al.*, 1995]. However, the inversion process only deals with arrival time residuals, which are equal to the arrival times minus the predicted arrival times from a global reference model. Further, FMTOMO provides the option to remove the mean of arrival time residuals associated with each source, which leads to relative arrival time residuals. A test series, which we carried out proved that the latter is very robust against perturbations of the hypocenter parameters of the regional sources (cp. 4.3.3)

The use of the ak135 travel time tables may not be appropriate for events that occurred in an azimuthal direction approximately perpendicular to the trench axes (Fig. 4.1, yellow stars), since travel times of those events might be influenced by the cold sinking incoming lithosphere.

We received a tomographic inversion P-wave velocity model [*Dinc-Akdogan et al.*, 2007] for the study-area (Fig. 4.10, profile Z-Z') and solved the forward problem for the mentioned events by embedding the model volume into the velocity model.

After a total of eight iterations of the tomographic inversion scheme a further reduction of the RMS was not observed. The final solution model reduces the all-over RMS from 205ms to 121ms.

Table 4.2: Final P-wave 1D velocity model.

Layer[a] no.	Depth [km]	V_p [km/s]
0	0.0	1.56
1	0.2	2.10
2	0.4	3.50
3	1.0	4.12
4	3.0	5.26
5	5.0	7.18
6	5.7	7.44
7	7.0	7.58
8	9.0	7.73
9	10.0	7.89
10	12.0	7.97
11	13.5	8.13
12	16.0	8.22
13	20.0	8.27
14	25.0	8.31
15	30.0	8.33
16	35.0	8.37
17	40.0	8.40

[a] Layer 0-1 represent the sediment and are results from drill experiments [*Kimura et al.*, 1997] at the outer rise, approximately 250 km south-eastern from the ORN. It can be assumed that the values are also valid in the study area. The crustal structure (Layer 2-6) is based upon active seismic tomography [*Ivandic et al.*, 2006] and the mantle velocities (Layer 7-17) are results of the inversion, whereas Layer 15-17 are assumed mantle velocities, since, as mentioned, these depths cannot be resolved.

Combination of active and passive sources

The 3D-tomographic procedure combines travel time picks from airgun shots, local seismicity and regional earthquakes in a single inversion. The advantage of this approach is illustrated in Fig. 4.8:

- **Wide-angle and refraction data** have two major advantages. First of all, the locations of airgun blasts are perfectly known. Thus, the inversion problem reduces from a coupled hypocenter-velocity to a simple velocity problem. Secondly, the high number of air gun shots leads to a good ray coverage and hence resolution. However, airgun blasts are in general not powerful enough to record clear mantle-phases in great distances, which leads in the present case to an adequate resolution in the upper 3-5 km of the mantle only (Fig. 4.8a).

- In contrast, **Local sources**, make it possible to resolve greater depths (Fig. 4.8b), but in the present case their number is comparable small and hence ray coverage lacks density. Further, the coupled hypocenter-velocity problem leads to larger RMS.

- Rays emitted from **regional or teleseismic sources** travel great distances and therefore travel the crust and upper mantle with steep angles (Fig. 4.8c). Thus, it is possible to resolve almost the entire lithosphere. A disadvantage is that the use of such rays in tomographic inversions requires accurate *a priori* source locations. A further insight into this is given in the subsequent section.

An inversion of a combined data set of all different sources unites the advantages and minimizes the disadvantages.

Robustness of synthetic arrival times

Meanwhile the hypocenter parameters of local sources are changed during the 3D-tomography inversion process, regional sources remain at their original locations. FMTOMO deals with regional and teleseismic sources by using relative arrival times, which depend on the hypocenter of the source and the used velocity model, but are not as sensible towards changes of these parameters as absolute arrival times. E.g. a change of the hypocenter location changes the ray parameter for a particular station, but the remaining amount of the ray parameter of two nearby stations may not change significantly, if the distance between those two stations is small compared to the distance to the source or if the source is comparable deep.

(1) To test the robustness of relative arrival times against changes in the location of the regional sources, we perturbated hypocenter parameters systematically in depth ($\pm 30km$), lat and lon (each with $\pm 0.2°$). We chose such wide perturbation, since we do not know error margins for the hypocenter parameters of the regional sources. We calculated arrival times of the original location for every station relative to one another. For each perturbation we calculated the maximum change of the relative arrival times within the ORN and excluded every event that showed a maximum change larger than $\pm 100ms$. Fig. 4.9 gives examples. The procedure leaves 47 regional events and excludes every source nearer than 2.1°.

(2) To calculate the travel time between regional source and model volume of the inversion, two different velocity models were used. For one set of sources (Fig. 4.1, red and yellow circles) the ak135 travel time tables were sufficient, meanwhile a second set (Fig. 4.1, yellow stars) uses a velocity model (Fig. 4.10) after *Dinc-Akdogan et al.* [2007]. Systematic perturbations of the velocity models caused significant changes of the relative arrival times only for such regional events that are shallower than ~40 km. Those events have been excluded from the data set, which leaves 39 regional events. However, observed travel times for all regional events show slightly late arrivals for stations closer to the trench compared to travel times calculated with the named velocity models. In contrast, an influence of travel times due to the cold, sinking slab would lead to early arrivals for those stations. Hence,

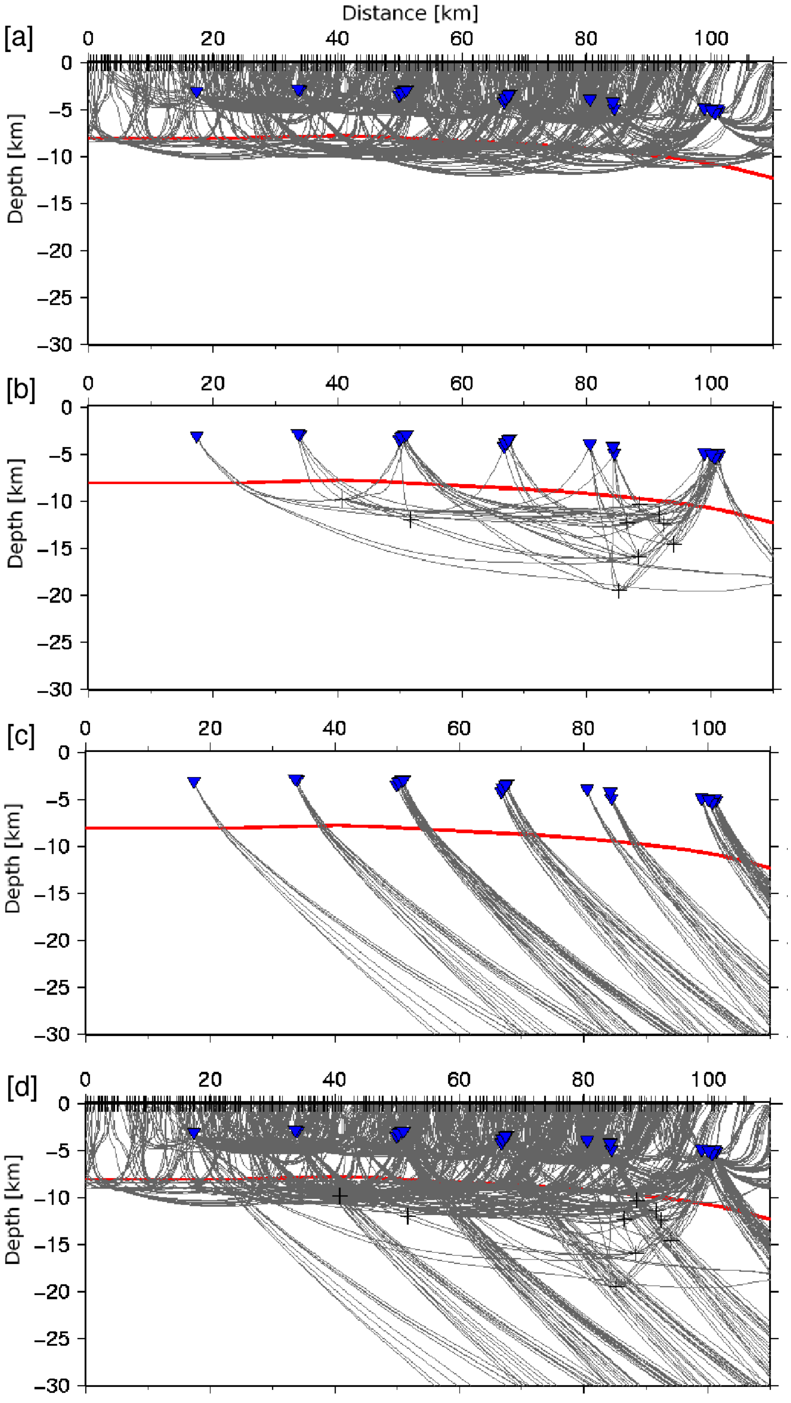

Figure 4.8: *General ray coverage for [a] wide-angle and refraction data (airgun blasts); [b] local earthquakes; [c] regional, respectively teleseismic sources and [d] combination of all sources*

the used P-wave velocity models seem to reflect the complex nature of a subduction zone.

Resolution Test

Synthetic checkerboard tests were used (1) to investigate solution non-uniqueness, which arises from the under-determined nature of the inverse problem and (2) to determine areas of sufficient resolution within the model volume. Checkerboard resolution tests were based on the 1D-input model (Fig. 4.11), whereat mantle velocities were perturbed with alternating regions of high and low velocity between ±0.3 km/s (Fig. 4.12a). For both, local and regional sources synthetic travel times through this model volume were calculated by solving the forward problem. In order to simulate the noise content of the observations, Gaussian noise with a standard deviation of 100 ms and 80 ms is added to the regional arrival time residuals and local source travel times respectively. The aim is to recover the checkerboard velocity model from the unperturbed input model.

Eight iterations of the tomographic inversion scheme were needed to obtain a solution model, which satisfies the synthetic dataset to the level of the imposed Gaussian noise. The quality of the recovered checkerboard pattern for profile A-A' (Fig. 4.12b) is good throughout the slice. This is due to the central position of the profile (Fig. 4.18) and because it has been part of the wide-angle and refraction profile line 03. Other profiles could not achieve such a throughout resolution and are therefore not presented.

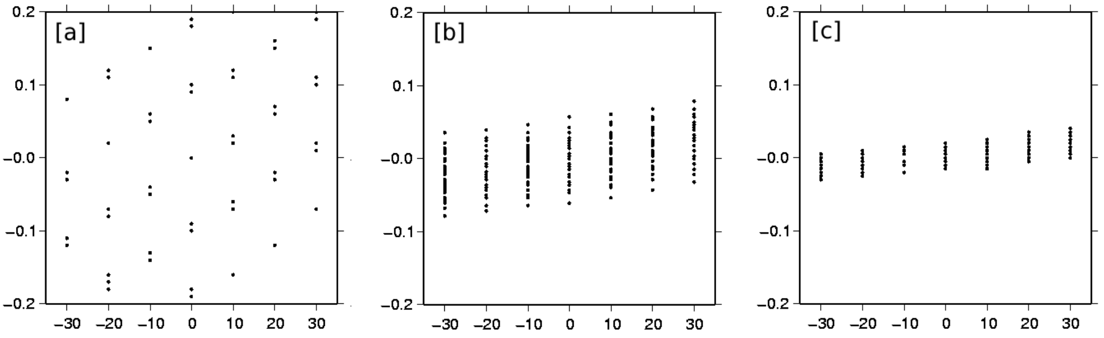

Figure 4.9: *Results of the perturbation test for 3 events. The ordinate gives the maximum change of the arrival time in seconds and the abscissae gives the perturbation of the depths. The different values for one depth result from the perturbation of lat, lon. [a] Perturbation test of a source with a focal depth of 50 km and a (distance 1.29°; backazimuth 48.54° with respect to station obs31). The maximum change is* $> \pm 200 ms$. *[b] Perturbation test of a source with a focal depth of 147 km and a (distance 2.22°; backazimuth 53.03° with respect to station obs31). The maximum change is* $< \pm 100 ms$ *[c] Perturbation test of a source with a focal depth of 91 km and a (distance 6.64°; backazimuth 101.20° with respect to station obs31). The maximum change is* $< \pm 35 ms$.

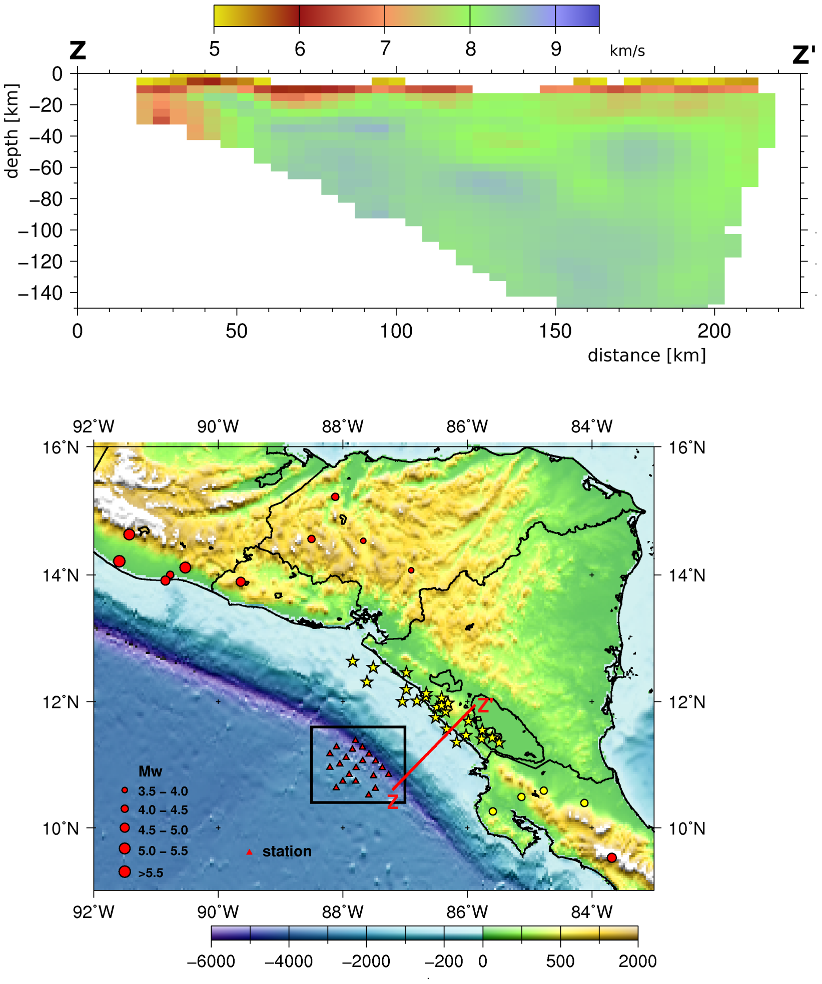

Figure 4.10: *P-wave velocity model after Dinc-Akdogan et al. [2007] used for regional events whose travel times might be influenced by the slab.*

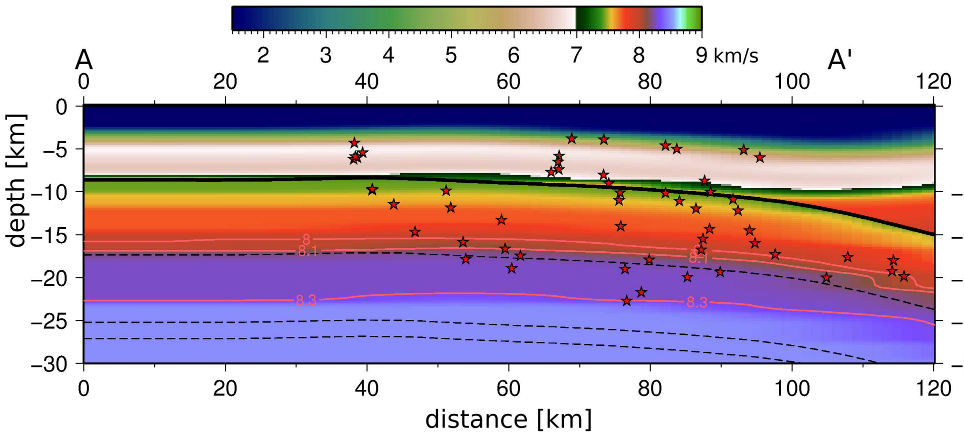

Figure 4.11: *Slice through the input model for the 3D tomography procedure. The model was obtained by combining multibeam bathymetry [Ranero et al., 2003] with the P-wave minimum 1D-velocity model (Table 4.2)*

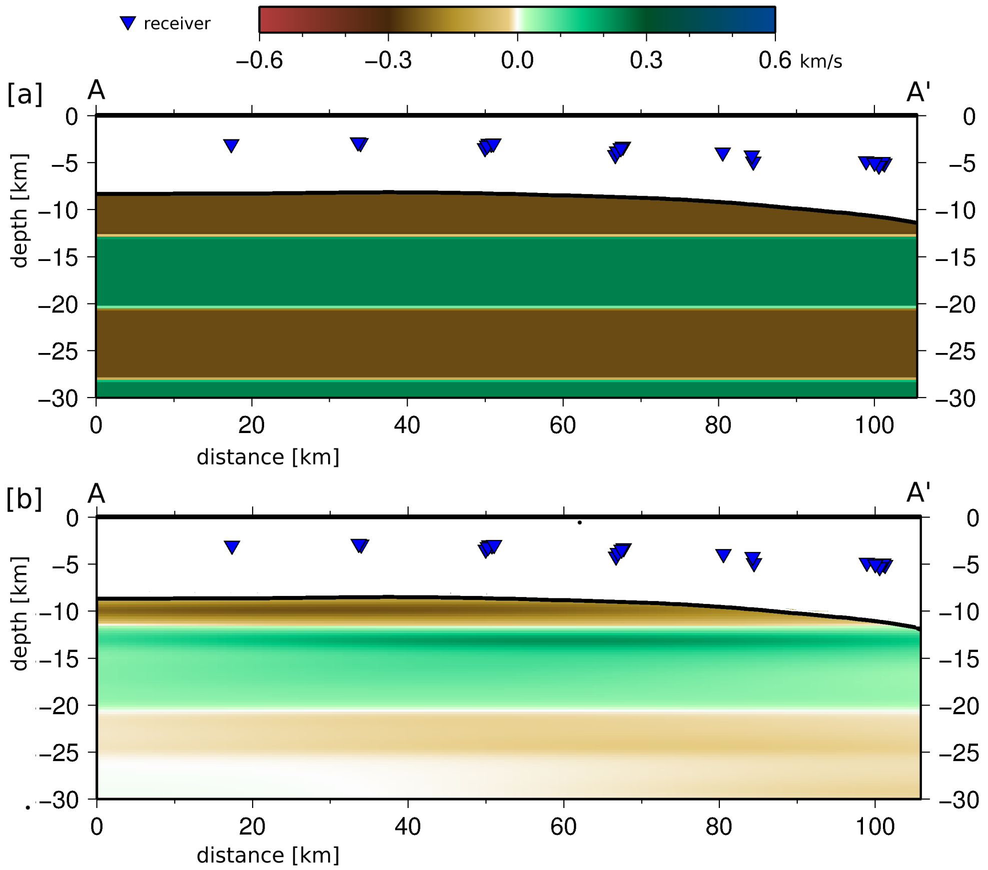

Figure 4.12: *Results of the synthetic checkerboard test used to examine solution robustness. (a) Synthetic model for profile A-A'. (b) recovered model after 8 iterations.*

4.4 Waveform Forward Modelling

A seismic source can be described as a sequence of point sources on a planar fault. Both, the number of point sources that are needed to reflect the rupture process and the dimension of the planar fault increase with the earthquakes magnitude, but the assumption of only one point source is sufficient to determine overall fault mechanism and centroid depth of the entire fault motion [*Yamanaka and Kikuchi*, 2003]. Since focal depth and mechanism are the parameters of interest for this study, we described the rupture process of each considered event as a single point source, which in turn can be described as a moment tensor.

In general a moment tensor has 6 independent elements, whereat commonly the following are used:

$$\mathbf{M}_1 = \begin{bmatrix} 0 & 1 & 0 \\ 1 & 0 & 0 \\ 0 & 0 & 0 \end{bmatrix}; \mathbf{M}_2 = \begin{bmatrix} 1 & 0 & 0 \\ 0 & -1 & 0 \\ 0 & 0 & 0 \end{bmatrix}; \mathbf{M}_3 = \begin{bmatrix} 0 & 0 & 0 \\ 0 & 0 & 1 \\ 0 & 1 & 0 \end{bmatrix}$$

$$\mathbf{M}_4 = \begin{bmatrix} 0 & 0 & 1 \\ 0 & 0 & 0 \\ 1 & 0 & 0 \end{bmatrix}; \mathbf{M}_5 = \begin{bmatrix} -1 & 0 & 0 \\ 0 & 0 & 0 \\ 0 & 0 & 1 \end{bmatrix}; \mathbf{M}_6 = \begin{bmatrix} 1 & 0 & 0 \\ 0 & 1 & 0 \\ 0 & 0 & 1 \end{bmatrix}$$

Any seismic source [**M**] can be written as linear combination of these elementary moment tensors:

$$[\mathbf{M}] = \sum_{n=1}^{6} a_n M_n \tag{4.1}$$

where a_n is the coefficient due to the nth basic moment tensor.

Now, the elements of a moment tensor of a seismic source on a fault plane defined by strike (ϕ) and dip (δ) of the fault surface and the direction of the slip vector, the rake angle (λ), can be written as:

$$\begin{aligned} M_{11} &= -M_0(sin\delta\, cos\lambda\, sin2\phi + sin2\phi\, sin\lambda\, sin^2\phi) \\ M_{12} &= +M_0(sin\delta\, cos\lambda\, cos2\phi + 0.5 sin2\phi\, sin\lambda\, sin2\phi) \\ M_{13} &= -M_0(cos\delta\, cos\lambda\, cos2\phi + cos2\phi\, sin\lambda\, sin\phi) \\ M_{22} &= +M_0(sin\delta\, cos\lambda\, sin2\phi - sin2\phi\, sin\lambda\, cos^2\phi) \\ M_{23} &= -M_0(cos\delta\, cos\lambda\, sin\phi + cos2\phi\, sin\lambda\, cos\phi) \\ M_{33} &= +M_0\, sin2\delta\, sin\lambda \end{aligned} \tag{4.2}$$

where M_0 is the seismic moment [e.g. *Aki and Richards*, 1980].

Then the coefficients a_n are

$$a_1 = M_{12}\,;\ a_2 = \frac{1}{2}(M_{11} - M_{22})\,;\ a_3 = M_{23}\,;$$

$$a_4 = M_{13}\,;\; a_5 = \frac{1}{2}(-M_{11} + M_{33})\,;\; a_6 = \frac{1}{3}(M_{11} + M_{22} + M_{33})$$

Let $\omega_{in}(t, p)$ denote the synthetic seismogram (Green's function) at station i due to the nth elementary moment tensor, where t is the time and p is a parameter that represents both, the onset time τ and the location of the point source. Next, the synthetic waveform $y_i(t, p)$ at station i can be obtained through

$$y_i(t, p) = \sum_{n=1}^{6} a_n \omega_{in}(t, p) \tag{4.3}$$

and compared to the observed one. A grid search over all possible values of ϕ, δ and λ determines the best-fit focal mechanism.

For the calculation of the Green's function we used the computer routine QSEIS [*Wang*, 1999], which is based on the reflectivity method [*Fuchs*, 1968; *Fuchs and Müller*, 1971; *Müller*, 1985; *Ungerer*, 1990]. The advantage of this code is that it can handle multiples very well and calculates next to the common displacement and velocity seismograms also volume changes for hydrophones. The program allows for different 1D velocity structures for both source and receiver and interpolates between them. We used the results for the P-wave minimum 1D-velocity model as input.

We performed a grid search over all strike angles with a step size of 10°, over all dip angles with a step size of 5° and over all rake angles with a step size of 10°. Once a best-fit mechanism was found we performed a second grid search with a step size of 1° for all angles starting from -20° and going to +20° relative to the best-fit solution.

A stable and reliable focal mechanism solution requires data of much higher quality than for the calculation of a minimum 1D-velocity model. In our experience just events with at least 10 P-wave observations and a gap in the azimuthal distribution of stations of <90° can be used.

Only 17 events from the data set fulfil these high standards, but most of them occurred in the crust, which is of secondary importance for this study. For 5 events in the mantle we could determine focal mechanisms (Fig. 4.18). For the calculation of these focal mechanisms we used only hydrophone data. The reason is that every ocean bottom seismometer was also equipped with a hydrophone, which data usually showed a better signal-noise-ratio than the vertical seismometer component. S-wave data could not be used due to the described problems (a rotation of the vertical components is not possible).

Usually, waveform forward modelling and moment tensor inversion allow the calculation of moment magnitudes by a fitting of the amplitudes. Therefore, the absolute amplitudes need to be known, which is not the case in the present data set, since different preamplifiers were in use for which the gain is not known.

The moment magnitude is not needed in this study, hence we norm the amplitudes of both the observed data and the synthetic one to the highest value within the considered time window. We chose a time window of 0.1 s before the first arrival to 0.5 s to 0.8 s after. The window needs to be this short since the following multiples and reflections are almost impossible to calculate and hence will introduce instabilities.

Fig. 4.13, Fig. 4.14 and Fig. 4.16 show waveform fits between observed and best-fit synthetic data for up-going, tensional mechanisms and Fig. 4.15 and Fig. 4.17 for down-going, compressional ones. The RMS residuals were between 0.4 and 0.55, which is acceptable low for data of such high frequencies. One can see that a residual is often caused rather by a difference in frequency (e.g. compare Fig. 4.13, station obh17 and obs29) than a misfit of polarities, which is more likely an effect of assumptions for the calculation of Green's functions e.g. geometry and duration of the source time function (a trapezoid function with cosines flanks and a duration of 100 ms has been used) and layering of the velocity model, than an effect of a wrongly calculated focal mechanism.

The best solutions are shown in Fig. 4.13c - 4.17c. Plotted are all solutions until the residual increased 10%. The waveform observed at a receiver is strongly influenced by the depth of the source. We carried out several grid searches using Green's functions for various source depths.

Fig. 3.4 shows the results of these calculations. The lowest residual determines the focal depth. Differences between focal depths obtained with this method and obtained from the travel time hypocenter location are $\leq$2.2km (Table 4.3).

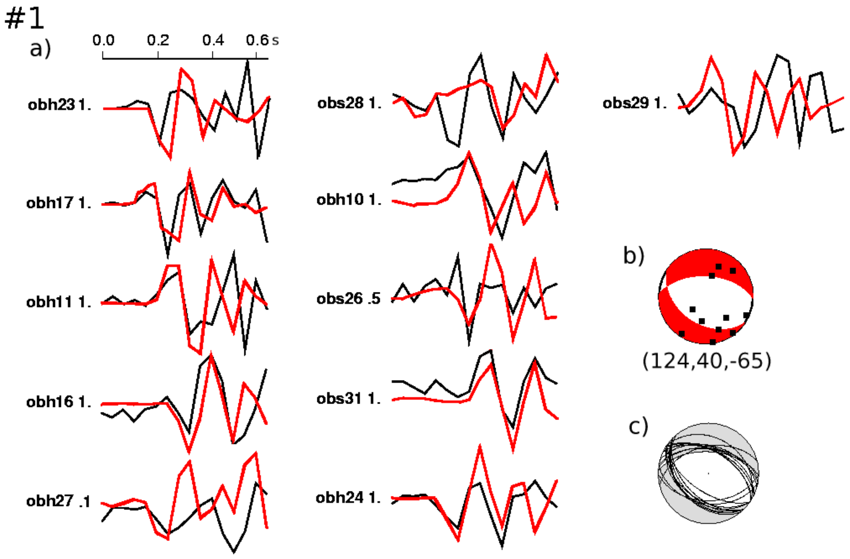

Figure 4.13: *Results of the forward modelling procedure for event #1. (a) Comparison between observed (black lines) and best-fit synthetic waveforms (red lines). The number behind the station name gives the weighting. (b) Best-fit focal mechanism and station distribution (black dots). The numbers below the mechanism diagram give the strike, dip and rake angles in degree. (c) Best solutions.*

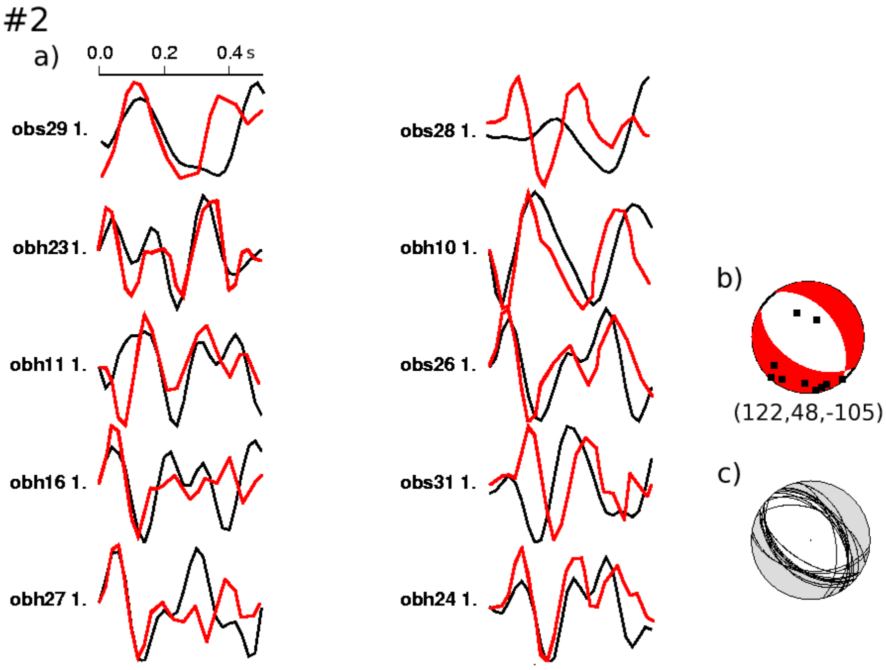

Figure 4.14: *Results of the forward modelling procedure for event #2. (a) Comparison between observed (black lines) and best-fit synthetic waveforms (red lines). The number behind the station name gives the weighting. (b) Best-fit focal mechanism and station distribution (black dots). The numbers below the mechanism diagram give the strike, dip and rake angles in degree. (c) Best solutions.*

4.5 Magnitudes

Following the approach of *Tilmann et al.* [2007], we used only hydrophone traces for the calculation of moment magnitudes. We removed the nominal response following *Thölen* [2005]. One problem was that we do not know what kind of preamplifier was used between hydrophone and recorder. However, all different preamplifiers that have been used in the ORN were investigated by *Thölen* [2005] and show a similar behavior for frequencies $\geq$1.5 Hz. Cut-off-frequencies are always below 0.3 Hz. We did not make use of frequencies below 4 Hz, since those were dominated by noise. Hence, for this particular study, the preamplifier does not influence the response function.

Next, the corrected hydrophone trace is multiplied by the sound velocity (1.5 km/s) and the density of water (1000 km/m^3). The resulting trace is identical to the displacement for a vertically incident wave and zero impedance contrast between seafloor and water. Even though these assumptions might not be fulfilled perfectly, they are also not violated too badly, since velocities and densities of the uppermost sediments are comparable to that in water and cause earthquake arrivals to have steep raypaths below the station.

The calculation of moment magnitudes then was done by applying standard method and code of *Ottemöller and Havskov* [2003], which searches for the combi-

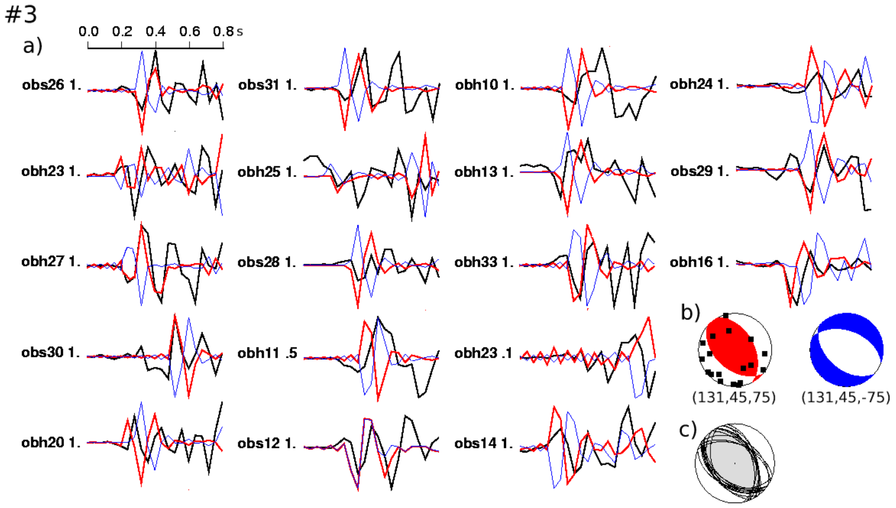

Figure 4.15: *Results of the forward modelling procedure for event #3. (a) Comparison between observed (black lines) and best-fit synthetic waveforms (red lines). The number behind the station name gives the weighting. (b) Best-fit focal mechanism and station distribution (black dots). The numbers below the mechanism diagram give the strike, dip and rake angles in degree. (c) Best solutions.*

nation of seismic moment M_0 and corner frequency f_0 that fits the observed spectra the best. The absolute magnitude was calibrated to one event that was observed by the ORN and land stations of INETER (magnitude determined from land stations was Mw=3.2 and from station of the ORN Mw=2.8±0.1). However, relative magnitudes of local events are more important for this study than absolute ones.

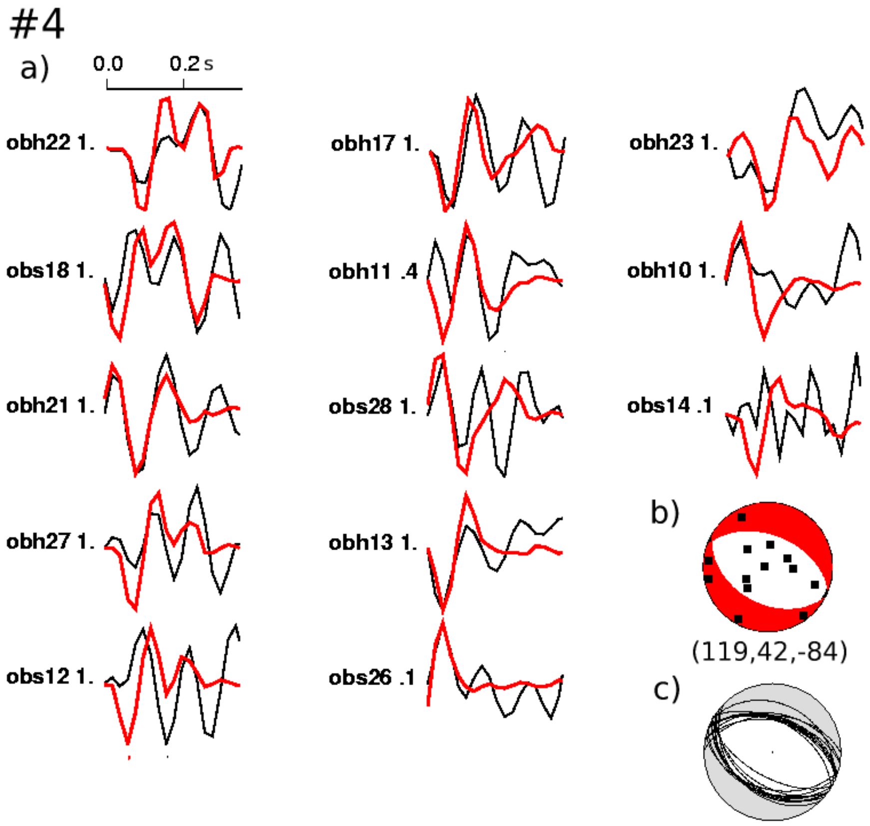

Figure 4.16: *Results of the forward modelling procedure for event #4. (a) Comparison between observed (black lines) and best-fit synthetic waveforms (red lines). The number behind the station name gives the weighting. (b) Best-fit focal mechanism and station distribution (black dots). The numbers below the mechanism diagram give the strike, dip and rake angles in degree. (c) Best solutions.*

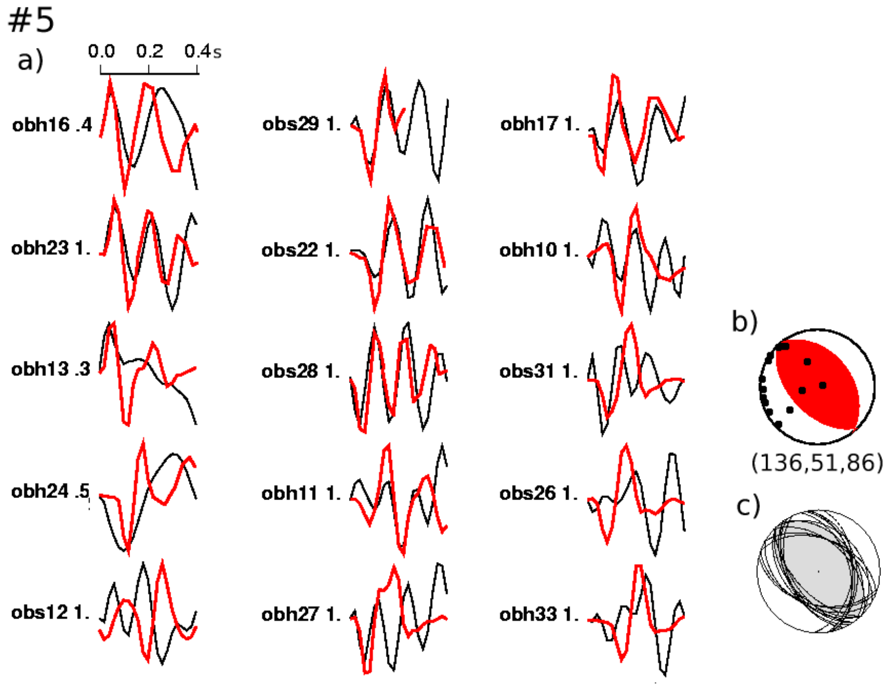

Figure 4.17: *Results of the forward modelling procedure for event #5. (a) Comparison between observed (black lines) and best-fit synthetic waveforms (red lines). The number behind the station name gives the weighting. (b) Best-fit focal mechanism and station distribution (black dots). The numbers below the mechanism diagram give the strike, dip and rake angles in degree. (c) Best solutions.*

4.6 Results and Discussion

The epicentre distribution of local sources (Fig. 4.18) supports constraints from seismic reflection data that imaged faults cutting through the crust 10-15 km into the mantle [*Ranero et al.*, 2003]. Seismic reflection images and focal solutions of large trench-outer rise earthquakes [*Lefeldt & Grevemeyer*, 2007] within the study area suggest that trench-outer rise normal faults dip landwards with an angle of $\sim 40° - 45°$. A projection of all local sources on a cross-section perpendicular to the trench axes shows a good match with faults of these particular dip-angles (Fig. 4.19) and density of earthquakes in the cross section can be related to density of faults. Seismic events were exclusively recorded in areas that show normal faults in the bathymetry (up to 60 km seawards of the trench), where seismicity reaches ~15 km into the mantle. Seismicity increases towards the trench, but the deepest events were recorded within ~20 km distance from the trench axis. Hypocentre parameters for all local sources are very accurately constrained. The final velocity solution model shows a data misfit variance of only 0.018 s^2, which corresponds to a RMS error of 135 ms. Note, that this includes residuals from regional sources, which are slightly higher, since they are not inverted for their hypocentre locations. The RMS error of local sources only is 121 ms.

Large earthquakes, however, might be able to cut deeper into the lithosphere, but such events were not recorded during the period of deployment of the network. Except for one event with a moment magnitude of Mw=3.2, land stations of the Instituto Nicaraguense de Estudios Territoriales (INETER) did not record any event in the outer rise during the time of deployment, suggesting that all recorded earthquakes have general magnitudes beneath this value. Nevertheless, focal and centroid depths as well as dimensions of rupture planes constructed for larger trench-outer rise events within the study area, like the 1994 Mw=5.8 event or the recent 2006 Mw=5.2 event, suggest a similar depth for the penetration of bending-related faults into the lithosphere [*Lefeldt & Grevemeyer*, 2007]. Hence, seismicity in the trench-outer rise may not exceed limits revealed by microearthquakes.

Combination of local and regional events in one tomographic inversion allows for an insight into the lithosphere deeper than bend-faults can possible cut. We show a highly resolved cross-section through the final P-wave velocity model in Fig. 4.10. Location and direction of the cross-section are given in Fig. 4.19. Checkerboard resolution tests (Fig. 4.12) demonstrate the full resolution of the shown tomographic image. One demonstrative feature in profile A-A' is an area of low P-wave mantle velocities, that develops approximately were normal faulting begins to govern the bathymetry and extends down to ~12 km below the Moho close-by the trench axis. P-wave velocities show values between 7.2 km/s and 7.9 km/s, which is 3-11% lower than the typical velocity of mantle peridotite [*Peacock et al.*, 2001; 2003]. Interesting is that the size of the area characterized by reduced velocities seems to increase linear towards the trench, while seismicity does not. Furthermore, several sources lay outside of this velocity anomaly. Average RMS for these sources does not differ from the RMS for the sources within the anomaly which, in turn, does not differ significantly from the RMS for regional events. That gives confidence that the edges of the anomaly are well designed and not rather an artefact of a decreasing resolution with depth.

Mantle velocities near the trench seem to be significantly reduced in the upper 5 km, but then go gradually back to expected values for oceanic lithosphere roughly 10 km deeper. The focal mechanisms for five earthquakes within the mantle derived from waveform forward modelling may provide a possible explanation. All mechanisms show a dip direction (Table 4.3) similar to those derived trench-outer rise faults [*Ranero et al.*, 2003; *Lefeldt & Grevemeyer*, 2007]. However, the three shallowest events show a purely tensional character, while the two deepest ones have compressional mechanisms. Further, relating earthquake location to seismic velocity (Fig. 4.19a) suggests that tensional events are embedded in the area of reduced mantle velocity, while the compressional ones lay beneath or at its edge. This observation does not only support the model of *Chapple and Forsyth* [1979], but rather suggests that the bottom of the area of reduced mantle velocity coincides with the neutral plane between both major stress regimes. However, reduced P-wave mantle velocities might be caused by fluids, but can also be explained by fracture porosity. Work of *Wilkens et al.* [1991] on the relationship between seismic velocity and porosity in basalts has shown that a small increase of $\sim$5% in the effective porosity can decrease seismic velocity by 50%. Thus, bending-related faulting may cause large-aspect ratio cracks in crust and upper mantle and therefore reduced velocities might be caused by a small change in effective porosity alone.

The area of reduced mantle velocity (<8.1-8.3 km/s) in Profile A-A' (Fig. 4.19a) reaches its maximum thickness of $\sim$12 km below Moho in the immediate vicinity of the trench. In contrast, seismicity reaches such depths already $\sim$45 km seawards the trench, where velocity reduction is by far not as distinct. A reduction of seismic velocities due to an increase of porosity is a process that is instantaneous linked to the occurrence of fractures, while a velocity reduction due to serpentinization proceeds slowly, since the diffusion speed of water in unfractured serpentine is only $\sim$1 km Myr$^{-1/2}$ [*Macdonald & Fyfe*, 1985], while the current convergence rate of the Cocos Plate is 80 km Myr^{-1}. Thus, the consistent reduction of P-wave velocities towards the trench, independently from the increase of seismicity militates in favour of serpentinization, but the sudden occurrence of velocity reduction to values of <8.1 km/s were seismicity occurs first (as it can be observed in Fig. 4.19, $\sim$60 km seawards of the trench) argues for fracture porosity.

A partly serpentinized upper mantle would not only lead to reduced seismic velocities, but also would change the rheological behaviour of the lithosphere, since a serpentine content of 10%-15% or less in peridotite already leads to physical conditions of pure serpentinites [*Escartin et al.*, 2001] with a "weak" and nondilatant rheology. Thereby, the strength is reduced from $\sim$1250MPa (peridotite) to $\sim$450MPa at Pc=200MPa.

We determined moment magnitudes from the source spectra [*Ottemöller & Havskov*, 2003] for 50 local events (Fig. 4.20). Magnitudes decrease towards the trench with exception of those events that were found to be compressional and deep. Accompanied is this decrease by an increase of the number of earthquakes per unit length towards the trench. This phenomenon can be best explained by a weak lithosphere, where comparable small stresses can already cause a rupture. Hence, the lithosphere ruptures lighter and under release of less energy, but therefore more frequently.

Further, serpentinization is related to a volume increase of ∼40%. In consequence, fractures should be sealed and fracture porosity should decrease towards the trench. For those reasons we suggest that the vast majority of the area of reduced mantle velocity near the trench axis is caused by serpentinization. We calculate the amount of water in the mantle by using the approximation of *Carlson and Miller* [2003], which relates the degree of serpentinization and water content of partially serpentinized peridotite to its seismic P-wave velocity. Therefore we integrate over the differences in the mantle P-wave velocity between and observed values (Fig. 4.19). The average velocity of the uppermost 12 km of the mantle is 7.76 km/s, which is ∼4-6% lower than expected values for dry oceanic lithosphere and corresponds to 1.24 - 1.86 wt% stored water or an increase in serpentine content of ∼10-15% and is equivalent to a fluid flux of 1.2 - 1.75 $gm^{-1}s^{-1}$ (cp sec. 4.7.1).

Our assessment nearly coincide with the lower limit evaluated in other studies for the Central American subduction zone [*Ranero et al.*, 2003]; thus, indicates that previous estimates may have roughly been 5 to 10 times too high.

Table 4.3: Results of the waveform forward modelling.

No.[a]		focal solution[b]		Depth[c]
	strike, *deg*	dip, *deg*	rake, *deg*	(km)
1	124	40	-65	6.1
	273	54	-109	
2	122	48	-105	8.3
	323	44	-72	
3	131	45	75	16.9
	332	47	104	
4	119	42	-84	9.9
	290	48	-95	
5	136	51	86	14.8
	321	39	96	

[a] The numbering is after Fig. 4.18. [b] For each event, two solutions were obtained that fit the observed waveforms equally well, whereat one is the fault and the other one the auxiliary plane. A distinction between both is impossible from waveform modelling alone. Seismic images [*Ranero et al.*, 2003] suggest that bending-related faults dip landwards, which is only fulfilled by the mechanisms given in the first row of every event. [c] Given is the depth beneath seafloor inferred from the tomographic inversion process

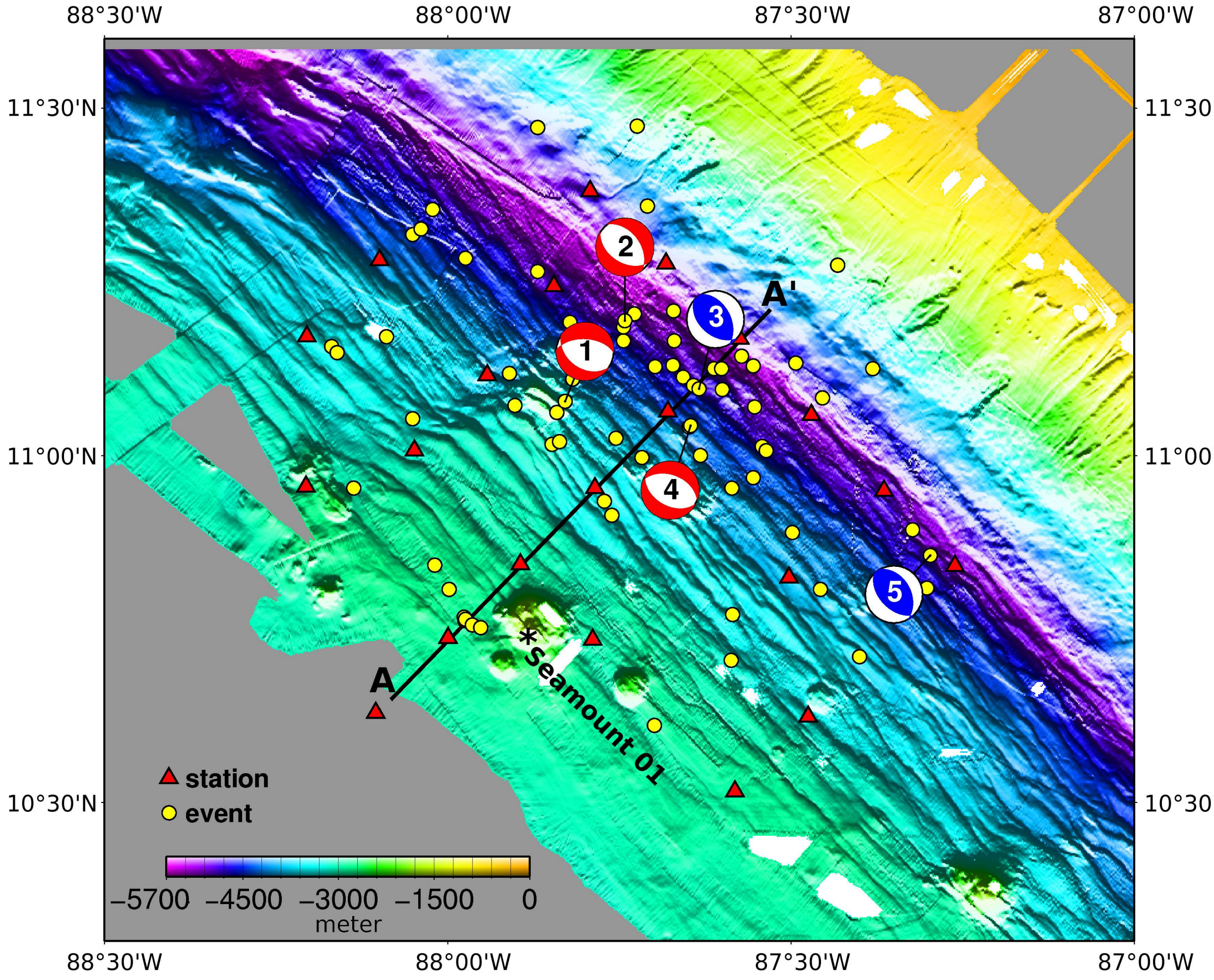

Figure 4.18: *Final epicentre distribution of all local sources. Hypocenter error ellipses, which semi-major axes are throughout <1km are not plotted, in order to maintain straightforwardness. Epicentres seem to fit the multibeam bathymetry [Ranero et al., 2003]. Most seismicity occurs within ∼30 km seawards the trench. Another spot of increased seismicity is located nearby seamount 01. Therefore it can be hypothesized that seamounts support fluid migration. Focal mechanisms for five events within the mantle are plotted (numbering is arbitrarily). The black line shows the location and direction of the cross-section shown in Fig. 4.19.*

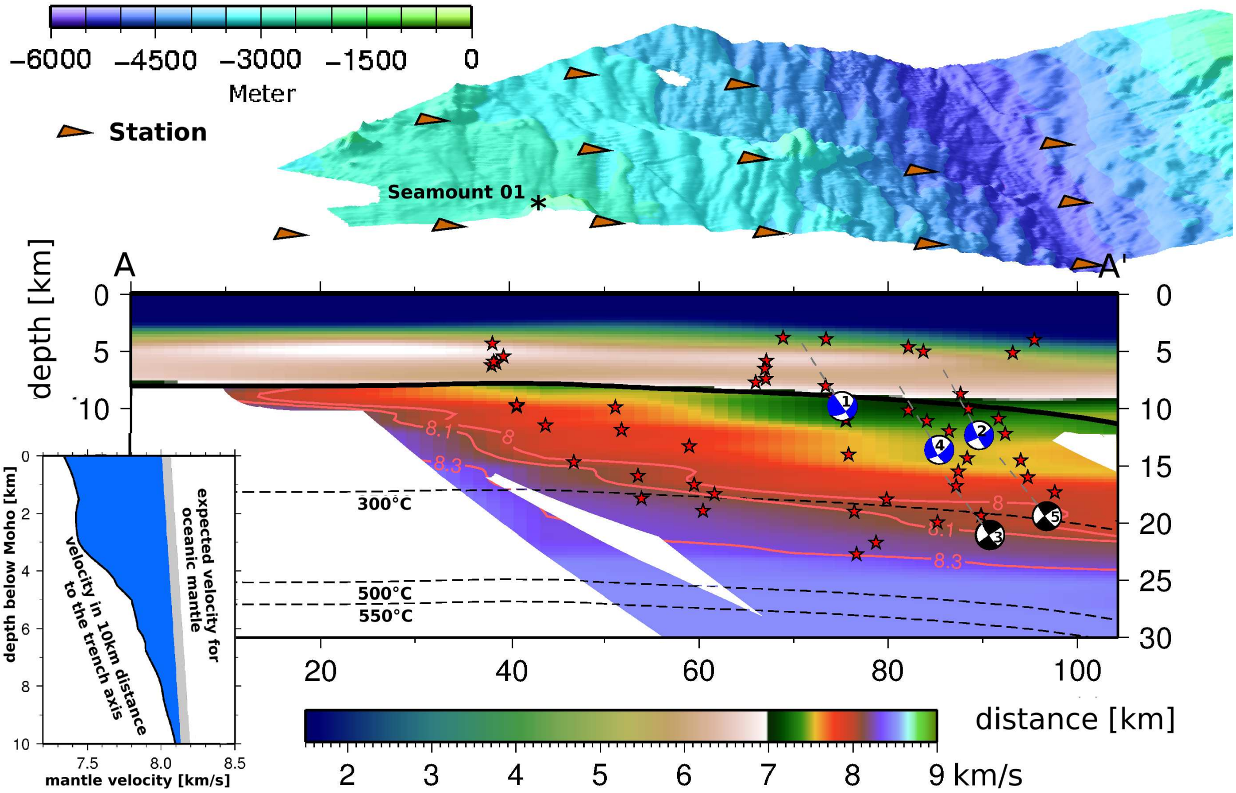

Figure 4.19: *Cross-section through the final P-wave velocity model volume along profile A-A'. The central position of the profile in the ORN and the existence of wide-angle and refraction data along the profile leads to a high resolution and remarkable small RMS. Areas of low resolution are clipped in the image. All earthquakes (red stars) and all focal mechanisms shown in Fig. 4.18 are projected on the cross-section. Isovelocity lines of 8 ; 8.1 and 8.3 km/s are plotted to underline the evolutionary trend of the low velocity anomaly, which starts to become a crucial feature beneath seamount 01, where seismicity occurs for the first time. A comparison between expected P-wave velocities for dry, oceanic lithosphere and actual velocities at ~10km seawards of the trench (at 90 km position in the profile A-A') is shown at the bottom left corner. Isotherms have been calculated using the code of McKenzie et al. [2005]. Multichannel bathymetry [Ranero et al., 2003], which is plotted on top of the tomographic image, shows a high density of bend-faults for distances >60 km from point A. Here, also seismicity shows the largest density. Dip angles of the five focal mechanisms are between 40° and 51° (Table 4.3) and nearby events seem to arrange according to these particular dip angles (grey dashed extensions).*

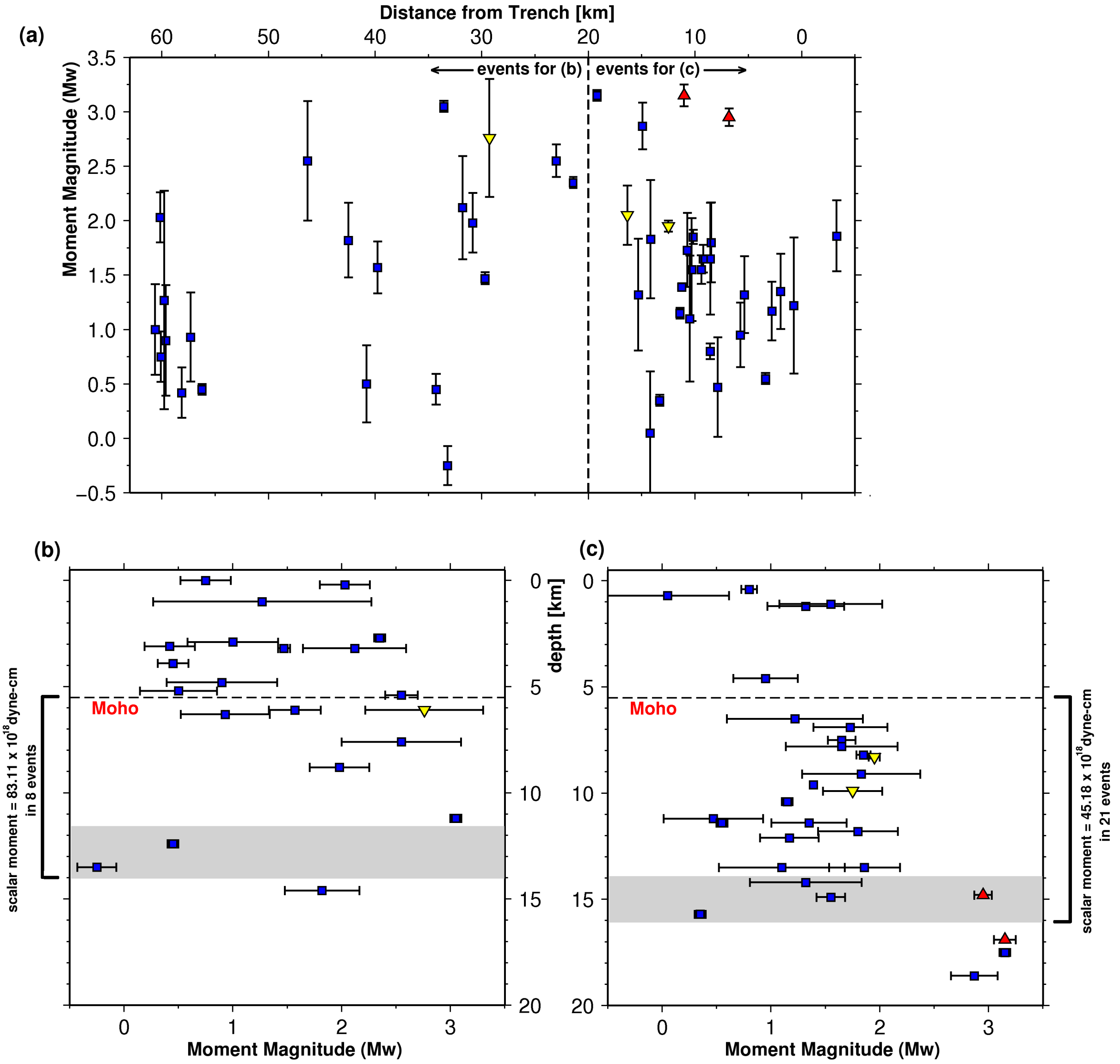

Figure 4.20: *Moment magnitudes for 50 local events. Determination of moment magnitudes is based on source spectra, whereat only hydrophone traces were used following the approach of Tilmann et al. [2007], which applies method and code of Ottemöller and Havskov [2003] on the same type of instruments as used in the ORN. The red triangles show the magnitudes of the events with compressional focal mechanism (#3 and #5), yellow triangles show those of the three tensional events (#1, #2 and #4). The moment was calculated for every particular station. Shown magnitudes are averages of those results. Error bars give the root mean square deviation. Land stations of INETER recorded one event and a moment magnitude of 3.2 was determined. We calibrated all events after this one, which also appears to have the largest magnitude. However, a calibration with only one reference event might introduce large uncertainties, but in this study relative magnitudes are of greater importance than absolute ones. Moment magnitudes against distance from the trench are shown in (a), meanwhile (b) shows moment magnitudes against focal depth for all events further than 20 km from the trench axis and (c) for all events in a 20 km range from the trench axis.*

4.6.1 Bending of a Thin Plate

In a former study [*Lefeldt and Grevemeyer*, 2008] we investigated several large (Mw$\geq$5.5) outer rise normal fault events nearby the Middle America Trench. Existence of such large earthquakes in this area seems to conflict with our hypothesis that only normal fault events of small magnitude can occur in the weak serpentinized upper mantle close-by the trench.

Following *Conner et al.* (2003), the stress distribution $\sigma_{xx}(z)$ over depth z of a plate in bending with the thickness $2h$ is

$$\sigma_{xx}(z) = \frac{2\mu}{(1-\nu)}\kappa z \tag{4.4}$$

in case of symmetric bending and

$$\sigma_{xx}(z) = \frac{2\mu}{(1-\nu)}\kappa \left[h\left(1-\sqrt{\frac{\kappa_z}{\kappa}}\right)^2 + z \right] \tag{4.5}$$

in case of non-symmetric bending, where μ is the elastic shear modulus, ν is the Poisson's ratio of the plate, κ the curvature and κ_z the yield curvature given by

$$\kappa_z = \frac{(1-\nu)}{2\mu}\frac{\sigma_z}{h} \tag{4.6}$$

with the yield strain σ_z.

Fig. 4.21 illustrates these equations. If a plate is bended symmetricly, the neutral plane, i.e. the depth with $\sigma_{xx} = 0$ is in the exact geometrical center of the plate. Beneath this depth, compressional stress increases until the yield strain is reached and thrust faults are created, above, the same applies for tensional stress and hence normal fault earthquakes. In non-symmetric bending, yielding occurs only in tension and not in compression. The location of the neutral plane is shifted.

Offshore Nicaragua, the incoming oceanic plate has an age of ~24Ma [*Barckhausen et al.*, 2001], which gives a temperature distribution shown in Fig. 4.21c. Earthquakes occur only above the 650°C isotherm, where the lithosphere is brittle enough [*McKenzie et al.*, 2005], which implies that the bending of an oceanic plate is non-symmetric. In such a model, compressional earthquakes are not possible, in contradiction with world-wide observations [e.g. *Chapple and Forsyth*, 1979].

However, additional stress is applied (1) by the coupling of the oceanic and the continental plate and (2) by the cold sinking slab. These forces apply parallel to the tangent of the curvature κ and therefore approximately parallel to the bending stress and thus can be introduced as a constant ς in eq. 4.7

$$\sigma_{xx}(z) = \frac{2\mu}{(1-\nu)}\kappa \left[h\left(1-\sqrt{\frac{\kappa_z}{\kappa}}\right)^2 + z \right] + \varsigma \ , \tag{4.7}$$

whereat ς can be described as $\varsigma = \varsigma_{sp} - \varsigma_{pc}$ with the slab-pull stress ς_{sp} and the plate-coupling stress ς_{pc}. This implies that compressional earthquakes are only possible if $\varsigma_{sp} < \varsigma_{pc}$.

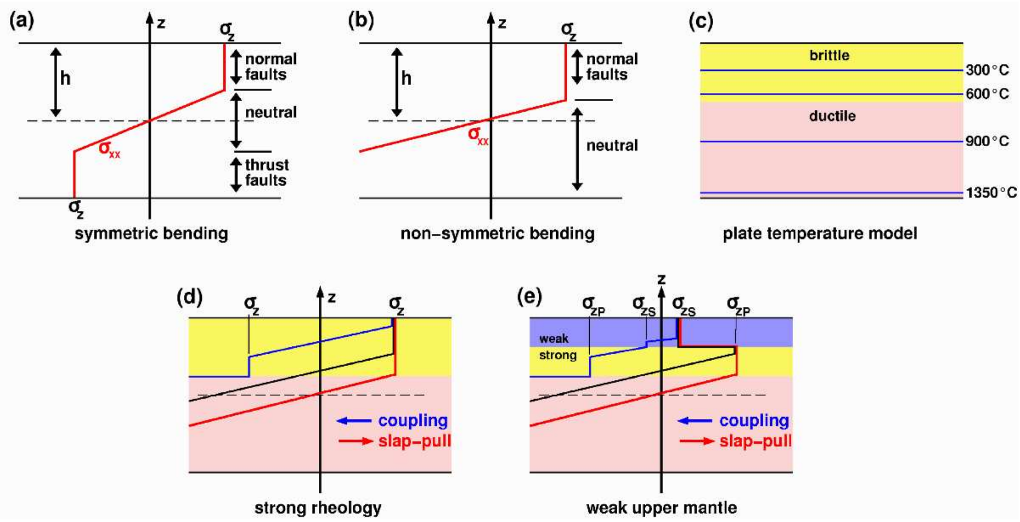

Figure 4.21: *Stress distribution in (a) symmetric bending and in (b) non-symmetric bending following Conner et al. [2003]. Temperature distribution of a 24Ma oceanic plate after McKenzie [2005]*

All of these considerations were done under the assumption that μ (and hence the related seismic S-wave velocity V_S), ν and σ_z are constant with depth. This is not necessarily the case, since these values depend on temperature, density, pressure, etc., but neither it will be violated too badly for the solid and brittle upper mantle nor is the particular function of the stress over depth of importance for these considerations. However, the picture changes drastically, if the upper mantle is serpentinized.

If peridotite is serpentinized, its strength changes negligible until a content of ∼10% serpentinite is reached and the rheology switches abruptly to the one of pure serpentinite associated with a drop in strength of ∼65% [*Escartin et al.*, 2001]. Such a condition is illustrated in Fig. 4.21e. The brittle upper mantle is divided into a weak section with >10% serpentinite and a reduced yield strain σ_{ZS} on top and a strong section beneath with the rheology of peridotite and its yield strain σ_{ZP}. If the both plates are coupled ($\varsigma_{sp} < \varsigma_{pc}$), several small tensional earthquakes will occur in the "weak" area whenever the reduced yield strain σ_{ZS} is reached, meanwhile compressional earthquakes of larger magnitude may occur in the "strong" zone, provided that ς_{pc} is large enough. On the other hand, in the state of a slab-pull ($\varsigma_{sp} > \varsigma_{pc}$), large tensional earthquakes are possible in the combined weak-strong brittle zone.

Thus, these conclusions allow to combine results of this study with our former work [*Lefeldt and Grevemeyer*, 2008] and extend existing models of *Chapple and*

Forsyth [1979] and *Christensen and Ruff* [1988].

4.7 Appendix

4.7.1 Calculation of water flux

The calculation of the total water flux fl $[gm^{-1}s^{-1}]$ into the subduction zone (section 4.6) was done by using the equation

$$fl = [(1-\lambda)\rho_P + \lambda\rho_S]\, z\, \omega\, v_{sub} \tag{4.8}$$

with the density of peridotite $\rho_P \approx 3.2gcm^{-3}$; the density of serpentinite $\rho_S \approx 2.5gcm^{-3}$ [e.g. *Carlson and Miller*, 2003]; the serpentine content λ ≈10-15%; the depth of serpentinized mantle $z = 12km$; the amount of stored water $\omega = 1.24-1.86$ wt% and the subduction velocity of $v_{sub} \approx 8cma^{-1}$

4.7.2 Additional profiles

Profile A-A' in Fig. 4.19 shows the most significant and best resolved part of the 3D-model volume. However, other parts of the model volume can provide further information. Fig. 4.22 gives the location of two additional cross-sections, which are shown in Fig. 4.26 and 4.29. Checkerboard resolution tests (Fig. 4.24 and 4.27) suggest a sufficient resolution for layers deeper than $\sim 2-3$ km beneath Moho. Areas of low resolution are clipped in the cross-sections (Note that some areas are clipped even though they seem to be resolved according to the resolution tests. However, during the inversion process, the velocity changes only in grid cells with ray coverage, but is inter- and extrapolated respectively for bordering cells without coverage. This is done for the case that the raypath changes in the next iteration to an adjoining grid cell. Thus, some areas seem to be resolved in the checkerboard test but do not show ray coverage (Fig. 4.23, 4.25, 4.28) in the final model. Further, in Fig. 4.23, 4.25, 4.28 all raypaths are plotted that cross the profile and therefore influence the inversion. Thus, rays are projected on the profile. However, this means that some areas in the profiles shown in Fig. 4.19, 4.26 and 4.29 might lack resolution even were ray-coverage seem to be given and are therefore clipped.).

Profile B-B' runs parallel to the deep sea trench. The depths of the iso-velocity lines do not change significantly throughout the profile, except where profile A-A' crosses, which is rather an artefact of higher resolution in this area due to the use of active seismic travel time picks. Thus, the final model volume suggests a high degree of isotropy in seismic velocities.

Profile C-C' is located perpendicular to the deep sea trench (parallel to profile A-A'). P-wave mantle velocities show equivalent values and trend to profile A-A'.

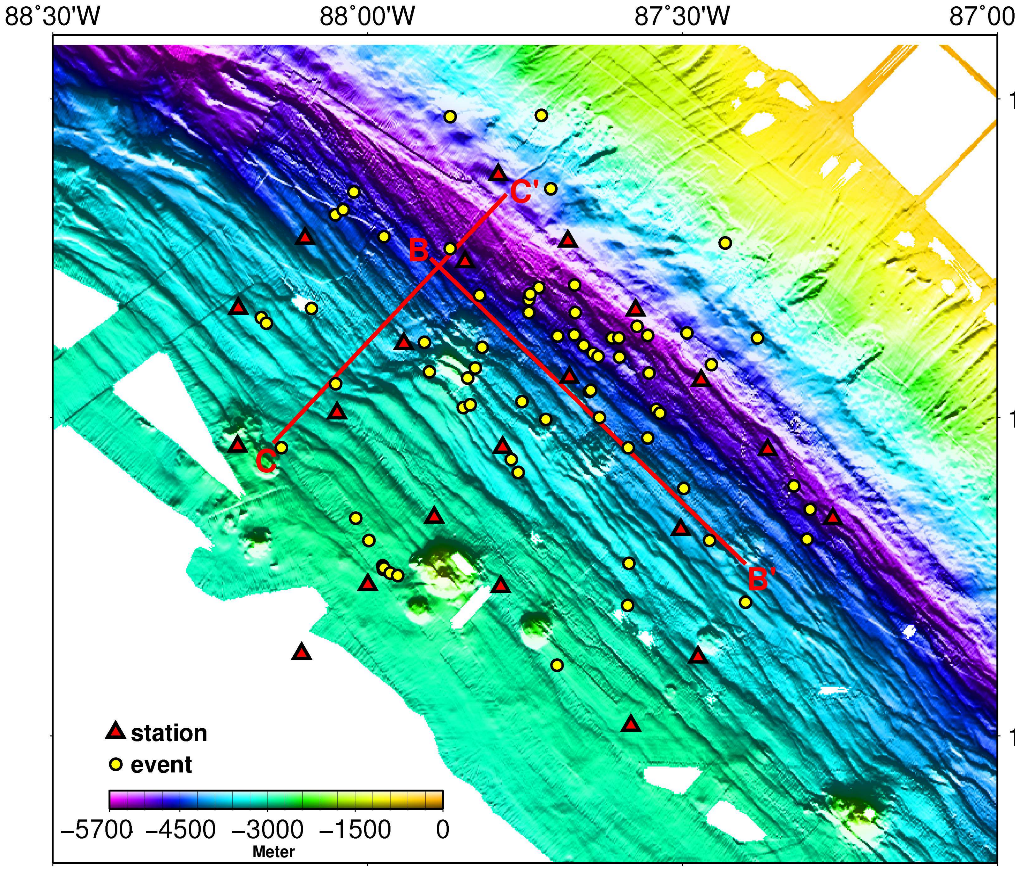

Figure 4.22: *Locations of the cross-sections shown in Fig. 4.26 and 4.29.*

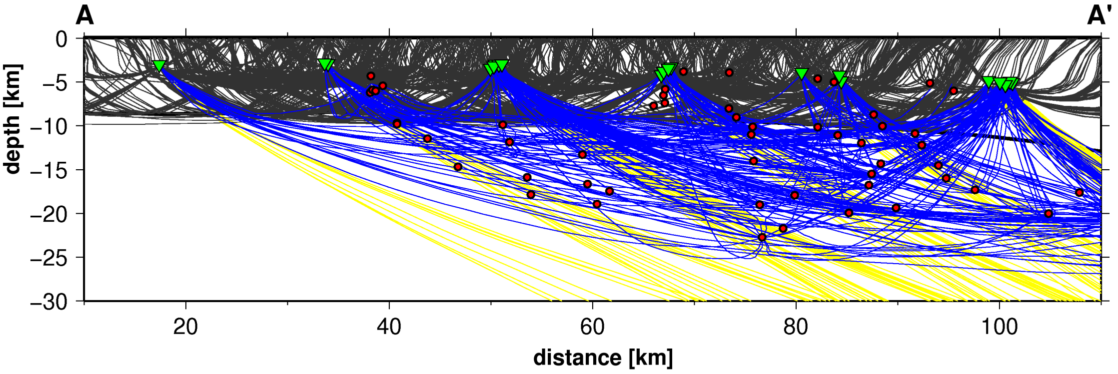

Figure 4.23: *Ray coverage for profile A-A'. Black raypaths are from airgun blasts, blue from local sources and yellow from regional events. Green triangles denote the receivers and red filled circles the local sources.*

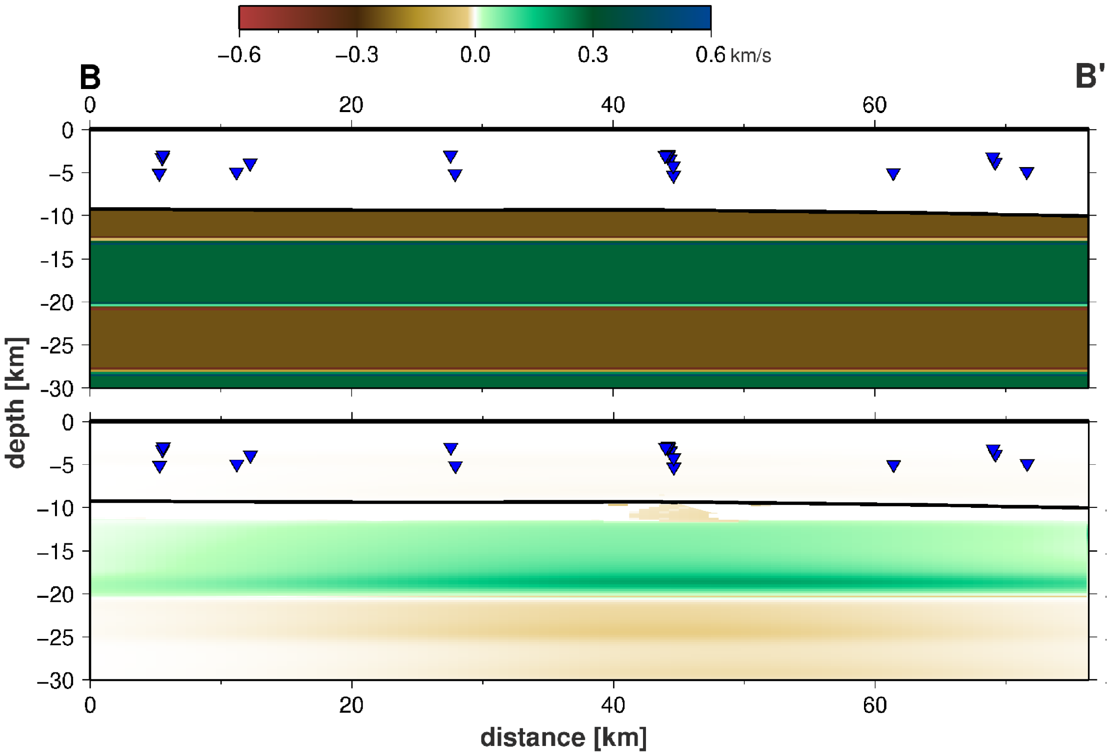

Figure 4.24: *Checkerboard resolution test for profile B-B'. The mantle is well resolved approximately 2-3 km beneath Moho. The mantle is fully resolved where profile A-A' crosses.*

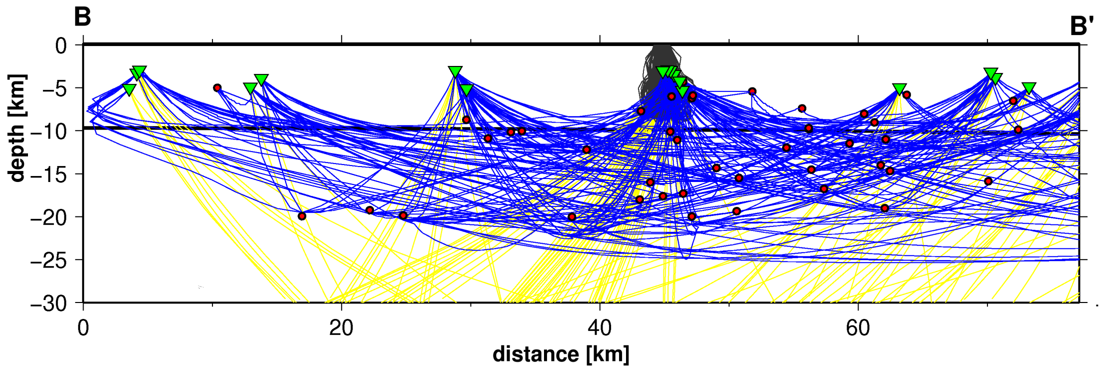

Figure 4.25: *Ray coverage for profile B-B'. Black raypaths are from airgun blasts, blue from local sources and yellow from regional events. Green triangles denote the receivers and red filled circles the local sources.*

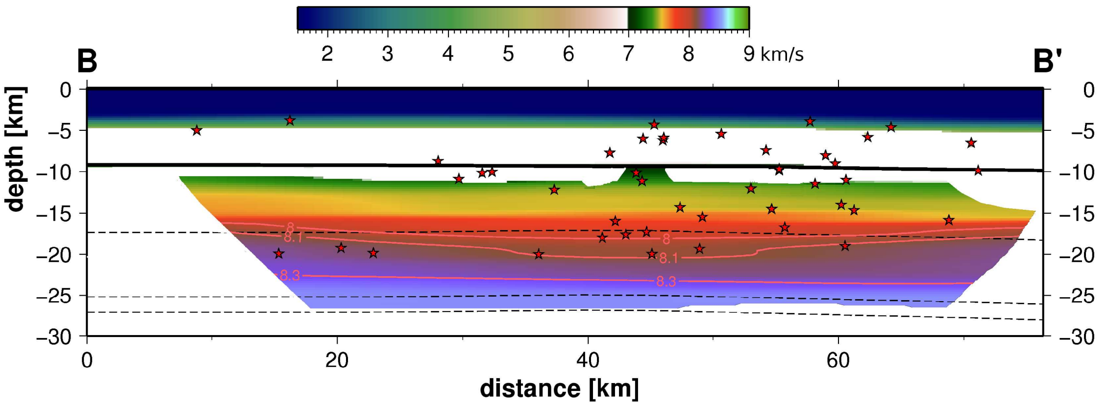

Figure 4.26: *Cross-section through the P-wave model volume. The profile is located parallel to the Middle America Trench (Fig. 4.22).*

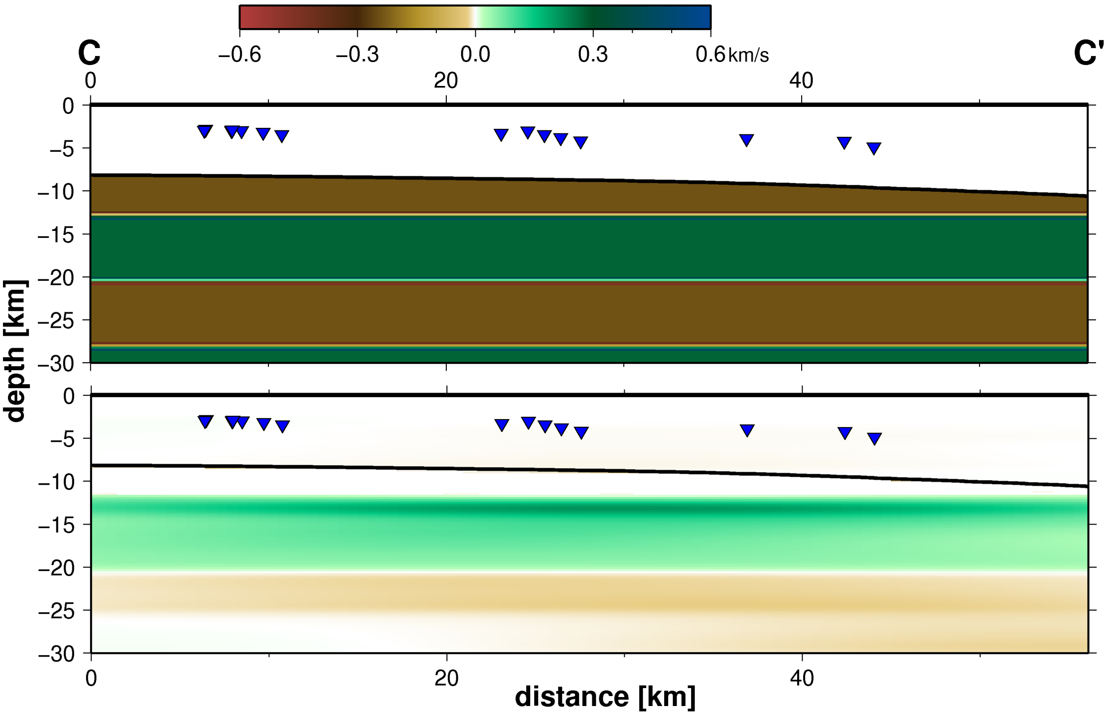

Figure 4.27: *Checkerboard resolution test for profile C-C'. The upper mantle is well resolved.*

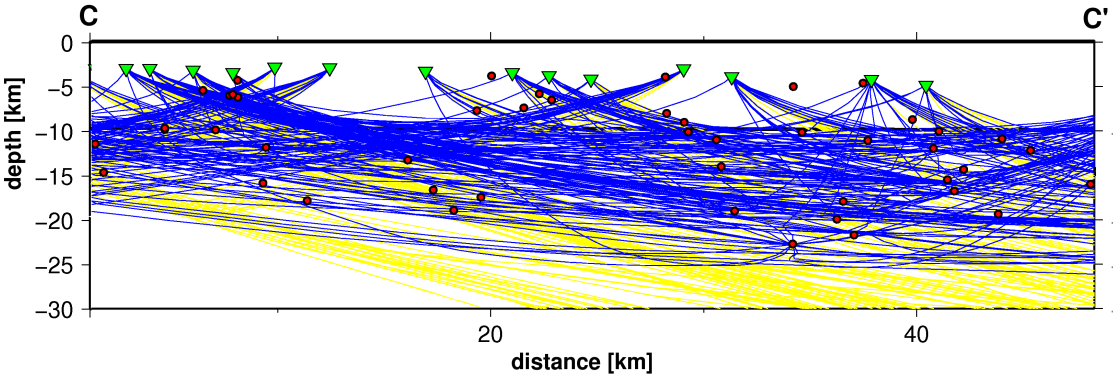

Figure 4.28: *Ray coverage for profile C-C'. Black raypaths are from airgun blasts, blue from local sources and yellow from regional events. Green triangles denote the receivers and red filled circles the local sources.*

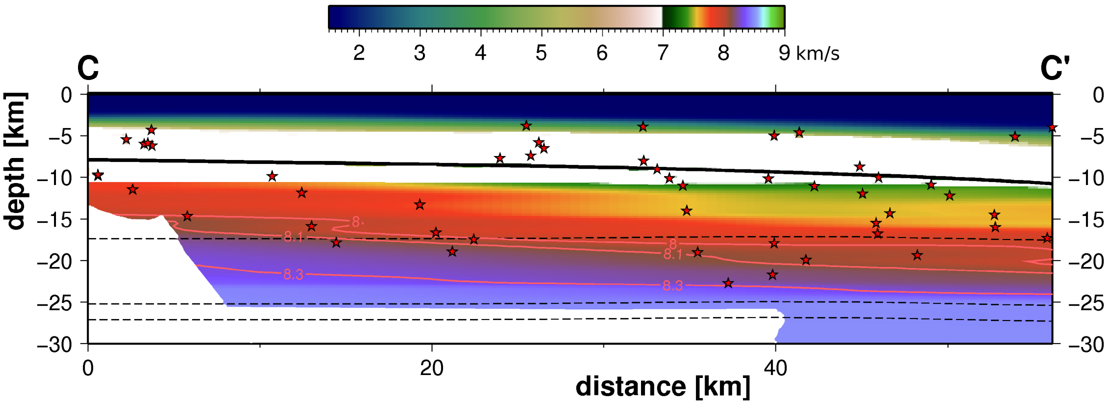

Figure 4.29: *Cross-section through the P-wave model volume. The profile is located perpendicular to the Middle America Trench (Fig. 4.22) and approximately 40 km northwest from profile A-A'.*

Table 4.4: Parameters for all stations of the Outer Rise Network.

Station	Latitude [deg]	Longitude [deg]	Depth [m]	Area[a]
obh10	11°22.85'N	87°47.55'W	4840	II
obh11	11°16.60'N	87°40.92'W	4984	II
obs12	11°10.11'N	87°34.47'W	5296	II
obh13	11° 3.51'N	87°28.22'W	5091	II
obs14	10°56.97'N	87°21.87'W	4892	II
obh16	10°50.48'N	87°15.66'W	5077	II
obh17	11°14.65'N	87°50.72 W	4863	II
obs18	11° 3.80'N	87°40.75 W	4202	II
obh20	11°16.87'N	88° 5.96'W	4170	II
obh21	11° 6.95'N	87°56.55'W	3771	II
obs22	10°57.20'N	87°47.13'W	3445	II
obh23	10°49.46'N	87°30.17'W	3880	II
obh24	10°37.42'N	87°28.50'W	3292	I
obh25	11°10.29'N	88°12.31'W	3440	I
obs26	11° 0.43'N	88° 2.91'W	3160	I
obh27	10°50.60'N	87°53.65'W	2980	I
obs28	10°44.08'N	87°47.32'W	2967	I
obs29	10°30.97'N	87°34.90'W	2912	I
obs30	10°57.32'N	88°12.38'W	2820	I
obs31	10°44.24'N	87°69.97'W	2894	I
obs33	10°37.75'N	88° 6.28'W	3020	I

[a] Stations of area I show a topography of $\sim 600m$, but a comparision with Fig. 1 shows that this is mostly due to surface structure than to the bending (e.g. station obh33 is deeper than obs31 and obh25 has almost the same distance from the trench as obh24).

Chapter 5

Screening the Oceanic Plate

Reduced seismic velocities at deep sea trenches – Implications from teleseismic arrival time residuals

Knowledge of the amount of water that enters a subduction zone is fundamental to our understanding of the Earth's water cycles. When the incoming oceanic plate is forced into the deep sea trench, the strong bending leads to a reactivation or creation of normal faults [*Christensen & Ruff*, 1988; *Hasegawa et al.*, 1994] prior to subduction, which have been inferred to cut deep enough into the mantle to provide a pathway for seawater to penetrate into the lithosphere [*Ranero et al.*, 2003], changing "dry" peridotites to "wet" serpentinites [*Peacock*, 2001; 2003]. Such a mechanism would present an efficient system to transport fluids into the slab and therefore would influence a wealth of subduction zone processes as dehydration at depths of 50-300 km can trigger intermediate-depth earthquakes [*Meade & Jeanloz*, 1991; *Kirby et al.*, 1996] and promotes melt generation under volcanic arcs [*Rüpke et al.*, 2002].

We present results from a unique data set obtained from a dense, local seismic monitoring network deployed in the trench-outer rise offshore Nicaragua. We investigate arrival times of P- and $PKIKP$-phases for several teleseismic earthquakes in 10° to 160° distance from the network. Residuals between synthetic relative arrival times and observed ones show reduced seismic P-wave velocities in the incoming plate seawards the deep sea trench with an evolutionary trend towards it. We explain this with a fractured, serpentinized upper lithosphere.

5.1 Introduction

At subduction zones the incoming oceanic plate bends into the deep sea trench. Following *Chapple and Forsyth* [1979] the bending of the uppermost lithosphere can be described as the flexure of a thin elastic plate, which leads to a tensional regime at the top of the plate, grading into a compressional one at the bottom. Thus, in their model trench-outer rise earthquakes are a consequence of this flexure.

Supported is this model by global compilations of earthquake mechanisms based on waveform inversion, since normal faulting events occur in the uppermost 25 km of the incoming lithosphere meanwhile compressional fault behaviour like thrust faulting dominates the greater depth [e.g., *Seno and Gonzales*, 1987; *Seno and Yamanaka*, 1996].

Further evidence in favor that the incoming plate might become pervasively fractured prior to subduction comes from multibeam bathymetric data of outer rise areas [*Masson*, 1991; *Kobayashi* et al., 1998; *Ranero et al.*, 2003]. At the seafloor, faults have throws of up to 100-500 m and are often 10-50 km long [*Kobayashi et al.*, 1998; *Ranero et al.*, 2003]. Offshore Nicaragua, faulting and fault growth between the outer rise and the trench generate a prominent stairway-like seafloor relief. Single faults might reach depths of up to 10-15 km below Moho [*Ranero et al.*, 2003].

In recent years it has been suggested that the fracturing of the trench-outer rise provides a pathway for fluids to penetrate into the mantle and react with the cold lithospheric material [*Christensen and Ruff*, 1988; *Hasegawa*, 1994; *Ranero et al.*, 2003], changing "dry" peridotites to "wet" serpentinites [*Peacock*, 2001; 2003], which contain up to 13 wt% of water. A wealth of subduction zone processes depend on the amount of water that is carried with the incoming plate into the subduction zone, since the dehydration at greater depths can trigger intermediate-depths earthquakes [*Meade and Jeanloz*, 1991; *Kirby et al.*, 1996] and influence the melt generation under volcanic arcs [*Rüpke et al.*, 2002]. In general considered ways of water transport into the slap are in chemically bound form in sediments and upper crust or trapped in the sediments and in open void spaces in the igneous crust [*Staudigel*, 1996; *Jarrad*, 2003]. Serpentinites would present another delivery system and might even be the most important one [*Raleigh and Paterson*, 1965; *Meade and Jeanloz*, 1991].

Evidence for serpentinization in the upper mantle comes from active seismic tomography. Seismic wide-angle and refraction lines show unusually low P-wave velocities in the crust and upper mantle seawards of the trench axis, especially in a range of approximately 50 km, where bending is the strongest [*Grevemeyer et al.*, 2007]. Mantle velocities are about 5-7 % lower than typical values for the oceanic lithosphere. Such velocity anomalies are best explained by a fractured and serpentinized lithosphere. However, bending-related faults may exceed depths that active seismic tomography could resolve so far.

We present implications from a local earthquake monitoring network, which has been installed at the Outer Rise offshore Nicaragua in 2005. During this period, high quality recordings of P- and $PKIKP$-arrivals from 4 major earthquakes with Mw=4.8 to 7.6 in 10° to 160° were made. Comparison between synthetic and ob-

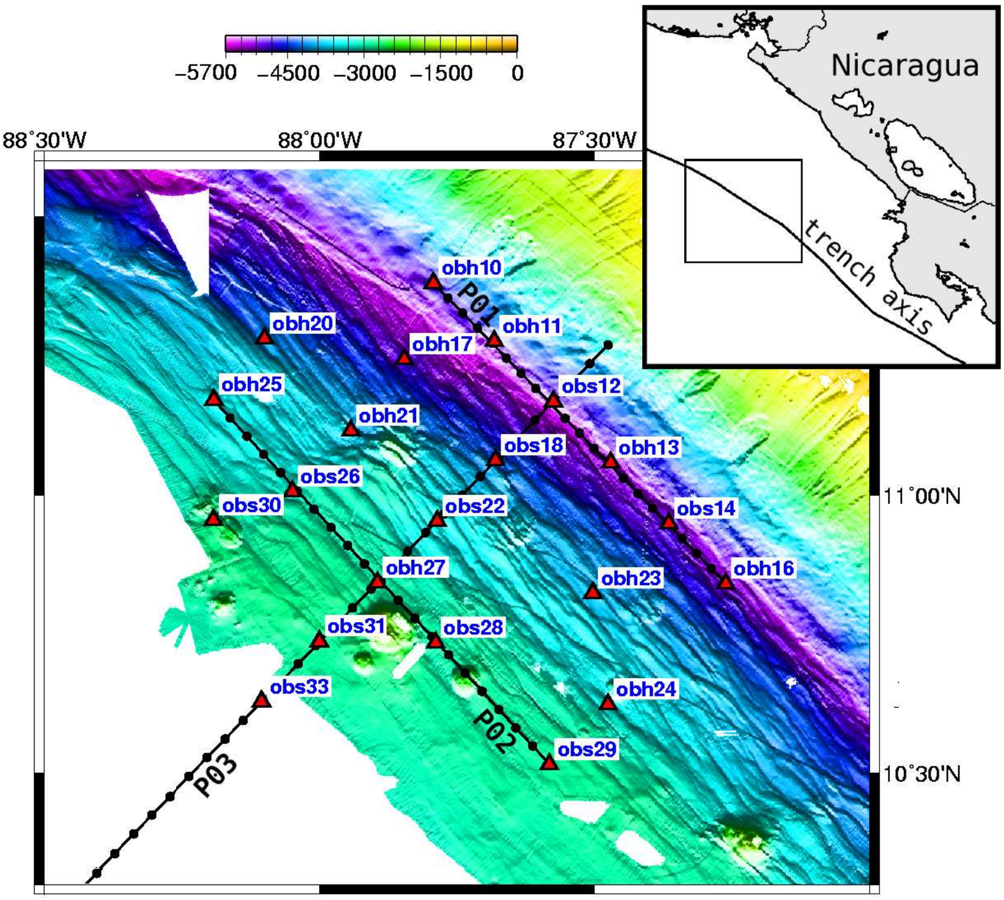

Figure 5.1: *Outer Rise Network and multibeam bathymetry [Ranero et al., 2003] offshore Nicaragua. The bending-related faults are visible throughout the ocean trench slope. At the end of the deployment of the ORN, three seismic wide-angle and refraction profiles have been shot (Dashed lines P01-P03)*

served relative arrival times for all stations in the network show a reduction of seismic velocities seawards the trench with an evolutionary trend towards it.

5.2 Data

The Outer Rise Network (ORN) was deployed during the RV Meteor M66/3 cruise in September 2005 and were recovered after 58 to 61 days. Altogether, 21 instruments provided data, among 10 ocean bottom seismometers (OBS), each equipped with both, a hydrophone and a three-component seismometer and 11 ocean bottom hydrophones (OBH). All sample frequencies were 100 Hz or 125 Hz. The distances between the instruments were 15 to 25 km and in total the network covers an area of 120 km by 110 km (Fig. 5.1).

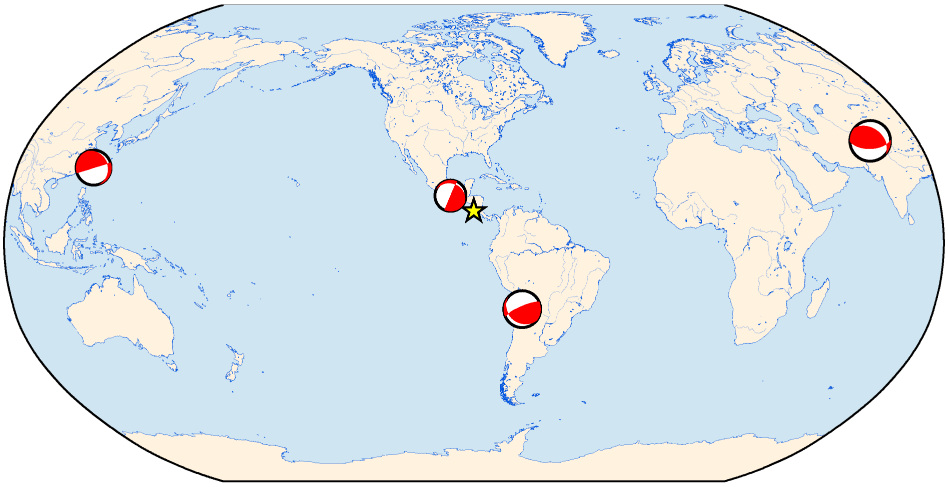

Figure 5.2: *Teleseismic events in this study. Focal mechanism are after Harvard CMT, locations are retrieved from IRIS. The yellow star gives the approximate location of the ORN*

We retrieved location, onset time and magnitude from *IRIS*[1] for approximately 90 teleseismic events with Mw=4.5 to 7.6 that occurred worldwide during the operation time of the ORN. Originally, the ORN was not designed for the recording of teleseismic events and hence no broadband-seismometers were deployed. Thus, long-wavelength first arrivals of teleseismic events are damped and furthermore, the observed noise at the ocean bottom is typically in the same frequency range as the teleseismic records. Therefore, the three-component seismometer traces could not be used and only the hydrophones, which cut off frequencies are below 0.28 Hz [*Thölen*, 2005] provided good data.

Table 5.1: Teleseismic events in this study (data from *IRIS*).

Place	date / time	Mw	Lat,*deg*	Lon,*deg*	depth [km]
Pakistan	2005/10/08 03:50:40.8	7.6	34.54	73.59	26
NE of Taiwan	2005/10/15 15:51:08.3	6.6	25.30	123.26	190
Chile-Bolivia	2005/11/17 19:26:49.9	6.9	-22.36	-67.85	104.70
Mexico	2005/11/06 12:07:17.9	4.7	15.84	-96.03	84.80

Hydrophone traces of four earthquakes (Fig. 5.2, Table 5.1) showed a significant high signal-to-noise ratio (Fig. 5.3) and - in order to determine most precise relative arrival time for all stations in the network - only those events were used.

Picking the arrival of a teleseismic *P*-wave can be difficult, since the smooth onset of a wave with a long wavelength does not show a clear peak in the waveform trace and might be indistinguishable from noise of the same frequency. However, in

---

[1] Incorporated Research Institutions for Seismology - www.iris.edu

the present study, we care for relative arrival times, which provides the possibility to pick any "significant" peak (cp. Fig. 5.4) or to cross-correlate the traces. The latter is only possible if the waveform records from different stations show a high degree of similarity. Usually, this is not the case, since different geological structure beneath the stations (e.g. changes in sedimental or crustal thickness, seamounts, etc.) or poles and zeros of the focal mechanism that are crossing the network lead to different waveforms. These problems are not of importance in the present case, since the oceanic plate is of simple structure with a crustal thickness of 5-6km [*Ivandic et al.*, 2006; *Grevemeyer et al.*, 2007; *Lefeldt et al.*, 2007], which is much smaller than the observed teleseismic wavelength and therefore barely influences the waveform. Further, the stereographic projection of a small network like the ORN on the focal mechanism of a distant quake is represented by a single point. Thus, the amplitude of the first arrival will not vary within the network. Fig. 5.4 gives an example for the similarity of records of different stations. First the onset of the water multiple leads to incommensurable waveforms for stations with different depths. The shallowest station of the ORN was in 2820 m depth. Given a seismic velocity of 1.5 km/s in water, only 3.76 s after the first arrival can be correlated. Fig. 5.5 shows the cross-correlation functions for the waveform example in Fig. 5.4. Throughout all events, the cross-correlation functions show distinct maxima, which can easily be picked and provide relative arrival times.

The error of this method can be estimated following *Chevrot* [2002], whereat the time lag of the autocorrelation function of the reference station is taken on a level with the maxima of the cross-correlation function.

Fig. 5.5 gives an example: stations obh10 is reference station and its autocorrelation function has a maxima of $11.9 * 10^{17}$ counts, whereat the cross-correlation with station obs28 shows at t=1.25s a maxima of $11.4 * 10^{17}$ counts. On this level, the autocorrelation function has a time lag of 62ms, which gives the standard deviation related to the travel time determined for station obs28. This way, seismic records that exhibit a strong correlation with the reference waveform will be attributed low errors, while signals strongly contaminated by noise will produce larger relative travel time errors.

5.3 Synthetic Arrival Times

The travel time of a seismic ray from its source to a particular receiver depends on both, the velocity model and the source location and for teleseismic data, both are commonly associated with large uncertainties. However, these problems simplify if only relative arrival times are to be calculated: the law of refraction,

$$p = \frac{r}{V} = \frac{r sin(i)}{v(r)} = const \quad ,$$

where p is the ray parameter, r is the radius (distance to the center of the earth), V is the slowness, i is the angle of incidence and $v(r)$ is the seismic velocity; implies that in a particular velocity model the ray parameter and hence the slowness is only

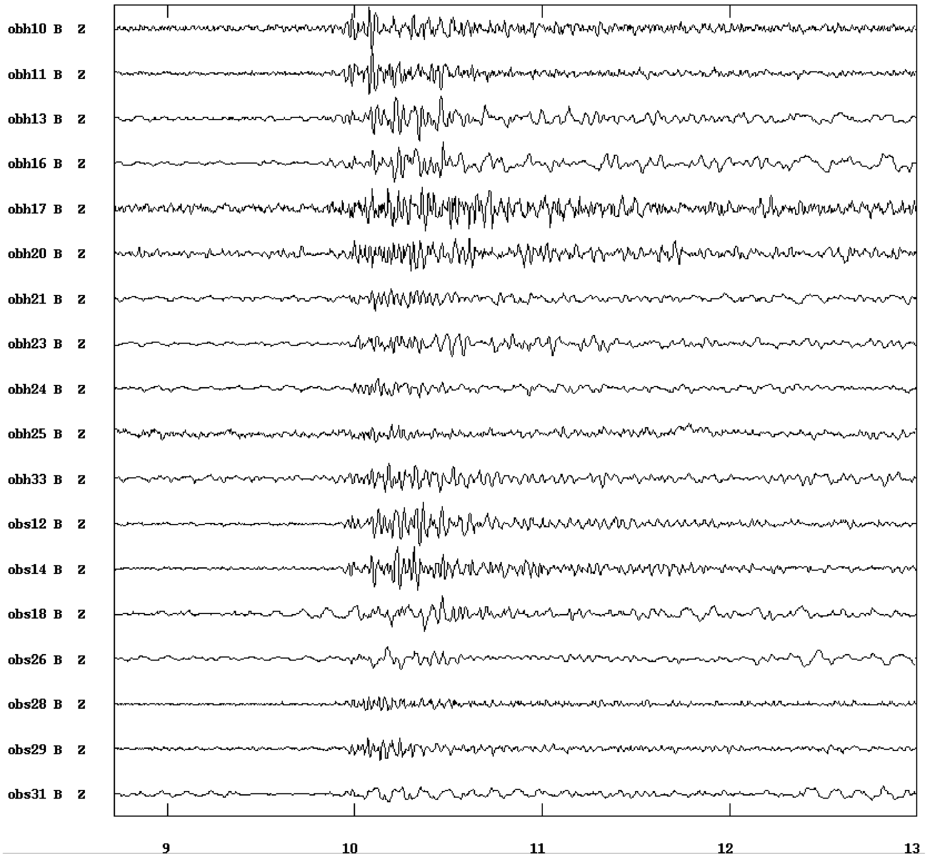

Figure 5.3: *Example for the hydrophone traces and the high signal-to-noise ratio of a teleseismic record (Pakistan-Event).*

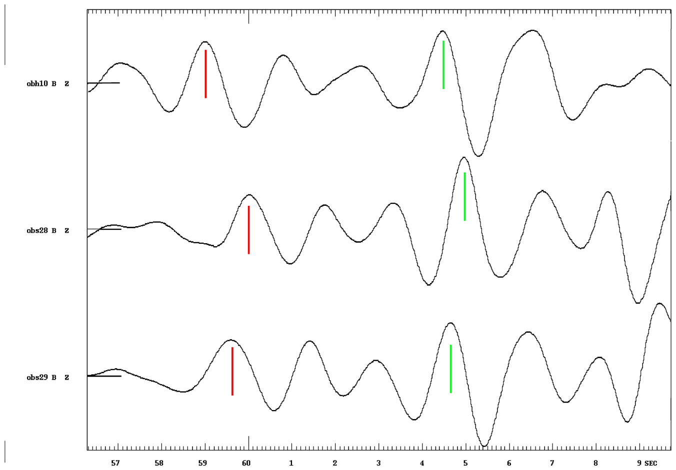

Figure 5.4: *Waveform example for the Taiwan-Event. Red line marks a "significant" peak of the first arrival, green line marks the water multiple. Waveforms are similar before the onset of the water multiple.*

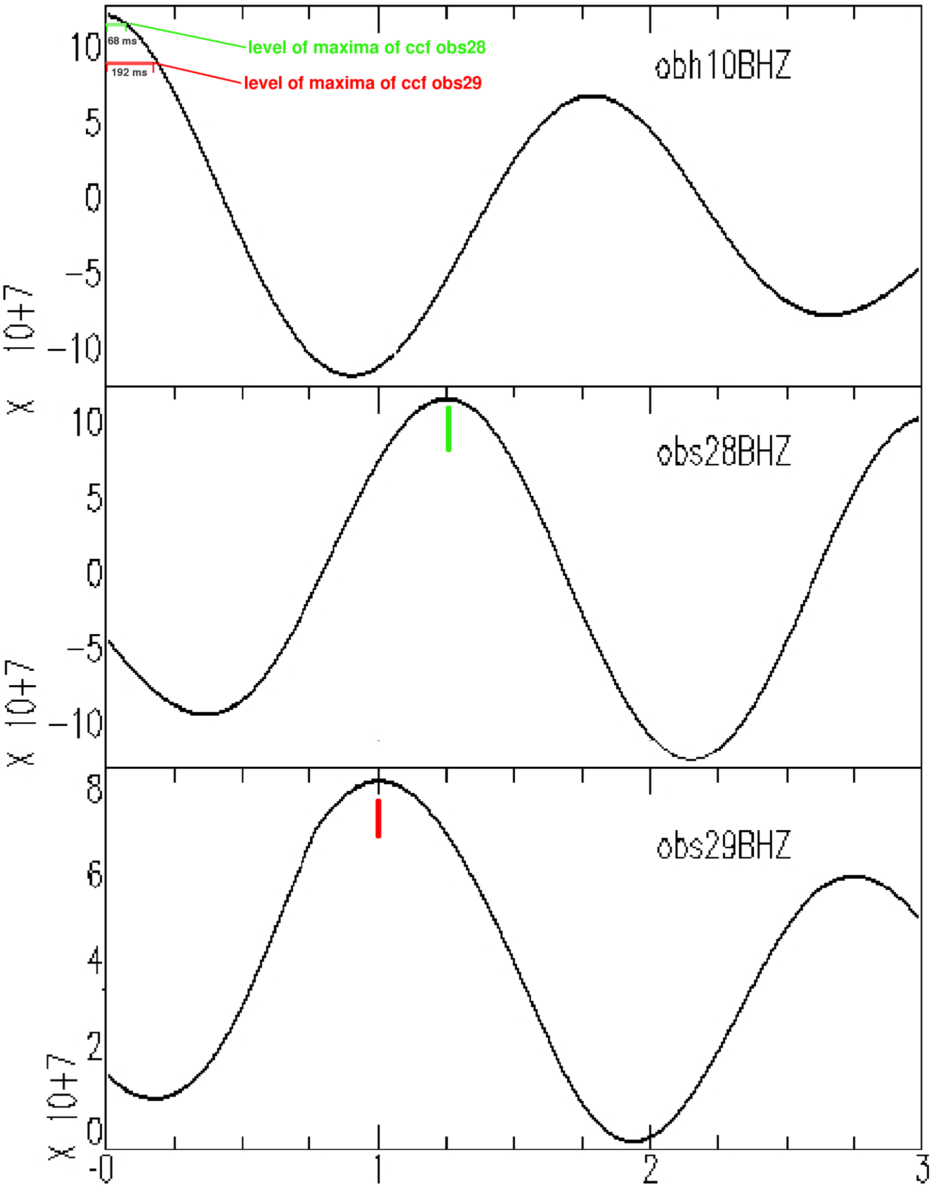

Figure 5.5: *Cross-correlation functions, autocorrelation function respectively, for the waveforms shown in Fig. 5.4 (For each station, the waveform was cut 3.75s after the onset of the first arrival). The correlation suggests a later P-wave arrival at station obs28 (1.25s, green vertical mark) and station obs29 (1s, red vertical mark) than at station obh10, in accordance with the waveforms. Horizontal marks give error estimate (red for obs29, green for obs28) following Chevrot [2002].*

changed, if the radius r or the sinus of the angle of incidence i change. At the source, the angle of incidence is the angle of emission and will not change significantly due to a mislocation of the hypocenter of the source, if this mislocation is small compared to the source-receiver-distance, which is always given for teleseismic events. Further, a mislocation of the focal depth should be small compared to the earth's radius and hence the related change of r is negligible .

A similar argumentation applies for uncertainties in the used velocity model. Considering two nearby receivers and a distant source, the raypaths from this source to the both receivers will not differ significantly from each other. In consequence, changes of the global velocity model apply in the same way for all raypaths, which leaves the relative arrival times untouched [*Lefeldt et al.*, 2007][1].

Thus, residuals between observed and synthetic relative arrival times should rather reflect the local receiver structure than global uncertainties in the velocity model or source location.

Relative arrival times for all events and stations were calculated using the forward solution program from the FMTOMO[2]-package with the $ak135$-travel time tables [*Kennett et al.*, 1995] as world-reference model and a tomographic 3D-velocity model for the ORN [*Lefeldt et al.*, 2007][3].

Table 5.2: Ray parameters for all events in Table 5.1.

Place	ray parameter[a] p	i, deg[b]	distance[c],deg	Phase
Pakistan	1.087	4.61	160.5	$PKIKP$
NE of Taiwan	1.865	7.93	133.2	$PKIKP$
Chile-Bolivia	8.692	40.0	33.57	P
Mexico	13.50	69.2*	10.03	P

[a] Ray parameters were calculated using the TauP Toolkit[1]. [b] the angle of incidence i is calculated from the ray parameter p for a depth of 20km and a seismic velocity of v_p =8.2 km/s (formula: $i = asin[p * 180/\pi * (e_r - 20km)^{-1} * v_p]$ with the earth radius e_r=6371km). [c] Distance from station obh27.
* For this event, the angle of incident is taken from a ray tracing calculation using *fmtomo*.

5.4 Results and Discussion

For each event e and each station i that provided data, observed arrival times $t^{obs}_{rel_{e,i}}$ were determined relative to a reference station, which was chosen arbitrarily, whereat

$$t^{obs}_{rel_{e,i}} = t^{obs}_{abs_{e,i}} - t^{obs,*}_{abs_e}$$

---

[1] cp. section 4.3.3

[2] http://rses.anu.edu.au/∼nick/fmtomo.html

[3] cp. Fig. 4.19

with the absolute arrival time $t_{abs_{e,i}}$ at station i and the absolut arrival time of the reference station $t^{obs,*}_{abs_e}$. In the same way, synthetic relative arrival times $t^{syn}_{rel_{e,i}}$ were calculated.

Residuals between synthetic and observed relative arrival times are shown in Fig. 5.6 and are calculated by $t^{syn}_{rel_{e,i}} - t^{obs}_{rel_{e,i}}$, hence a negative value means a late observed arrival.

For all events, residuals decrease towards the trench, e.g. relative observed arrivals are late compared to synthetic ones for stations nearby the trench, even under consideration of the error margin. As discussed above, residuals of relative arrival times are most likely induced by changes in the local sub-receiver structure and thus, late arrivals indicate a media of reduced velocities beneath the stations nearby the trench, whereat this velocity anomaly seems to expand towards the deep sea trench, starting approximately in 50-60 km distance to the trench axis, where also bending-related faulting becomes a visible feature in the bathymetry (Fig. 5.1).

Late relative arrival times in Fig. 5.6 do not seem to evolve linear with distance from the trench axis, but rather expand strongly between 30 and 50 km and than change only slightly towards the trench. We used a simple method to evaluate the dimension of the late arrivals by taking the arithmetic mean of the residuals of the both furthest seawards stations as starting value (stations are obs31 and obh33; here, the bathymetry shows no bending-related faults, cp. Fig. 5.1) and the arithmetic mean of the residuals of the three stations closest to the trench as final value. The Pakistan and the Taiwan event show an almost similar total residual of ∼200ms (Fig. 5.6), meanwhile the Chile and the Mexico event have higher total residual of ∼250 and 416ms respectively. However, residuals for the Mexico event show a large degree of fluctuations and are therefore excluded from further considerations.

Assuming an area of reduced velocities, an incoming ray will be the more delayed the longer its way through this area is, thus, the flater its angle of incidence is. Table 5.2 gives estimates for the angles of incidence for all events. The $PKIKP$-phases from the Pakistan and Taiwan event arrive under steep, almost vertical angles and hence are less delayed than rays from the Chile event, which arrive under flater angles of $\sim 40°$. (Note, that the angles in Table 5.2 are calculated for oceanic mantle with normal (expected) seismic velocities. Reduced velocities will lead to slightly steeper angles.) Nearby the trench, arrival times of the Chile event are ∼50ms more delayed than of the Pakistan or Taiwan event. Most of this difference was generated in the upper mantle, since the low crustal velocities lead to steep angles of incidence for all events.

Reduced mantle velocities could be explained with a fractured, serpentinized crust and upper mantle. *Ranero et al.* [2003] hypothesized that mantle serpentinite content has a maxima below the Moho and increases linear with depth. Based on this, we will estimate an upper limit for the depth extension of the velocity anomaly. Following *Ivandic et al.* [2006] and *Grevemeyer et al.* [2007], seismic velocities nearby the trench and in the uppermost mantle are in the range of 7.5 to 7.7 km/s in the study area, when expected velocities for unfractured oceanic lithosphere would be 8.2-8.3 km/s. We assume a velocity anomaly with a seismic P-wave velocity of 7.6 km/s below Moho and a linear increase of velocities with depth, until at the depth z an "expected" mantle velocity of 8.3 km/s is reached. For an vertical traveling ray, such a anomaly can be described as an area with the seismic velocity v_a=(7.6 + 8.3)/2 km/s = 7.95 km/s and an extension of z in depth. We will assume the angles of incidence i from Table 5.2 and neglect changes of this angle with depth in the upper mantle. Thus, the simplifications for the velocity anomaly apply for every angle i. The seismic velocity for an unfractured oceanic upper mantle is assumed to be constant v_b=8.3 km/s.

An emitted ray from a source e that passes the area of reduced velocities is delayed by

$$t_d = \frac{z}{v_a cos(i_e)} - \frac{z}{v_b cos(i_e)} \quad .$$

The difference of the total residual from the Pakistan / Taiwan event and the Chile event is Δt ≈50ms, angle of incidence are $cos(i_1) = 40°$ for the latter and $cos(i_2) \approx 6°$ for the former events, which gives

$$\Delta t = z \left[cos(i_1)^{-1} \left(\frac{1}{v_a} - \frac{1}{v_b} \right) - cos(i_2)^{-1} \left(\frac{1}{v_a} - \frac{1}{v_b} \right) \right] \quad .$$

Solving for z and inserting given values leads to

$$z \approx 31.4 km$$

for the depth below Moho of the area of reduced velocities nearby the trench.

This value is comparable high, since other studies [*Ranero et al.*, 2003; *Lefeldt & Grevemeyer*, 2008] suggest that bending-related faults cut 10-20 km deep into the mantle. However, taking into account the many assumptions and simplifications that have been made to carry out the calculation, this value confirms the former studies.

With very simple methods, we succeeded to screen the entire oceanic lithosphere for the first time and document that mantle velocities are reduced. The onset of this reduction coincides with the onset of bending-related faults in the bathymetric data, whereat delay times for teleseismic waves increase from the point of onset towards the deep sea trench.

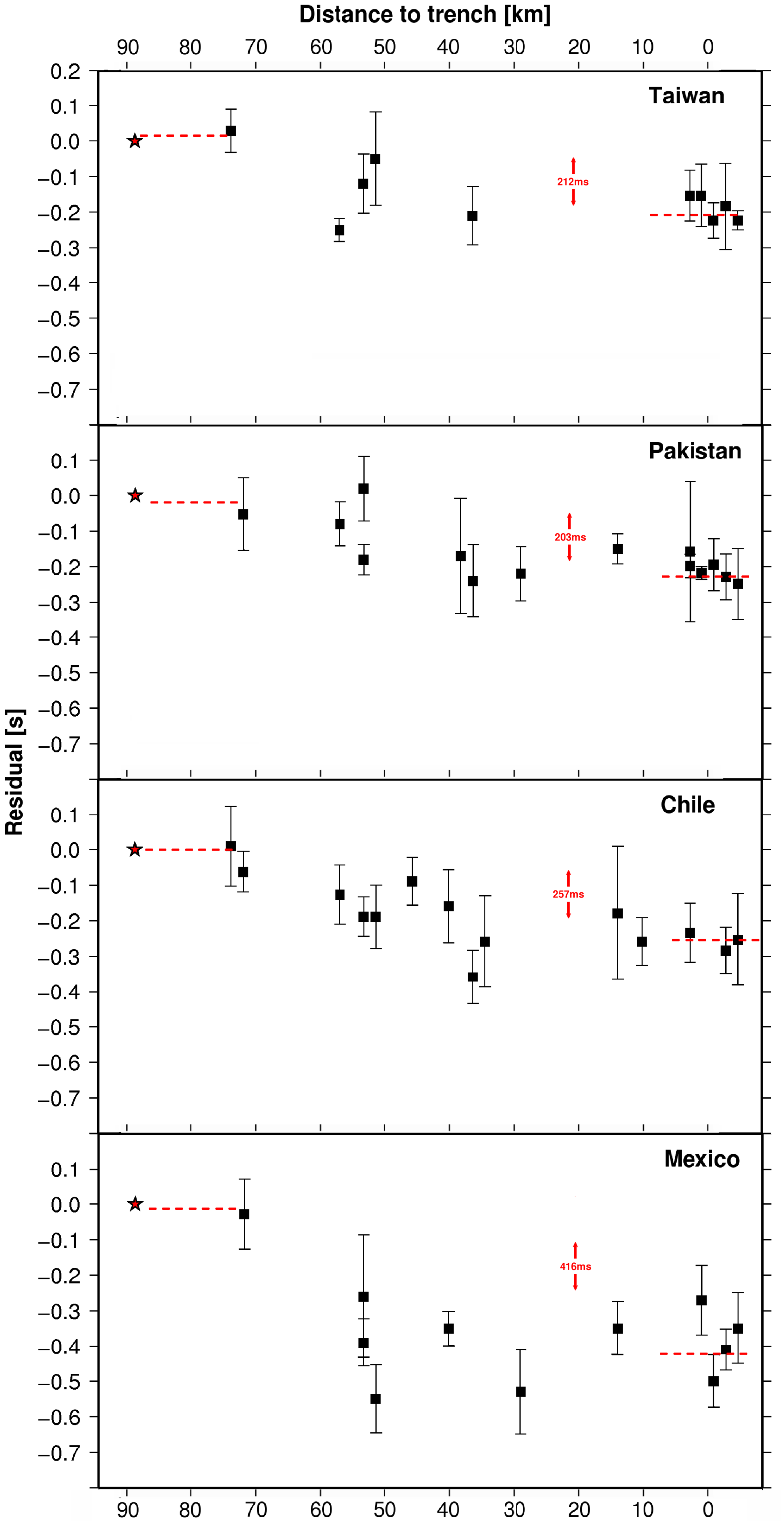

Figure 5.6: *Residuals between observed and synthetic relative arrival times. Black squares represent stations. Distance to the trench was calculated by taking the minimal distance from a station to the deepest points of the trench in the bathymetric data. Red stars give the reference station, which for all events was obh33. Error bars give the standard deviation.*

Chapter 6

Discussion

This study uses three independent methods to (1) proof that trench-outer rise bend-faults cut indeed into the mantle and (2) to document a related change of the mantle's rheology:

1. Local (micro)seismicity was recorded in a particular area of the Nicaraguan trench-outer rise zone. Seawards the trench, earthquakes could only be observed in areas in which bend-faults are a highly visible feature in the bathymetry. Further, an increase in seismic activity nearby seamounts (cp. Fig. 4.18) was documented. Microseismicity reaches up to 15 km deep into the mantle.

   Results from the inversion of the coupled hypocenter-velocity problem show an area of reduced mantle *P*-wave velocities in close proximity of the deep sea trench. The bending-related fracture system in the oceanic crust and upper mantle migth thereby function as a delivery system for seawater to penetrate the mantle and form the fluid-rich mineral serpentinite. If this is the sole cause for the reduction of seismic velocities in the mantle, a total amount of 1.24 - 1.86 wt% stored water and an increase in serpentine content of ∼10-15% respectively in the upper 12 km of the mantle is needed. Though, it cannot not be excluded that bend-faults lead to an increase of fracture porosity in the manner of water-filled cracks in the upper mantle, which could explain reduced seismic velocities as well. Thus, presented values for fluid content are upper limits. However, moment magnitudes, which are commonly below Mw=3.2, seem to decrease towards the trench, in agreement with seismic velocities. At the same time, the number of earthquakes per unit length increases towards the trench. Such a behavior migth be explained by a weak, serpentinized lithosphere.

   The most outstanding result of this experiment comes from the determination of focal mechanisms for several local earthquakes: shallow events in the uppermost 4-9 km of the mantle have a tensional mechanism, which allows seawaters to migrate into deeper layers, meanwhile compressional stresses seem to govern the rupture behavior of deeper earthquakes, which implies a barrier for fluids at the intersection between both stress regimes (neutral plane). This has not been taken into account in any previous study and thus the depth of mantle serpentinization has either been linked to the maximum depth that bend-faults cut into the lithosphere or the location of the 600°C - 650°C isotherms [e.g. *Ranero et al.*, 2003]. Both are deeper than the neutral plane and therefore led to upper limits for fluid contents that are 5-10 times higher than given in this study.

2. The same network described above provided as well data of teleseismic events in distances of 10° to 160°. Seismic rays from the furthest events arrive under almost vertical angles. Travel time picks from these events were compared to synthetic (predicted) arrival times and it could be shown that seismic rays are delayed at receivers nearby the deep sea trench compared to receivers further seawards. This observation is related to changes in the sub-receiver geology, which implies an area of reduced velocity close to the trench in agreement with the results of the tomographic inversion. Even though this result only confirms the findings from the tomographic inversion procedure, the simple nature of this experiment provides a strong, coherent and independent argument for the evolutionary process of the reduction of seismic mantle velocities at the trench-outer rise and therefore relates bending-related faulting and changes of the lithosphere's rheology.

3. Seven teleseismic earthquakes at the outer rise offshore Central America with Mw>5.5 have been investigated by using a non-linear relocation algorithm and a sophisticated body wave moment tensor inversion procedure. The results show that major earthquakes in this area occur at shallow depth (10-25 km beneath seafloor) and commonly change their fault mechanism during the rupture from tensional normal fault behavior at the outset to compressional thrust fault or strike-slip behavior in greater depths. Further, the dimension of the fault planes shows an unusual aspect ratio of 5 to 10 km in dip direction and 25 to 50 km in strike direction.

   Taken into account that bending-related faults can be tracked for ∼50 km in the bathymetric data and that results from both, local earthquake tomography presented in this study and active seismic reflection experiments [*Ranero et al.*, 2003] suggest in agreement a maximum rupture depth of 10 to 15 km into the mantle, the given aspect ratios imply that during a major earthquake an entire bend-fault ruptures.

   The change of the fault mechanism suggests that the rupture is initiated within the tensional stress regime and continues into the compressional area. This result confirms models of *Chapple and Forsyth* [1979] and *Christensen and Ruff* [1988] and it is the first time that this could be shown with a single earthquake.

   Furthermore, a comparison with data from *Harvard CMT Catalog* highlights that major trench-outer rise events occur after major interplate events in the joining area, i.e. when the oceanic and the continental plate are partly decoupled. Therefore, teleseismic outer rise earthquakes seem to be rather slab-pull than bending related.

Combining these results, this study could firstly determine the typical hypocenter depths of trench-outer rise earthquakes. Thereby, the maximum focal depths of 15 km beneath Moho (microseismicity) to 20 km (teleseismicity) may coincide with the maximum depth that bend-faults cut into the mantle: focal mechanisms of the deepest events seem to be of up-going, compressional character, which implies that the determined focal depths present the deepest (initial) point of the rupture and the bend-fault respectively. However, the depth that serpentinization reaches is determined by the stress regimes in the lithosphere and not by the depth to which bend-faults cut.

Teleseismic events and microseismicity

One emerging question when comparing item 1. and 3. is: If a decrease of magnitudes of microseismic events towards the trench is indeed a sign for a weak lithosphere, how can the occurrence of teleseismic events with Mw$\geq$5.5 in the close proximity of the trench (cp. Fig. 3.2) be explained?

Following *Christensen and Ruff* [1988], the depth of the neutral plane changes both, temporally and spaciously, depending on the degree of coupling between the oceanic and the continental plate. A major interplate event releases stress between the plates and thereby decouples them; thus, the pulling sinking slab extends the tensional regime downwards. As documented in sec. 3.9, large trench-outer rise events are most likely slab-pull related, i.e. they occur when the both plates are decoupled. In that state, the tensional regime reaches into the "dry" (not serpentinized) area, which has a strong rheology that allows for normal fault earthquakes of larger magnitudes. During the rupture, water might be able to penetrate into deeper layers, but is pressed out immediately when the coupling of the plates becomes stronger and the neutral plane moves upwards. The short time in between is probably not enough to cause serpentinization, which is a slow process.

Thereby I assume that the both plates were relatively strong coupled during the deployment of the ORN, since a large earthquake occurred ~ 30 km landwards of the Middle America Trench (11/18/05, Mw=5.5, according to *IRIS-DMC* archive) and close-by the ORN shortly before the ORN was recovered. Most likely this was an interplate event, which decreased the degree of coupling between the plates. Supported is this by the occurrence of two major normal fault events 8 and 12 months later at the former location of the ORN (07/25/06; 11/18/06, after *Harvard CMT*).

That would also explain the observation of two outer rise earthquakes with compressional mechanism (Fig. 4.19) in the ORN data set. As we pointed out in section 4.6.1, the (non-symmetric) bending of a tectonic plate alone can only lead to tensional earthquakes, otherwise an additional compressional force needs to be applied, i.e. stress due to the coupling of the plates must be higher than due to the slab-pull. Further, in our model, we divide the oceanic brittle mantle into an upper part with a "weak" serpentinite-like rheology and a "strong" peridotite-like lower part, both with different yield strains. As a consequence, normal fault events are only of small magnitude if the both plates are stronger coupled and the tensional stress regime covers but the weak upper mantle - in accordance with the observations. Thus, the model we present extends existing models of *Chapple and Forsyth* [1979] and *Christensen and Ruff* [1988] and combines tele- and microseismic observations.

Transport of seawater through sediments and crust

Fisher et al. [2003] documented that seamounts can introduce a circulation of fluids throughout the oceanic crust. We find an increase in seismicity in close proximity of a seamount (Fig. 4.18). Absolute P-wave velocities for profile A-A' (Fig. 4.19) show a clear and distinct reduction of seismic velocities in the crust beneath the seamount.

However, meanwhile absolute velocities highlight the evolutionary trend of the reduced velocity anomaly, a comparison between input 1D-model (Fig. 4.11) and final 3D-model can unveil further details: Fig. 6.1 shows that the strong reduction of seismic velocities is restricted to an area that starts nearby seamount 01 and extends ~ 50km trenchwards. Seamounts can redound to a hydrothermal recharge and discharge across 50 km [*Fisher et al.*, 2003], i.e. can breach the sediment cover that isolates the oceanic crust and lead to a communication with the overlying seawater. Once the crust is hydrated, a rupture that cuts through the Moho into the upper mantle could easily carry fluids with it. Thus, seamounts may play an important role in the hydration process of the oceanic plate.

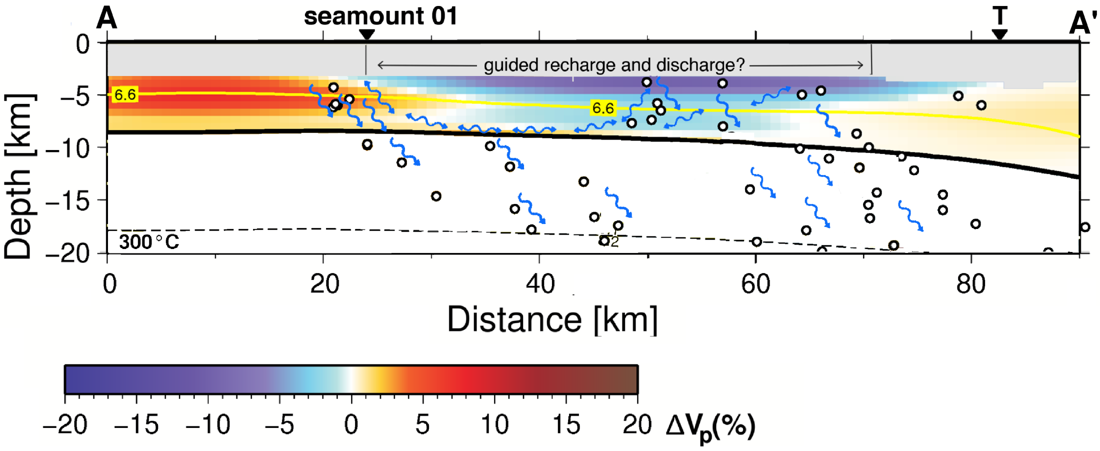

Figure 6.1: *Crustal P-wave anomalies (profile A-A'). Earthquakes are indicated by white circles. 'T' denotes the location of the trench. 300° C-Isotherm has been calculated using the code of McKenzie et al. [2005]. Blue arrows show possible fluid transport. 6.6 km/s isovelocity line is plotted in yellow.*

Water budget of the Nicaraguan subduction zone

Water can enter a subduction zone as pore-water or as chemically bound water. Thereby, recent numerical modelling studies [*Hensen and Wallmann*, 2005; *Haeckel*, 2006] indicate that pore-water contained in the sediments is expelled within the first 10-20 km after subduction. Expulsion pathways of pore-water carried by the igneous crust are mostly unknown, but following *Jarrad* [2003] this water should be quantitatively lost at shallow subduction depths reached within the forearc. Thus, considerations of fluid flux with respect to the volcanic arc and the earth's deep water cycle can be limited to structured water.

Therefor previous studies derived a sedimental input of 0.04 $gm^{-1}s^{-1}$ [*Wallmann*, 2001] and a crustal, respectively upper mantle input of 0.53 $gm^{-1}s^{-1}$ [*Jarrad*, 2003]. Mantle serpentinization was not taken into account, but can provide an additional input of up to 1.2 - 1.75 $gm^{-1}s^{-1}$ and thus is the major source of structured water in the Nicaraguan subduction zone.

However, *Freundt and Kutterolf* [2007] estimated volcanic fluxes of 0.19 $gm^{-1}s^{-1}$ for Nicaragua, which presents only 8-11% of the input of bound water. Even though low velocity zones in tomographic images of the slab [*Dinc-Acdoban*, 2007] imply that several reservoirs beneath the forearc and volcanic arc may take up a significant amount of subducted water, a recent study of *Peacock et al.* [2005] might suggest that the vast majority enters the earth's deep water cycle: thermal structure models of Nicaragua (Fig. 6.2) show that the subducted upper mantle does not exceed temperatures of $\sim 600°C$ beneath the volcanic arc and therefore serpentinites might not be dehydrated and thus reaches greater depths.

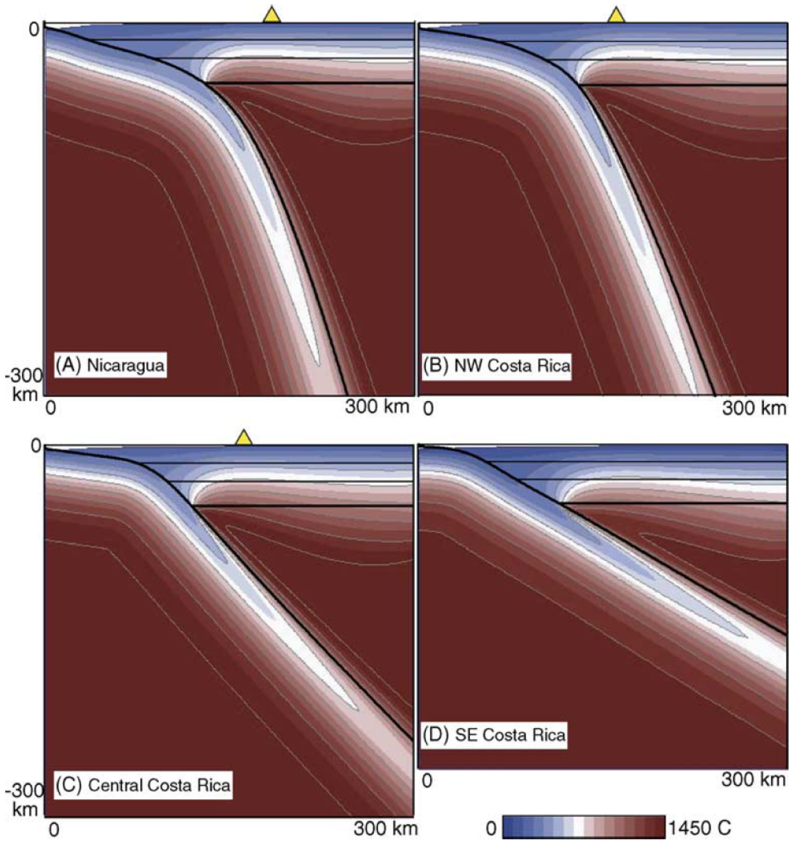

Figure 6.2: *Calculated thermal structure for four different transects across Central American subduction zone [Peacock et al., 2005] using an olivine mantle–wedge rheology. Bold lines represent top of subducting slab and top of convecting mantle–wedge. Thin horizontal lines represent mid-crust (15 km depth) and Moho (30 km) of overriding plate. Contour interval = 100 °C. (A) Nicaragua, (B) NW Costa Rica, (C) Central Costa Rica, (D) SW Costa Rica.*

Chapter 7

Outlook

Even though the amount of seawater in the subducted mantle might not be as large as proposed, yet the results of this study leave the potential for trench-outer rise mantle hydration to play an important role for the water cycle in subduction zones.

However, two questions remain:

- What is the exact amount of fluids in the incoming mantle? Thus, what fraction of the reduced velocity anomaly is caused by serpentinite and what part by fracture porosity?
- Are the results of this study transferable for all subduction zones or is the Nicaraguan subduction zone exceptionally?

Normal fault trench-outer rise earthquakes are a global feature [*Chapple & Forsyth*, 1979] and bathymetric data from the trench-outer rise offshore Chile [*Grevemeyer et al.*, 2003] shows a similar stairway-like seafloor relief generated by bending-related faults. Both argues for mantle hydration as a global quality, but as aforementioned, the hydration of the incoming Nicaraguan plate seem to be two to three times higher than inferred for other slabs [*Abers et al.*, 2003].

The decrease of moment magnitudes towards the trench axis (cp. 4.6) suggests a weakened lithosphere and therefore favours serpentinite as cause for reduced mantle velocities over fracture porosity, but the ORN was deployed for only two months. A longer duration is needed to determine if this observation is a characteristic. Ideally, microseismicity should be observed before and after a major (teleseismic) event in the area, since the associated change of the stress regime is significant. The determination of magnitudes over distance and depth for a long period might make it possible to define the strength of the minerals in the mantle, which in turn could be linked to the degree of hydration.

Another promising approach is the investigation of shear waves, especially in the active seismic wide-angle and refraction experiments. Synthetic models [*Ivandic*, priv. comm.] imply that the Poisson-ratio for peridotite, with water-filled cracks and no occurrence of serpentinite, is significantly different from partly serpentinized peridotite, even though the P-wave velocity is equal. Furthermore, the Poisson-ratio is a function of the angle under which the seismic ray meets a water-filled crack and a layer of serpentinite respectively, but the functions for both medias differ from each other. Thus, a P- and a S-wave tomographic inversion for profiles of different directions (e.g. parallel and perpendicular to the trench axis) could shed more light on the matter.

In 2008, the 3rd phase of sponsorship of the SFB 574 will start. The subproject A5, of which this thesis is contribution, will focus on the subduction zone offshore Central Chile. Next to a seismic refraction and wide-angle experiment, a long-duration outer rise network is planned as a part of a onshore/offshore seismic network. Provision is made for broadband seismometers at the outer rise. A clear recording of P- and S-waves from regional and local seismicity as well as from airgun blasts, shall make it possible to determine the amount of water in the mantle of the incoming Nasca Plate. If the plate is hydrated, there might be the possibility to relink reduced velocity and hydration to the Nicaragua data and to generate a global model.

Therefore, I suggest the common design of a seismic network (similar or equal spacing between all stations) to be changed into a network with a dense core surrounded by a few stations with greater spacing in the outer field, in total covering a larger area. The ORN experiment has shown that recordings from the furthermost stations of the epicenter of an earthquake importantly contributed to the determination of the focal depth. In the suggested geometry, the outer field stations might help to determine even more accurate focal depths. Also, it is generally difficult to determine focal solutions of deeper earthquakes from a small network, since no poles or zeros may cross. Outer field stations shall provide a solution for this problem as well.

Further, it is my suggestion to have as many stations on the ocean bottom as possible, when seismic wide-angle and refraction profiles are shot. Stations that are not part of the 2D-profile can still provide 3D-information. Hence I propose that a consistent inversion with all information - active and passive seismic data - is carried out.

References

Abers, G.A., T. Plank and B.R. Hacker (2003), The wet Nicaragua slab, *Geophys. Res. Lett.*, *30*(2), 1098.

Aki, K. and P. Richards (1980), Quantitative Seismology: Theory and Methods. *W.H. Freeman and Co.*, San Francisco.

Allerton, S., H.U. Worm & L.B. Stokking, L.B. (1996), Paleomagnetic and rock magnetic properties of Hole 896A. *Proc. Ocean Drill. Program Sci. Results*, vol. 148, 217–226.

Barckhausen, U., C.R. Ranero, R. von Huene, S.C. Cande & H.A. Roeser (2001), Revised tectonic boundaries in the Cocos Plate off Costa Rica: implication for the segmentation of the convergent margin and for plate tectonic models, *J. Geophys. Res.*, **109** (B9), 19207- 19220

Barth, G.A. & J.C. Mutter (1996), Variability in oceanic crustal thickness and structure: Multichannel seismic reflection results from the northern East Pacific Rise. *J. Geophys. Res.*, vol. 101, 17951–17975.

Berhorst, A. (2006) Die Struktur des aktiven Kontinentalhangs vor Nicaragua und Costa Rica - marin-seismische Steil- und Weitwinkelmessungen, *PhD thesis*, Christioan-Albrechts-Universität, Kiel

Bird P. (2003), An updated digital model of plate boundaries. *Geochem. Geophys. Geosyst.*, vol. **4**, 1027, doi:10.1029/2001GC000252.

Burbach, GV, C. Frolhich, W.D. Penington, and T. Matumoto (1984), Seismicity and Tectonics of the Subducted Cocos Plate, *J. Geophys. Res.*, *89*, 7719-7735.

Canales, J.P., Detrick, R.S., Toomey, D.R. % W.S.D. Wilcock (2003), Segment-scale variations in the crustal structure of 150–300 kyr old fast spreading oceanic crust (East Pacific Rise, 8°15'N-10°5'N) from wide-angle seismic refraction profiles. *Geophys. J. Int.*, vol. 152, 766-794.

Carbotte, S. & K. Macdonald (1992), East Pacific Rise 8°-10°31'N: Evolution of ridge segments and discontinuities from SeaMARC II and three-dimensional magnetic stdies. *J. Geophys. Res.*, vol. 97, 6959–6982.

Carlson, R.L., and D.J.Miller (2003), Mantle wedge water contents estimated from seismic velocities in partially serpentinized peridotites: *Geophysical Research Letters*, v. *30*, 1250. doi: 10.1029/2002GL016600.

Chapple, W.M. and D.W. Forsyth (1979), Earthquakes and bending plates at trenches, *J. Geophys. Res.*, *84*, 6729-6749.

Chevrot, S. (2002), Optimal measurement of relative and absolute delay times by simulated annealing, *Geophys. J. Int.*, **151**, 164–171

Christensen, D.H. & L. Ruff, (1983) Outer-rise earthquakes and seismic coupling. *Geophys. Res. Lett., 10*, 697-700.

Christensen, D.H. and L. Ruff (1988), Seismic Coupling and outer rise earthquakes. *J. Geophys. Res.*, *93*, 13421-13444.

Conner, R.D., Johnson, W.L., Paton, N.E. & Nix, W.D. (2003), Shear bands and cracking of metallic glass plates in bending, *J. Appl. Phys.*, v. 94/2, p. 904-911, doi: 10.1063/1.1582555

Crosson, R.S. (1976), Crustal structure modeling of earthquake data; 1, Simultaneous least squares estimation of hypocenter and velocity parameters, *J. Geophys. Res.*, *81* (17), 3036-3046.

Dahm, T. and G. Manthei and J. Eisenblätter (1999), Automated moment tensor inversion to estimate source mechanisms of hydraulically induced micro-seismicity in salt rock, *Tectonophysics*, *306*, doi:10.1016/S0040-1951(99)00041-4

DeMets, C. & T.H. Dixon, (1999) New kinematic models for Pacific-North America motion from 3 Ma to present, I: Evidence for steady motion and biases in the NUVEL-1A model. *Geophys. Res. Letters*, v. 26, 1921-1924.

Dinc Akdogan, A.N., M. Thorwart, Y. Dzierma, W. Rabbel, , E.R. Flueh, J. Gossler, W. Taylor, G.E. Alvarado (2007), Seismicity of Southern Nicaragua and Northern Costa Rica : A Combined Offshore and Onshore Study, *LAK 2007*: 20th Colloquium on Latin American Earth Sciences, abst. 793

Dowrick, D.J., & D.A. Rhoades (2004), Relations between Earthquake Magnitude and Fault Rupture Dimensions: How Regionally Variable are They? *Bull. Seismol. Soc. Am.*, **94**, 776-788.

Dziewonski, A.M. & D. L. Anderson (1981), Preliminary reference Earth model. *Physics of the Earth and Planetary Interiors* **25**, S.297 356

Eberhart-Phillips, D., and A.J. Michael (1993), Three-dimensional velocity structure and seismicity in the Parkfield region, central California, *J. Geophys. Res.*, *98*, 15,737-15,758

Engdahl, E.R. & A. Villaseñor (2002), Global Seismicity: 1900 1999, in W.H.K. Lee, H. Kanamori, P.C. Jennings, and C. Kisslinger (editors), *International Handbook of Earthquake and Engineering Seismology*, Part A, Chapter 41, pp. 665-690, Academic Press,

Escartin, J., Hirth, G. & Evans, B. (2001), Strength of slightly serpentinized peridotites: implications for the tectonics of oceanic lithosphere. *Geology* 29, 1023-1026.

Fisher, A.T., Davis, E.E., Hutnak, M., Spiess, V., Zühlsdorff, L., Cherkaoui, A., Christiansen, L., Edwards, K.M., Macdonald, R., Villinger, H., Mottl, M.J., Wheat, C.G. & Becker, K. (2003), Hydrothermal recharge and discharge across 50 km guided by seamounts on a young ridge flank, *Nature*, *421*, 3618-3621.

Forsyth, D.W. (1982), Determinations of focal depths of earthquakes associated bending of oceanic plates at trenches, *Phys. Earth Planet. Int.* **28**, 141-160.

Fuchs K. (1968), The reflection of spherical waves from transition zones with arbitrary depth-dependent elastic moduli and density, *J. Phys. Earth*, *16*: 27-41. special issue.

Fuchs K. and Müller G. (1971), Computation of synthetic seismograms with the reflectivity method and comparison with observations. *Geophys. J. R. astr. Soc.*, *23*(4): 417-433.

Graeber, F. (1997), Seismische Geschwindigkeiten und Hypozentren in den sdlichen zentralen Anden aus der simultanen Inversion von Laufzeitdaten des seismologischen Experiments PISCO'94 in Nordchile, *Scientific Technical Report STR97/17*, GeoForschungszentrum, Potsdam.

Green, H.W. & H. Houston (1995), The mechanics of deep earthquakes, *Ann. Rev. Earth Planet. Sci.* **23**, 169-213.

Grevemeyer, I., J.L. Diaz-Naveas, C.R. Ranero, H. Villinger (2003), Ocean Drilling Program Leg 202 Scientific Party, Heat flow over the descending Nasca plate in Central Chile, 32°S to 41°S; evidence from ODP Leg 202 and the occurence of natural gas hydrates, *Earth planet Sci. Lett.* 213, 285-298

Grevemeyer, I., N. Kaul, J.L. Diaz-Naveas, H. Villinger, C.R. Ranero and C. Reichert (2005), Heat flow and bending-related faulting at subduction trenches: case studies offshore of Nicaragua and Central Chile, *Earth Planet. Sci. Lett.* **236**, 238-248.

Grevemeyer, I., C.R. Ranero, E.R Flueh, D. Klaeschen and J. Bialas (2007), Passive and active seismological study of bending-related faulting and mantle serpentinization at the Middle America trench, *Earth Planet. Sci. Lett.*, **258**, 528-542

Gripp, A.E & R.G. Gordon (2002), Young tracks of hotspots and current plate velocities. *Geophys. J. Int.*, vol. 150, 321–361, http://tectonics.rice.edu/hs3.html.

Hacker, B.R., S.M. Peacock, G.A. Abers & S.D. Holloway (2003), Subduction factory 2. Are intermediate-depth earthquakes in subducting slabs linked to metamorphic dehydration reactions? *J. Geophys. Res.* **108**, doi:2010.1029/2001JB001129.

Haeckel, M. (2006), A transport-reaction model of the hydrological systems of the Costa Rica subduction zone. *In:* J.D. Morris, H.W. Villinger, A. Klaus (eds), Proc. ODP, *Sci. Res.*, 205: 1-26

Hasegawa, A., S. Horiuchi and N. Umino (1994), Seismic structureof the northeastern Japan convergent margin: *A synthesis. J. Geophys. Res.*, *99*, 22295-22311.

Havskov, J., and L. Ottemöller (1999), SeisAn earthquake analysis software. *Seismological Research Letters*, *70*, 532-534.

Hensen, C. and Wallamnn, K. (2005), Methane formation at Costa Rica continental margin - constraints for gas hydrates inventories and cross-décollement fluid flow. *Earth Planet. Sci. Lett.*, **236**, 41-60.

Hey, R. (1977), Tectonic evolution of the Cocos-Nazca spreading center. *Geol. Soc. Am. Bull.*, 88, 1404–1420.

Husen, S., E. Kissling, E. Flueh, and G. Asch (1999), Accurate Hypocentre Determination in the Seismogenic Zone of the Subducting Nazca Plate in Northern Chile Using a Combined On-/Offshore Network, *Geophys. J. Int.*, *138*, 687-701.

Hyndman, R.D. & K. Wang (1993), Thermal constraints on the zone of ma jor thrust earthquake failure: the Cascadia subduction zone, *J. Geophys. Res.* **98**, 2039 - 2060.

Ivandic, M., Grevemeyer, I., Flueh, E. R. and McIntosh, K. (2006), Structure and hydration of the subducting plate offshore Nicaragua, *Eos Trans. AGU*, *87* (52), Fall Meet. Suppl., Abstract V51F-01

Jackson J. & T. Fitch (1979), Seismotectonic implication of the relocation aftershock sequences in Iran and Turkey: an application of the master event technique, *Geophys J R astr Soc*, **57**, 209-229

Jarrad, R.D. (2003), Subduction fluxes of water, carbon dioxid, chlorine, and potassium. *Geochemistry, Geophysics, Geosystems*, *4*: doi: 10.1029/2002GC000392.

Kanamori, H. (1971), Seismological evidence for lithospheric normal faulting: the Sanriku earthquake of 1933, *Phys. Earth planet. Inter.*, *4*, 289-300.

Kennett, B.L.N. Engdahl, E.R. & Buland R. (1995), Constraints on seismic velocities in the Earth from travel times, *Geophys J Int*, **122**, 108-124

Kikuchi, M. & H. Kanamori (1982), Inversion of complex body waves, *Bull. Seism. Soc. Am.*, *72*, 491-506.

Kikuchi, M. & H. Kanamori (1986), Inversion of complex body waves II, *Physics of the Earth and Planetary Interiors*, v. *43*, p. 205 222.

Kikuchi, M. & H. Kanamori (1991), Inversion of complex body waves III, *Bull. Seism. Soc. Am.*, *81*, 2335-2350.

Kikuchi, M., H. Kanamori and K. Satake (1993), Source complexity of the 1988 Armenian earthquake; evidence for a slow after-slip event, *J. Geophys. Res*, *98*, 15.797-15.808.

Kikuchi, M. & M. Ishida (1993), Souce retrieval for deep local earthquakes with broadband records, *Bull. Seism. Soc. Am.*, **83**, 1855-1870.

Kimura, G., E. Silver and P. Blum (1997), Proceedings of the Ocean Dril ling Program, *Init. Repts.*, vol. *170*, Texas A&M University, College Station TX, Ocean Drilling Program.

Kirby, S.H., Engdahl, E.R. & Denlinger, R. (1996), Intraslab earthquakes and arc volcanism: dual physical expressions of crustal and uppermost mantle metamorphism in subducting slabs, *In* G.E. Bebout et al. (Eds.), Subduction: top to bottom, *Geophysical Monograph*, 96, Washington D.C., American Geophysical Union, 195-214

Kissling, E. (1988), Geotomography with Local Earthquake Data, *Rev. of Geophys.*, *26*, 659-698.

Kissling, E. and J.C. Lahr (1991), Tomographic image of the Pacific Slab under southern Alaska, *Eclogae geol. Helv.*, *84/2*, 297-315

Kissling, E., Ellsworth, W. L., Eberhart-Phillips, D. and U. Kadolfer (1994), Initial reference models in local earthquake tomography, *J. Geophys. Res.*, *99*, 19,635-19,646.

Kissling, E., U. Kradolfer and H. Maurer (1995), *VELEST User Guide Short Introduction.* Institute of geophysics and Swiss seismological service, ETH, Zrich.

Kobayashi, K., M. Nakanishi, K. Tamaki and Y. Ogawa (1998), Outer slope faulting associated with western Kuril and Japan trenches, *Geophys. J. Int. 134*, 356-372.

Kradolfer, U. (1989), Seismische Tomographie in der Schweiz mittels lokaler Erdbeben, *PhD thesis*, ETH, Zürich

Lefeldt, M. and I. Grevemeyer (2008), Centroid depth and mechanism of trench-outer rise earthquakes off Central America, *Geophys. J. Int.*, *172*, 240-251, doi:10.1111/j.1365-246X.2007.03616.x

Lomax, A., J. Virieux, P. Volant and C. Berge (2000), Probabilistic earthquake location in 3D and layered models: Introduction of a Metropolis-Gibbs method and comparison with linear locations, in *Advances in Seismic Event Location* Thurber, C.H., and N. Rabinowitz (eds.), Kluwer, Amsterdam, 101-134.

Lomax, A., A. Zollo, P. Capuano, and J. Virieux (2001), Precise, absoute earthquake location under Somma-Vesuvius volcano using a new 3D velocity model, *Gephys. J. Int.*, *146*, 313-331.

Lonsdale, P. (1988), Structural pattern of the Galapagos microplate and evolution of the Galapagos triple junction, *J. Geophys. Res.*, 93, 13551-13574.

Macdonald, H. & Fyfe, W. S. (1985), Rate of serpentinization in seafloor environments. *Tectonophysics* 116, 123–135.

Madsen, J.A., Fornari, D.J., Edwards, M.H., Gallo, D.G. & Perfit, M.R. (1992), Kinematic framework of the Cocos-Pacific plate boundary from 13°N to the Orozco transform fault: Results from an extensive magnetic and SeaMARC II survey. *J. Geophys. Res.*, vol. 97, 7011–7024.

Maurer, H. and U. Kradolfer (1996), Hypocentral parameters and velocity estimations in the western Swiss alps by simultaneous inversion of P- and S-wave data, *Bull. Seism. Soc. Am.*, *86*, 32-42

Masson, D.G. (1991), Fault patterns at outer trench walls, *Mar. Geophys. Res. 13*, 209-225.

McGinnis, S. (2001), On the Effects of Geometry in Discrete Element Numerical Earthquake Simulations, *PhD-thesis*, University of Colorado

McKenzie, D., Jackson, J. & Priestley, K. (2005), Thermal structure of oceanic and continental lithosphere. *Earth and Planetary Science Letters*, v. 233, p. 337–349, doi: 10.1016/j.epsl.2005.02.005 (2005).

Meade, C. and R. Jeanloz (1991), Deep focused earthquakes and recycling of water into the Earth s mantle, *Science 252*, 68-72.

Müller G. (1985), The reflectivity method: A tutorial. *J. Geophys.*, *58*: 153-174.

Peacock, S.M. (2001), Are the lower planes of double seismic zones caused by serpentine dehydration in subducting oceanic mantle? *Geology*, *29*, 299-302.

Peacock, S.M. (2003), Insight into the hydrogeology and alteration of oceanic lithosphere based on subduction zones and arc volcanisms. *In* Davis EE, Elderfield H (Eds.), Hydrogeology of Oceanic Lithosphere, *Cambridge University Press 2004*.

Peacock, S.M., P.E. van Keken, S.D. Holloway, B.R. Hacker, G.A. Abers and R.L. Fergason (2005), Thermal structure of the Costa Rica - Nicaragua subduction zone, *Phys. Eart. plan. Sci. Int.,*, **149**, 187–200.

Protti, M., Gendel, F.; and McNally, K. (1994), The geometry of the WadatiBenioff Zone under southern Central America and its tectonic significance: results from a highresolution local seismographic network, *Phys. of the Earth and Planet. Inter.*, *84*, p. 271-287.

Raleigh, C.B., and M.S. Paterson (1965), Experimental deformation of serpentinite and its tectonic implications: *Journal of Geophysical Research*, *70*, 3965-3985.

Ranero, C.R., J. Phipps Morgan, K. McIntosh and C. Reichert (2003), Bending, faulting, and mantle serpentinization at the Middle America Trench, *Nature*, *425*, 367-373.

Ranero, C.R. & V. Sallars (2004), Geophysical evidence for hydration of the crust and mantle Nazca plate during bending at the north Chile trench. *Geology*, **vol. 32**, p.549

Ranero, C.R., A. Villaseñor, J. Phipps Morgan & W. Weinrebe (2005), Relationship between bendfaulting at trenches and intraslab seismicity, *Geosystems, Geophysics, Geochemistry* **6**, doi:10.1029/2005GC000997.

Rawlinson, N. and Urvoy, M. (2006), Simultaneous inversion of active and passive source datasets for 3-D seismic structure with application to Tasmania. *Geophys. Res. Lett.*, **33** L24313, doi:10.1029/2006GL028105.

Rawlinson, N., de Kool, M. and Sambridge, M. (2007), Seismic wavefront tracking in 3-D heterogeneous media: applications with multiple data classes. *Explor.*

Geophys., **37**, 322-330.

Roggensack, K., R.L. Hervig, S.B. McKnight and S.N. Williams (1997), Explosive basaltic volcanism from Cerro Negro volcano: influence of volatiles on eruptive style, *Science*, *277*, 1639-1642.

Rüpke, L., J. Phipps Morgan, M. Hort and J.D.A. Connolly (2002), Are the regional variations in Central America arc lavas due to differing basaltic peridotitic slab sources of fluids? *Geology*, *30*, 1035-1038.

Schweitzer, J. (2001), HYPOSAT - An enhanced routine to locate seismic events. *Pure and Applied Geophysics*, *158*, 277-289.

Seno, T. and D.G. Gonzalez (1987), Faulting caused by earthquakes beneath the outer slope of the Japan Trench, *Journal of the Physics of the Earth*, *35*, p. 381-407.

Seno, T. and Y. Yamanaka (1996), Double seismic zones, compressional deep trench-outer rise events and superplumes, *in* Subduction Top to Bottom, edited by G. E. Bebout, D. W. Scholl, S. H. Kirby, and J. P. Platt, Geophys. Monogr, AGU, Washington D. C., *96*, pp. 347-355.

Smith, W. H. F. & D. T. Sandwell (1997), Global seafloor topography from satellite altimetry and ship depth soundings, *Science*, v. **277**, p. 1957-1962, 26 Sept..

Spence, W. (1986), The 1977 Sumba earthquake series: evidence for slab pull force acting at a subduction zone, *J. Geophys. Res.*, *91*, 7225-7239.

Staudigel, H., T. Plank, B. White and H. U. Schmincke (1996), Geochemical fluxes during alteration of the basaltic oceanic crust: DSDP sites 417 and 418, *in Subduction: Top to Bottom, Geophys. Monogr. Ser.*, *vol. 96*, edited by G. E. Bebout et al., pp. 19-38, AGU, Washington, D. C.

Syracuse, E.M., G.A. Abers, L. Auger, G. Reyes, J. Brewer, K.M. Fischer, J.M. Protti, V. Gonzales, W. Strauch (2006), Seismic Velocities and Earthquake Locations in the Central America Upper Mantle: results from the TUCAN Experiment, EOS Trans. AGU, Fall Meet. Suppl., abst. T21G-04

Thölen, M. (2005), Systematische Kalibrierung von geophysikalischen Sensoren für Frequenzen unter 1 Hertz, *Diplomarbeit*, Universität Hamburg

Thurber, C. H. (1992), Hypocenter-velocity structure coupling in local earthquake tomography, *Phys. Earth Planet. Int.*, *75*, 55-62.

Tichelaar B.W., D.H. Christensen and L.J. Ruff (1992), Depth extent of rupture of the 1981 Chilean Outer-rise earthquake as inferred from long-period body waves, *Bull. Seism. Soc. Am.*, *82*, 1236-1252.

Tilmann, F.J., Grevemeyer, I., Flueh, E.R., Dahm, T. & Goßler, J. (2007) Seismicity in the outer rise offshore southern Chile: indication of fluid effects in crust and mantle.

Tonarini, S., S. Agostini, C. Doglioni, F. Innocenti, & P. Manetti (2007), Evidence for serpentinite fluid in convergent margin systems: The example of El Salvador (Central America) arc lavas, *Geochem. Geophys. Geosyst.*, 8, Q09014, doi:10.1029/2006GC001508.

Ungerer J. (1990), Berechnung von Nahfeldseismogrammen mit der Reflektivitätsmethode. Diplomarbeit, Institut für Geophysik, Universität Stuttgart, Germany.

Vera, E.E., Mutter, J.C., Buhl, P., Orcutt, J.A., Harding, A.J., Kappus, M.E., Detrick, R.S. & Brocher, T.M. (1990), The structure of 0 to 0.2 m.y. old oceanic crust at 9°N on the East Pacific Rise from expanded spread profiles. *J. Geophys. Res.*, vol. 95, 15529–15556.

Wallmann, K. (2001), The geological water cycle and the evolution of marine d180 values, *Geochim. Cosmochim. Acta* 65, Nr. 15, S. 2469-2485

Wang, R. (1999), A simple orthonormalization method for stable and efficient computations of Green's functions. *Bulletin of the Seismological Society of America*, *89(3)*, 73341.

Wilkens, R.H., Fryer, G.J. & Karsten, J. (1991), Evolution of porosity and seismic structure of upper oceanic crust: Importance of aspect ratios. *J. Geophys. Res.*, 96: 17981-17995

Wilson, D.S. (1996), Fastest known spreading on the Miocene Cocos-Pacific Plate boundary, *Geophys. Res. Lett.* **23**, 3003-3006

Wilson, D.S., D.A.H. Teagle & G.D. Acton *et al.* (2003), Proc. ODP, Init. Repts., 206 [WWW document] URL http://www-odp.tamu.edu/publications/206_IR/206ir.htm

Yamanaka, Y., and M. Kikuchi (2003), Source processes of the recurrent Tokachi-oki earthquake on September 26, 2003, inferred from teleseismic body waves, *Earth Planet. Sci.*, *55*, e21-e24.

Yoshida Y., K. Satake and K. Abe (1992), The large normal-faulting Mariana earthquake of April 5, 1990 in uncoupled subduction zone. *Geophys. Res. Lett.*, *19*, 297-300.

Danksagung

Ich möchte mich bei den vielen Kollegen und Freunden, die mich bei dieser Arbeit unterstützt haben, herzlich bedanken, insbesondere bei meinem Betreuer Ingo Grevemeyer, der mir bei allen Fragen stets weitergeholfen hat, mir dabei aber jegliche wissenschaftliche Freiheit in Bezug auf Methodik und Interpretation gelassen hat. Einen großen Dank auch an Ernst Flüh für viele Ratschläge und besonders für die Möglichkeit, an zahlreichen Expeditionen teilzunehmen.

Ebenfalls bedanken möchte ich mich bei Nick Rawlinson von der Australian National University, mit dem vielmehr zufällig ein Kontakt und eine Zusammenarbeit entstanden, ohne die aber die wichtige 3D-Tomographie in dieser Arbeit so nicht hätte durchgeführt werden können. Dank dabei auch an Ellen Syracuse und Geoffrey Abers, beide Boston University, für die großzügige Bereitstellung ihrer Daten.

Ein besonderer Dank gilt Cesar Ranero für seine vielseitige Unterstützung bei diesem Projekt und ebenfalls Jason Phipps Morgan für einige fruchtbare Ideen.

Weiteren Dank schulde ich dem gesamten SFB 574, besonders Wolfgang Rabbel, Martin Thorwart und Nilay Dinc-Akdogan.

Vielen Dank an Jürgen Gossler für seine große Hilfe bei der Aufbereitung der ORN-Daten und bei zahlreichen weiteren Fragen.

Nicht zuletzt möchte ich meiner Familie, insbesondere meinem Vater, für moralische und oft auch finanzielle Unterstützung danken!

Lebenslauf

Marten Lefeldt wurde am 25.09.1980 in Bornhöved geboren. 1999 erhielt er sein Abitur am Fachgymnasium - technischer Zweig - der beruflichen Schulen des Kreises Segeberg. Ende des Jahres begann er das Studium der Physik (Diplom) an der Christian-Albrechts-Universität zu Kiel, wo er 2001 sein Vordiplom und im November 2004 sein Diplom erhielt. Seit 2005 arbeitet er im Sonderforschungsbereich 574 am Leibniz Institut für Meereswissenschaften und der Christian-Albrechts-Universität zu Kiel als wissenschaftlicher Angestellter. Diese Doktorarbeit entstand aus dieser Tätigkeit.

Pivatanschrift:
Lindenstr. 31, 24619 Bornhöved

Staatsangehörigkeit:
deutsch

Appendix